Diplomarbeit

Simulation of Hot Cracking in Laser Powder Bed Fusion of Metals (PBF-LB/M)

ausgeführt zum Zwecke der Erlangung des akademischen Grades eines Diplom-Ingenieurs (Dipl.-Ing. oder DI) eingereicht an der TU Wien, Fakultät für Maschinenwesen und Betriebswissenschaften, von

Carlos Geovanny DURÁN OSCUEZ

Mat. Nr.: 11816279

unter der Leitung von

Univ.Prof. Dipl.-Phys. Dr.-Ing. Andreas Otto

Institut für Fertigungstechnik und Photonische Technologien, E311

und

Univ.Ass. Dipl.-Ing. BSc Constantin Zenz

Institut für Fertigungstechnik und Photonische Technologien, E311

Wien, Oktober 2023

Ich nehme zur Kenntnis, dass ich zur Drucklegung dieser Arbeit nur mit Bewilligung der Prüfungskommission berechtigt bin.

Eidesstattliche Erklärung

Ich erkläre an Eides statt, dass die vorliegende Arbeit nach den anerkannten Grundsätzen für wissenschaftliche Abhandlungen von mir selbstständig erstellt wurde. Alle verwendeten Hilfsmittel, insbesondere die zugrunde gelegte Literatur, sind in dieser Arbeit genannt und aufgelistet. Die aus den Quellen wörtlich entnommenen Stellen, sind als solche kenntlich gemacht.

Das Thema dieser Arbeit wurde von mir bisher weder im In- noch Ausland einem_r Beurteiler_in zur Begutachtung in irgendeiner Form als Prüfungsarbeit vorgelegt. Diese Arbeit stimmt mit der von den Begutachter_innen beurteilten Arbeit überein.

Ich nehme zur Kenntnis, dass die vorgelegte Arbeit mit geeigneten und dem derzeitigen Stand der Technik entsprechenden Mitteln (Plagiat-Erkennungssoftware) elektronisch-technisch überprüft wird. Dies stellt einerseits sicher, dass bei der Erstellung der vorgelegten Arbeit die hohen Qualitätsvorgaben im Rahmen der geltenden Regeln zur Sicherung guter wissenschaftlicher Praxis „Code of Conduct“ an der TU Wien eingehalten wurden. Zum anderen werden durch einen Abgleich mit anderen studentischen Abschlussarbeiten Verletzungen meines persönlichen Urheberrechts vermieden

Wien, 13.10.2023

Ort und Datum

[redacted]

Unterschrift

Acknowledgements

I wish to thank Prof. Andreas Otto for providing me with the opportunity to develop my master thesis at the Institute of Production Engineering and Photonic Technologies (IFT).

My sincere gratitude goes out to Dipl.-Ing. Constantin Zenz and Dr. Robert Bielak for their invaluable guidance, commitment, and professionalism throughout this work.

I would also like to acknowledge the unconditional support I have received from my parents and relatives.

Lastly, thank you Katherine and Helena for giving me daily motivation.

Table of Contents

Abstract

Hot cracking is a common defect that affects the processability of many industrially relevant alloys in the field of laser and laser-assisted manufacturing. Specific engineering applications may benefit significantly from these alloys if the aforementioned defect is effectively mitigated. The problem of solidification cracking, a form of hot cracking, was examined through computational simulations of the Laser Powder Bed Fusion (PBF-LB) process, in which individual beads of CM247LC nickel superalloy were reproduced. This study hypothesized that it is feasible to model the thermomechanical behavior of the mushy zone using the Finite Volume Method (FVM) as discretization technique, allowing its integration into a multiphysical simulation model for the evaluation of hot cracking.

A suitable hot cracking criterion was implemented in a multiphysical model for laser material processing, and the effect of preheating on crack mitigation was evaluated using a Hot Cracking Susceptibility (HCS) index. The selected criterion is based on the competition between two physical parameters: the rate at which liquid metal is fed into a control volume within the mushy zone (*Rate of Feeding*, ROF) and the rate at which this control volume contracts (*Rate of Shrinkage*, ROS). Hot cracking is possible when the ROF is less than the ROS. The first parameter is determined by thermo-fluid analysis, while the second is derived from the thermomechanics of the mushy zone, assuming linear-thermoelasticity as the constitutive law governing deformations and stresses. It was found that higher preheating temperatures do not improve liquid feeding into the mush, but significantly reduce the rate of shrinkage, favoring the mitigation of hot cracking. The available simulation tool provides a good basis for predicting the impact of different physical variables and process parameters on solidification cracking during laser manufacturing.

Kurzfassung

Heißrissbildung ist ein häufiger Fehler, der die Verarbeitbarkeit vieler industriell relevanter Legierungen im Bereich der Laser- und lasergestützten Fertigung beeinträchtigt. Bestimmte technische Anwendungen können erheblich von diesen Legierungen profitieren, wenn der oben genannte Mangel wirksam gemindert wird. Das Problem der Erstarrungsrissbildung, eine Form der Heißrissbildung, wurde durch Computersimulationen des Laserstrahlschmelzens (PBF-LB/M) untersucht, bei denen einzelne Nähte der Nickelbasis-Superlegierung CM247LC reproduziert wurden. In dieser Studie wurde die Hypothese aufgestellt, dass es möglich ist, das thermomechanische Verhalten der Mushy Zone mithilfe der Finite-Volumen-Methode (FVM) als Diskretisierungsverfahren zu modellieren, um die Integration in ein multiphysikalisches Simulationsmodell zur Bewertung der Heißrissbildung zu ermöglichen.

Ein geeignetes Heißrisskriterium wurde in einem multiphysikalischen Modell für die Lasermaterialbearbeitung implementiert, und die Auswirkung des Vorwärmens auf die Rissminderung wurde mithilfe einer Heißrissanfälligkeitsindex (HCS) bewertet. Das ausgewählte Kriterium basiert auf dem Wettbewerb zwischen zwei physikalischen Parametern: der Rate, mit der flüssiges Metall in ein Kontrollvolumen innerhalb der Mushy Zone eingespeist wird (*Rate of Feeding*, ROF) und der Rate, mit der sich dieses Kontrollvolumen zusammenzieht (*Rate of Shrinkage*, ROS). Heißrissbildung ist möglich, wenn der ROF kleiner als der ROS ist. Der erste Parameter wird durch Thermofluidanalyse bestimmt, während der zweite aus der Thermomechanik der Mushy Zone abgeleitet wird, wobei lineare Thermoelastizität als Materialgesetz für Verformungen und Spannungen angenommen wird. Es wurde festgestellt, dass höhere Vorwärmtemperaturen die Flüssigkeitszufuhr in der Mushy Zone nicht verbessern, aber die Schrumpfungsrate erheblich verringern, wodurch die Heißrissneigung reduziert wird. Das verfügbare Simulationstool bietet eine gute Grundlage, um den Einfluss verschiedener physikalischer Variablen und Prozessparameter auf die Erstarrungsrissbildung bei der Laserfertigung vorherzusagen.

List of Figures

List of Tables

List of Abbreviations and Symbols

AM ..... Additive Manufacturing
BTR ..... Brittle Temperature Range
Bal. ..... Balance
CA ..... Cellular Automata
CTE ..... Coefficient of Thermal Expansion
DSC ..... Differential Scanning Calorimetry
e.g. ..... example given
Eq. ..... Equation
Eqs. ..... Equations
Fig. ..... Figure
Figs. ..... Figures
FDM ..... Finite Difference Method
FVM ..... Finite Volume Method
GBLF ..... Grain Boundary Liquid Films
HAZ ..... Heat-Affected Zone
HCS ..... Hot Cracking Susceptibility
HIP ..... Hot Isostatic Pressing
i.e. ..... id est (that is)
OpenFOAM ..... Open Source Field Operation and Manipulation
PBF-LB/M ..... Laser Powder Bed Fusion of Metals
PBF-LB ..... Laser Powder Bed Fusion
Qi ..... Quartile i
RDG ..... Rappaz-Drezet-Gremaud
ROF ..... Rate of Feeding
ROS ..... Rate of Shrinkage
SLM ..... Selective Laser Melting
TIG ..... Tungsten Inert Gas
VOF ..... Volume of Fluid Method
w/ ..... with
w/o ..... without

a ..... composition coefficient of liquid density
a_c ..... crack length
a_i ..... constants for estimation of k_v
α ..... linear coefficient of thermal expansion
b ..... thickness of the intergranular liquid film
β ..... solidification shrinkage factor
c_p ..... specific heat capacity
c ..... dendrite network tortuosity
C_L ..... composition of the liquid at the solid-liquid interface
C_O ..... alloy composition
CII ..... crack initiation index
D ..... ductility curve

$\boldsymbol{D}$ ..... displacement vector field
D_p ..... average diameter of the powder particles
∂V ..... closed boundary of V
$d\Omega$ ..... surface differential
Δp_{crit} ..... critical pressure drop
ΔT_{br} ..... width of the BTR
δ ..... constant to avoid division by zero
e ..... total accumulated strain
e_V ..... unit volume change
E ..... modulus of elasticity
E_a ..... activation energy
ε ..... strain
ε_p ..... ductility curve (elongation to failure)
ε_{sh} ..... strain curve (linear shrinkage/contraction strain)
$\dot{\varepsilon}_{p,max}$ ..... maximum strain rate
$\boldsymbol{\varepsilon}$ ..... infinitesimal strain tensor
$\dot{\boldsymbol{\varepsilon}}$ ..... strain rate tensor
$\boldsymbol{\varepsilon}^{mech}$ ..... mechanical strain
$\boldsymbol{\varepsilon}^{th}$ ..... thermal strain
η ..... kinematic viscosity
f_l ..... volumetric fraction of liquid
f_s ..... volumetric fraction of solid
F_z ..... separation force
g ..... acceleration of gravity
G ..... shear modulus (second Lamé constant)
G_T ..... temperature gradient
γ_{LG} ..... liquid-surrounding gas interface energy
γ_{SL} ..... solid-liquid interface energy
γ_{GB} ..... grain boundary energy
γ_{fr} ..... effective fracture surface energy
h ..... distance from a volume element to the melt surface
$\boldsymbol{I}$ ..... unit tensor
k ..... thermal conductivity
k_p ..... thermal conductivity of metallic powder
k_f ..... thermal conductivity of surrounding phase
k_v ..... thermal conductivity of metallic vapor
k_s ..... conductivity of the solid
k_r ..... heat transfer due to radiation
k_e ..... equilibrium partition coefficient
κ ..... permeability of the mushy zone
K ..... bulk modulus
ℓ ..... substrate length
L ..... length of the porous network
λ ..... first Lamé constant
λ_2 ..... secondary dendrite arm spacing
m ..... microstructure parameter
m_L ..... slope of the liquidus line
μ ..... dynamic viscosity
n ..... total number of elements i

$\boldsymbol{n}$ ..... unit vector pointing out of a control volume
N ..... sample size (total number of elements j)
ν ..... Poisson's ratio
p ..... liquid pressure
p_o ..... atmospheric pressure
p_m ..... metallostatic pressure
p_{cap} ..... capillary pressure
p_s ..... effective feeding pressure
p_c ..... cavitation pressure
p_f ..... external pore pressure
p_r ..... reserve of plasticity
ϕ ..... porosity of the powder bed
R ..... ideal gas constant
R_0 ..... radius
ρ ..... density
ρ_o ..... density of pure element at the melting point
ρ_l ..... density of the liquid phase
ρ_s ..... density of the solid phase
$\bar{\rho}$ ..... density average
ρ_{298} ..... density at 298 K
s ..... track length
S ..... area between ε_p and ε_{sh}
$\boldsymbol{S}$ ..... source term (fluid flow through a porous medium)
$\boldsymbol{\sigma}$ ..... Cauchy stress tensor
σ_{fr} ..... fracture stress
σ ..... Boltzmann constant
T ..... temperature
T_L ..... liquidus temperature
T_S ..... temperature at the end of solidification
T_{coh} ..... coherency temperature
T_{cr} ..... temperature at which a hot cracking criterion is met
T_{ref} ..... reference temperature
$\dot{T}$ ..... cooling rate
t ..... time
t_V ..... vulnerable time period
t_R ..... time period during which stress relief is possible
t_{coh} ..... time to reach the coherency point
t_{cr} ..... time at which a hot cracking criterion is met
$\boldsymbol{u}$ ..... velocity field
$\boldsymbol{v}$ ..... rate of change of displacement
v_T ..... velocity of the liquidus isotherm
V ..... volume
V_i ..... volume of element i
V_j ..... volume of element j
$\boldsymbol{x}$ ..... position vector
Y_i ..... mass percentage of element i
Y_{heavy} ..... total mass percentage of heavy elements

1 Introduction

Laser Powder Bed Fusion of Metals (PBF-LB/M) is a technology that employs the thermal energy of a laser beam to selectively fuse regions of a previously deposited layer of metal powder onto a base plate or substrate. The process begins with the fusion of a single track, which together with other individual tracks form a layer, and the consecutive addition of layers builds a three-dimensional component [1]. This Additive Manufacturing (AM) technique is rapidly gaining ground among various industrial applications due to the benefits it provides, especially the ability to produce parts with sophisticated geometries that would not be achievable with traditional subtractive manufacturing, casting or forming methods.

Certainly, various defects can also occur when producing components using PBF-LB/M, e.g., porosity (due to lack of fusion, keyholes, pores inside powder particles, gas entrapment, spattering, denudation effect), balling, poor dimensional accuracy, residual stress, undesired surface roughness, cracks, etc. Mitigation strategies include the use of tuned process parameters, preheating, control over the shape and size of the melt pool, post-processing techniques, among others. These strategies are often designed on the basis of experimental investigation, analytical and numerical modeling, or statistical methods [2].

There is currently a growing interest in studying metallic alloys for high-performance applications, whose potential can be fully exploited if a better understanding of their PBF-LB processability and greater control over the properties and quality of the finished parts are achieved. Among these materials, nickel-based superalloys occupy an important place as they are used in many demanding fields, such as aerospace, chemical and petrochemical industries, nuclear power systems, steam turbine power plants, heat treatment equipment, automotive industry, etc. [3]. What generally makes them suitable for operating in such critical environments is their excellent mechanical properties at elevated temperatures and their high resistance to oxidation and corrosion. Yet, depending on the composition, many Ni-based alloys are considered non-weldable and highly prone to hot cracking.

Hot cracking is a broadly used terminology to describe cracks that occur during welding of metallic materials, and given the similarity of the physical processes involved, it has also been adopted in the field of AM. In metal casting, this phenomenon is often referred to as hot tearing or hot shortness. The EN ISO 17641-1 standard [4] classifies hot cracks into solidification cracks, liquation cracks, and ductility dip cracks. Solidification cracks, also known as segregation cracks, form in a newly fused metal bead during the phase change from liquid to solid, while liquation cracks originate as a result of localized melting within a portion of the heat-affected zone (HAZ) that is very close to the fusion boundary. The HAZ refers to a region of the material near the fusion zone in which the microstructure has been altered by the heating

process. Ductility dip cracks, on the other hand, are found in solid regions inside or outside the HAZ, affected by a sharp loss of ductility due to high temperatures.

Both solidification and liquation cracks suggest the presence of a liquid phase when a crack initiates, whereas ductility dip cracking occurs in the solid state. Although not usually categorized as hot cracking, strain-age cracking is another type of defect commonly found in additive manufacturing of Ni-based superalloys. This defect is associated with the precipitation of the gamma prime strengthening phase, promoted by the intrinsic heat treatment of the workpiece during subsequent layer deposition, or during post-process treatment [5, 6].

In the course of this investigation, solidification cracking in PBF-LB is analyzed through computational simulations that reproduce single-track processing of superalloy CM247LC. Stereomicrographic images showing solidification cracks in laser-sintered single tracks of CM247LC are included in Fig. 1.1. Due to its outstanding performance at high temperatures, this Ni-based alloy is primarily used in components such as gas turbine blades for which, compared to other manufacturing processes, PBF-LB offers significant advantages when adding cooling features like orifices and internal channels for air circulation [7, 8]. A major drawback in the AM and welding processability of the aforementioned material is solidification cracking, which has motivated several investigations seeking to understand and mitigate this problem. Hereinafter, the terms solidification cracking and hot cracking will be used interchangeably.

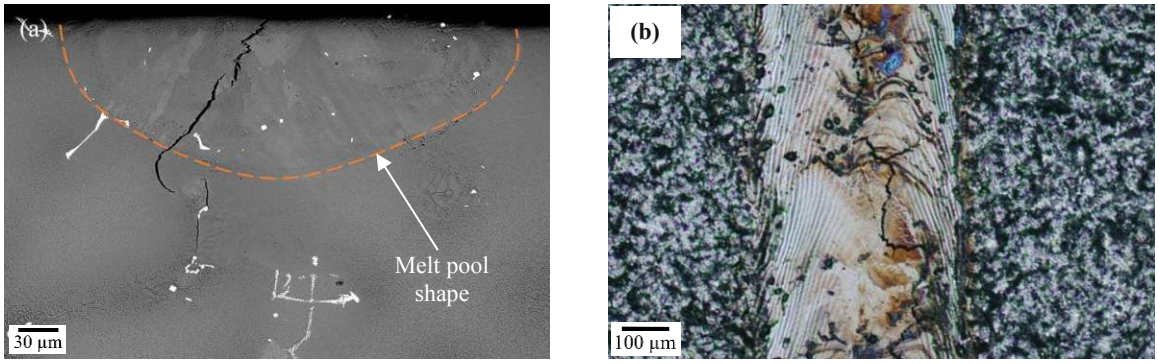

Fig. 1.1: (a) Cross-section view and (b) upper view of solidification cracks in single tracks of CM247LC. *Courtesy of Maurizio Vedani, Politecnico di Milano.*

In chapter 2 of the present work, an overview of cracking theories and criteria is presented. Many of these criteria address the problem from the point of view of solid mechanics, describing the evolution of strain and/or stress during processing and establishing critical values for solidification cracking. Other criteria focus on the dynamics of liquid feeding towards the solidifying portion of the material. In this study, both solid mechanics and fluid mechanics are

taken into account in the evaluation of hot cracking. Chapter 3 describes in detail the proposed criterion and how it is implemented.

A multi-physical numerical model developed within the OpenFOAM® (Open Field Operation and Manipulation) framework [9 - 12] is used to simulate the single track PBF-LB process and to evaluate the proposed hot cracking criterion. The numerical simulation model, as well as the properties of the investigated material, are described in chapter 4. Simulation results are presented and discussed in chapters 5 and 6, respectively. Lastly, chapter 7 provides the main conclusions and perspectives for future research.

The importance of this study lies in applying the available numerical simulation tools to assess solidification cracking not only from a solid mechanics approach, but also in combination with thermofluid science. In this way, different physical variables and process parameters (mechanical and non-mechanical) can be investigated to evaluate their influence on solidification crack mitigation when using laser-assisted manufacturing technologies such as PBF-LB/M.

2 Hot Cracking Theories and Criteria

Over the last century, various efforts have been made to derive a mathematical model that accurately describes hot cracking in manufacturing processes such as metal casting and welding. However, there is no complete agreement on the exact mechanisms or interactions driving this phenomenon, nor is there a general method to predict whether or not this defect will occur under a given set of conditions.

The hot cracking problem is complex because it depends on numerous factors, which vary in nature and origin. Cross [13], for example, categorizes the controlling factors affecting crack susceptibility as metallurgical and mechanical. The first category includes, but is not limited to, Brittle Temperature Range (BTR), interdendritic melt flow, dendrite coherency, eutectic fraction, surface tension, grain morphology, and porosity. The second category involves stress, strain, and strain rate. Crack initiation encompasses an interplay between these metallurgical and mechanical factors, which in turn are affected by process parameters, chemical composition of the materials involved, boundary and initial conditions (fixturing, pre-heating, etc.).

This chapter provides an overview of some of the hot cracking theories and criteria available in the literature. Table 2.1 organizes the authors and the corresponding publication years of the different criteria into five groups: BTR- and strain-, stress-, feeding-, strain rate-, and pore-based criteria. A brief description of each group's general aspects is provided.

Table 2.1: Overview of hot cracking theories and criteria

Author(s) and publication year [a]	Ref.	Author(s) and publication year [a]	Ref.
BTR- and Strain-based		Stress-based	
Pumphrey and Jennings (*shrinkage-brittleness theory*), **1948**	[14]	Norton (*fracture strength*), **1914**	[16]
Pellini (*strain theory*), **1954**	[14]	Saveiko, **1961**	[16]
Borland (*generalized theory*), **1960**	[14]	Williams and Singer, **1968**	[17]
Matsuda (*modified generalized theory*), **1982**	[14]	Dickhaus et al., **1994**	[16]
Novikov (*reserve of plasticity*), **1995**	[15]	Lahaie and Bouchard, **2001**	[19]
Magnin et al. (*principal plastic strain*), **1996**	[15]	Liquid feeding	
Strain rate-based		Feurer (*feeding-shrinkage*), **1977**	[20]
Prokhorov (*technological strength*), **1971**	[22]	Clyne and Davies, **1981**	[20]
Rappaz et al. (*RDG criterion*), **1999**	[23]	Katgerman, **1982**	[20]
Braccini et al., **2000**	[24]	Hatami et al., **2008**	[16]
Kou, **2015**	[25]	Pore-based	
		Draxler, **2019**	[26]

[a] If available, the denomination of the theory or criterion is given in parentheses.

2.1 BTR- and Strain-Based Theories and Criteria

As shown in Fig. 2.1(a), the shrinkage-brittleness theory of Pumphrey and Jennings proposes that solidification cracking, regarded as a solid-solid separation, takes place within an "effective interval" bounded by the coherency temperature and the temperature at which solidification is completed [14]. When the coherency temperature is reached below liquidus, the crystals begin to form bridges and the material becomes capable of withstanding mechanical strain. Cracking is only feasible below this temperature.

Unlike the above, Pellini's strain theory views cracking as a solid-liquid separation and considers that coherency or solid-solid bridging does not occur until the final stages of solidification [14]. As represented in Fig. 2.1(b), there are two stages of solidification, a mushy stage and a liquid film stage. The latter is further divided into a normal film stage that occurs

under equilibrium conditions (*normal solidus*[1] as lower bound) and a segregate film stage driven by non-equilibrium solidification (*segregate solidus*[2] as lower limit). Cracking is not possible in the mushy range due to the uniform strain distribution of the solid-liquid mixture. Strain starts building up at the beginning of the film stage, leading to cracks once the solid-liquid boundary ductility is exceeded.

Fig. 2.1(c) and 2.1(d) represent Borland's generalized theory and Matsuda's modified generalized theory, respectively, which incorporate concepts from both the shrinkage-brittleness theory and the strain theory. They divide the solidification process into additional stages. Differently from Pellini's theory, Borland and Matsuda acknowledge the presence of coherency (solid-solid interaction) at a relatively early stage in the solidification process and both agree that the critical stage for crack initiation is below the coherency temperature.

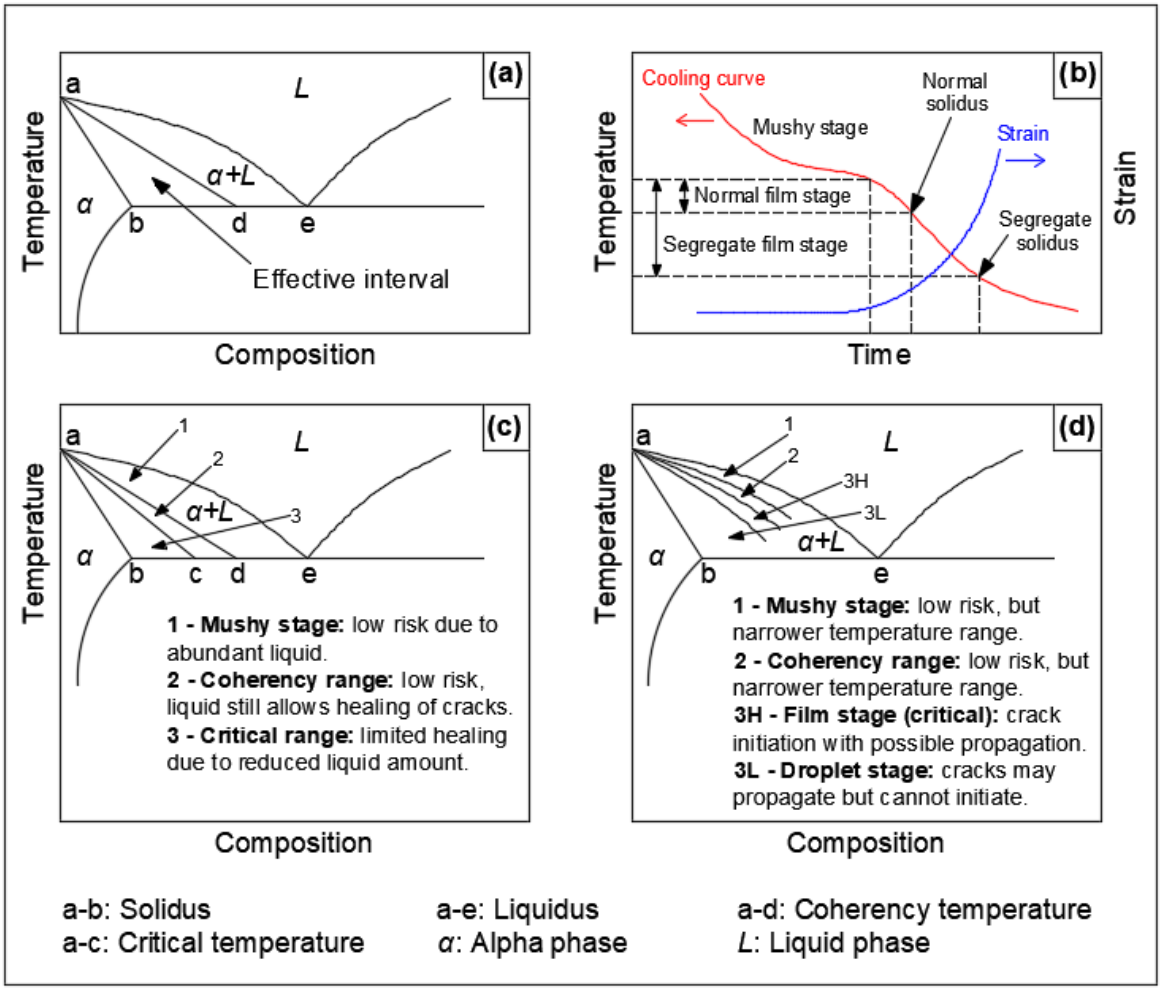

Fig. 2.1: Solidification cracking theories according to (a) Pumphrey and Jennings, (b) Pellini, (c) Borland, and (d) Matsuda. Adapted from [14].

[1] Also found in the literature as *bulk solidus* or *equilibrium solidus*.
[2] Also known as *true solidus* or *non-equilibrium solidus*.

The theories presented seek to establish a temperature interval in the solidification process where the material is prone to cracking. They also aim to describe a rupture mechanism. According to [14], it is very unusual to observe any indication of solid-solid fracture on the surface of a solidification crack, but there is enough evidence (metallographic and fractographic images) that supports Pellini's idea of solid-liquid separation, i.e., the presence of liquid films at the time of crack initiation.

The upper limit of the critical temperature range for solidification crack initiation is below liquidus. However, it could be given by the coherency temperature as proposed by the shrinkage-brittleness theory, or by a lower temperature as suggested by Borland and Matsuda. Regardless of the above, some researchers even consider the liquidus line as the upper limit for practical purposes. The lower limit of the critical range is also unclear. It could be the equilibrium solidus, the segregate solidus as suggested by Pellini, or a higher temperature (above the equilibrium solidus) as per Matsuda's observations.

The latter might explain why there are different interpretations in the literature about what the Brittleness Temperature Range (BTR) and its temperature limits actually represent. The BTR refers to a temperature span in which the alloy is susceptible to solidification cracking; analogous to the effective interval described by the shrinkage-brittleness theory. It can be estimated experimentally, using for example tensile, Varestraint or Trans-Varestraint tests, by obtaining ductility curves as shown in Fig. 2.2. The ductility curve, which is a temperature-dependent critical strain curve, provides the strain required to generate cracks at a given temperature. This strain is often referred to as an "augmented strain", because it characterizes the sum of the strain produced by external mechanical loading and the local strain induced by thermal action.

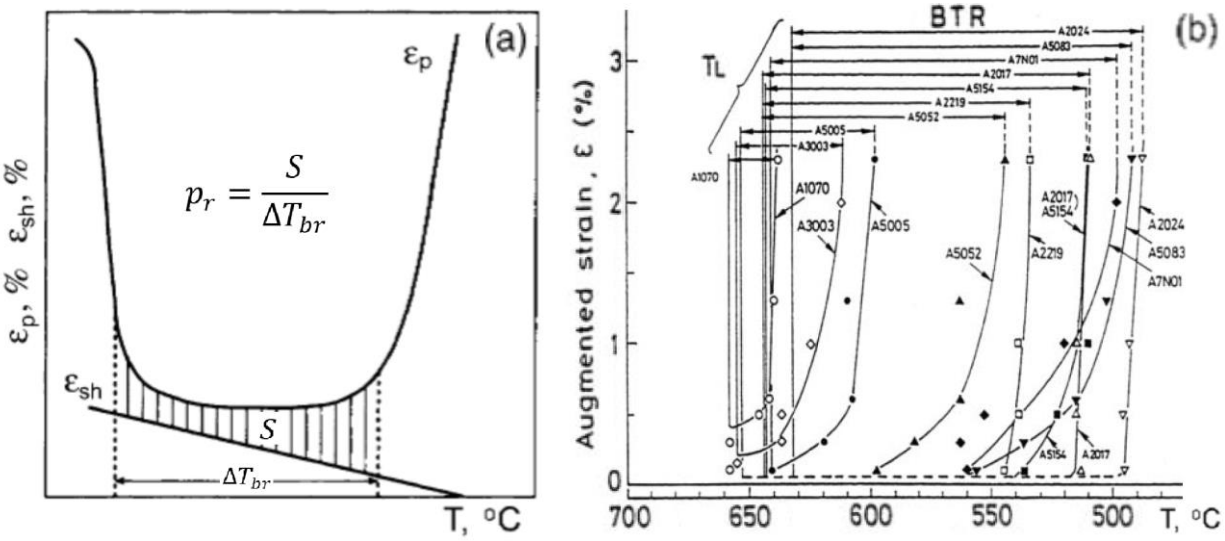

Fig. 2.2: Typical ductility curves of aluminum alloys obtained from (a) tensile tests [15], and (b) Trans-Varestraint tests [16].

Some hot cracking criteria depend on the width of the BTR, ΔT_{br}. For example, Novikov proposed a criterion based on the "reserve of plasticity", p_r, as described by Eq. (2.1), where S is the area between the ductility curve (elongation to failure), ε_p, and the strain curve (linear shrinkage/contraction strain), ε_{sh}, in the brittle temperature range [15]. The hot cracking susceptibility, HCS, is given by $1/p_r$; see Fig. 2.2(a). According to this criterion, the material cracks when its reserve of plasticity is exceeded by the accumulated strain, i.e., when $\varepsilon_{sh} > p_r$.

$$p_r = \frac{S}{\Delta T_{br}} \tag{2.1}$$

Another approach formulated by Magnin et al. states that hot cracking occurs when the maximum principal plastic strain exceeds an experimentally determined fracture strain within the BTR [15].

A controversial aspect of the BTR is that it is influenced by the process conditions, i.e., the same alloy can show different ductility curves. For instance, the BTR obtained from a casting test may differ from that of a weld test. Coniglio et al. [16] pointed out that large variations can be observed for a same material welded under different conditions. Eskin [15] showed how the ductility curves of aluminum alloys are influenced by cooling rate and strain rate. Wang et al. [17] measured the BTR for 310S stainless steel during laser welding using Trans-Varestraint tests. They reported a BTR of 11 K and 79 K for welding speeds of 0.2 m/min and 1 m/min, respectively. Using Varestraint testing, Kim et al. [7] found significant variations in the ductility curves of nickel superalloy CM247LC when producing oscillated welds with different frequencies. Chapter 4 shows that the solidification range[3] and thus the BTR is highly influenced by cooling rate, which determines whether solidification takes place under equilibrium or non-equilibrium conditions. Non-equilibrium solidification produces a shift of the solidus towards lower temperatures, i.e., the widening of the BTR.

2.2 Stress-Based Criteria

In addition to strain, mechanical stress has also been considered an important factor in the appearance of solidification cracks. Stress-based criteria assume that cracks occur when the local tensile stress exceeds the material strength (fracture stress). According to [16], Norton's work was one of the first to describe the relationship between the cracking susceptibility and fracture strength in a semisolid, suggesting that a fast increase of strength during solidification, i.e., rapid dendrite bonding, reduces the risk of hot cracking.

[3] Difference between the liquidus and solidus temperatures when the material solidifies.

By considering hot cracking as a solid-liquid separation, various approaches have been developed to evaluate the stress or force required to separate two grains surrounded by liquid. Examples include Eqs. (2.2) and (2.3) proposed by Saveiko and Dickhaus et al., respectively [16].

$$\sigma_{fr} = \frac{2\gamma_{LG}}{b} \tag{2.2}$$

$$F_z = \frac{3\pi\mu {R_0}^4}{8t}\left(\frac{1}{{b_1}^2} - \frac{1}{{b_2}^2}\right) \tag{2.3}$$

In Eq. (2.2), σ_{fr} is the fracture stress, γ_{LG} is the surface energy corresponding to the liquid-air (or surrounding gas) interface, and b is the thickness of the intergranular liquid film. This equation intends to estimate the stress required to pull apart two parallel plates separated by a thin liquid film, assuming perfect wetting between plates and liquid, no influence of sliding, uniform distribution of the liquid, and negligible viscosity. It also assumes that the liquid and the atmosphere are in contact.

Meanwhile, instead of considering surface energy as the most influential property, Eq. (2.3) relates the separation force, F_z, to the liquid's dynamic viscosity, μ. Grains are represented as two parallel plates of radius R_0 separated by a liquid film, whose thickness increases from b_1 to b_2 over the time period t. Coniglio et al. [16] made a noteworthy observation regarding Eqs. (2.2) and (2.3), which are plotted in Fig. 2.3 for the binary Al-Cu alloy. The required stress to separate the grains increases exponentially as the liquid film becomes thinner, which would make separation more difficult at the later stages of solidification. However, theories such as Pellini's suggest that hot cracking risk is the highest when thin liquid films are present.

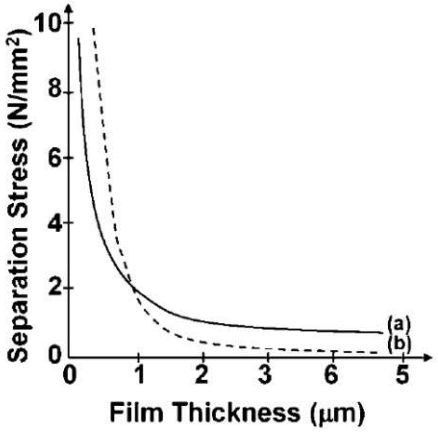

Fig. 2.3: Calculated fracture stress using (a) Eq. (2.2) and (b) Eq. (2.3) for liquid Al-Cu alloy at 660°C [16].

In a different way, Williams and Singer proposed a hot cracking model based on fracture mechanics [18]. The fracture stress, σ_{fr}, is determined from Eq. (2.4), where G is the shear modulus, ν is the Poisson's ratio, a_c is the crack length, and γ_{fr} is the effective fracture surface energy. The latter is estimated from Eq. (2.5), where γ_{SL} is the solid-liquid interface energy, and γ_{GB} is the grain boundary energy. According to [18], this model fails to describe the effect of grain size on hot cracking as it predicts a lower cracking susceptibility for coarser microstructures. In practice, cracking is generally less likely to occur with finer microstructures.

$$\sigma_{fr} = \sqrt{\frac{8\,G\,\gamma_{fr}}{\pi\,(1-\nu)\,a_c}} \tag{2.4}$$

$$\gamma_{fr} = 2\,\gamma_{SL} - \gamma_{GB} \tag{2.5}$$

On the basis of their research on direct chill casting of aluminum alloys, Lahaie and Bouchard [19] proposed Eq. (2.6) to determine the fracture stress required for hot cracking. This approach incorporates the solid fraction, f_s, the tensile strain, ε, and a microstructure parameter, m, which takes the values 1/3 for equiaxed structures and 1/2 for columnar grains. This model predicts a decreasing fracture stress with grain coarsening, which is in agreement with experimental observation. However, it does not show any correlation between fracture strain and grain size.

$$\sigma_{fr} = \frac{4\gamma_{LG}}{3b}\left[1 + \left(\frac{{f_s}^m}{1-{f_s}^m}\right)\varepsilon\right]^{-1} \tag{2.6}$$

2.3 Criteria based on Liquid Feeding

This group of criteria has its roots in Feurer's feeding-shrinkage concept, which suggests that hot tearing occurs due to lack of liquid feeding caused by resistance to fluid flow through the dendrite network [20]. The latter is treated as a permeable medium that becomes less permeable with decreasing temperature as a result of solidification shrinkage. The rate of feeding, ROF, and the rate of shrinkage, ROS, are the two parameters that build Feurer's criterion, which states that cracking is possible if $ROF < ROS$. This is illustrated in Fig. 2.4 for an Al-Si alloy.

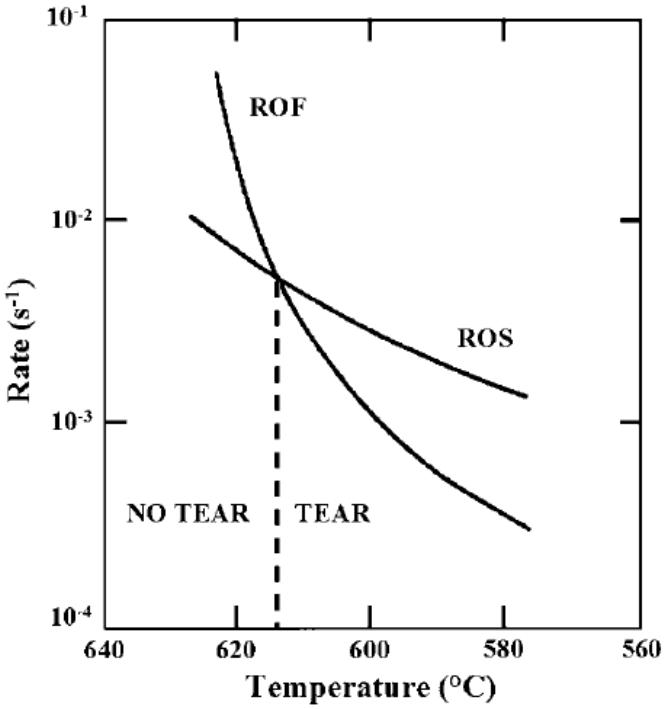

Fig. 2.4: Calculated ROF and ROS for an Al-Si alloy casting [16].

The ROF, as written in Eq. (2.7), represents the maximum volumetric flow rate of liquid per unit volume:

$$ROF = \left(\frac{\partial \ln V}{\partial t}\right)_{feeding} = \frac{{f_l}^2 {\lambda_2}^2 p_s}{24\pi c^3 \mu L^2} \tag{2.7}$$

where V is volume, t is time, f_l the volumetric fraction of liquid, λ_2 the secondary dendrite arm spacing, p_s the effective feeding pressure, c the dendrite network tortuosity, μ the liquid dynamic viscosity, and L the length of the porous network. Eq. (2.7) was derived using Darcy's law [21], which describes the fluid flow through a porous medium.

The effective feeding pressure, p_s, can be estimated from Eqs. (2.8) to (2.11), where p_o, p_m, and p_{cap} are the atmospheric, metallostatic, and capillary pressures, respectively, $\bar{\rho}$ is the density average of the solidifying volume element, ρ_l and ρ_s are the densities of the liquid and solid phases, respectively, f_l and f_s are the volumetric fractions of liquid and solid, respectively, g is the acceleration of gravity, h the distance from the volume element to the melt surface, γ_{SL} the solid-liquid interface energy, and λ_2 the secondary dendrite arm spacing.

$$p_s = p_o + p_m - p_{cap} \tag{2.8}$$

$$p_m = \bar{\rho} g h \tag{2.9}$$

$$\bar{\rho} = \rho_l f_l + \rho_s f_s \tag{2.10}$$

$$p_{cap} = \frac{4\,\gamma_{SL}}{\lambda_2} \tag{2.11}$$

The rate of shrinkage per unit volume, ROS, is given by Eq. (2.12):

$$ROS = \left(\frac{\partial \ln V}{\partial t}\right)_{shrinkage} = -\frac{1}{\bar{\rho}}\frac{\partial \bar{\rho}}{\partial t} \tag{2.12}$$

A more elaborated expression to estimate the rate of shrinkage can be found in [15] for aluminum alloys:

$$ROS = \frac{(\rho_o - \rho_s + a k_e C_L)\dot{T} f_l^{(2-k_e)}}{\bar{\rho}(1-k_e) m_L C_O} \tag{2.13}$$

where ρ_o is the density of pure aluminum at the melting point, ρ_s and ρ_l are the alloy densities at the solidus and liquidus temperatures, respectively, $\bar{\rho}$ is the average density, a is the composition coefficient of liquid density, k_e is the equilibrium partition coefficient, C_L is the composition of the liquid at the solid-liquid interface, C_O is the alloy composition, m_L is the slope of the liquidus line, and $\dot{T}$ is the average cooling rate. One downside of Eq. (2.12) or Eq. (2.13) is that they do not account for shrinkage due to mechanical straining.

Taking into account Feurer's theory, some indices of susceptibility to hot cracking (HCS) have been developed based primarily on the amount of time the alloy remains in the vulnerable region during solidification. An example is the cracking susceptibility coefficient of Clyne and Davies presented in Eq. (2.14):

$$HCS = \frac{t_V}{t_R} = \frac{t_{0.99} - t_{0.9}}{t_{0.9} - t_{0.4}} \tag{2.14}$$

where t_V is the vulnerable time period, i.e., when the fluid has difficulty moving freely through the dendrite network, t_R represents the time period during which stress relief is possible, $t_{0.4}$,

$t_{0.9}$ and $t_{0.99}$ are the times at which the solid fraction reaches 0.4, 0.9, and 0.99, respectively [20].

Similar models developed by Katgerman and Hatami et al. are described by Eqs. (2.15) and (2.16), respectively [16, 20]:

$$HCS = \frac{t_{0.99} - t_{cr}}{t_{cr} - t_{coh}} \tag{2.15}$$

$$HCS = \frac{T_{0.99} - T_{cr}}{t_{0.99} - t_{cr}} \tag{2.16}$$

In Katgerman's approach, t_{coh} is the time at which the semisolid reaches the coherency point, $t_{0.99}$ the time at which the solid fraction becomes 0.99, and t_{cr} the time at which Feurer's criterion is met, i.e., $ROF = ROS$. In Hatami's model, $T_{0.99}$ and $t_{0.99}$ are the temperature and time at a 0.99 solid fraction, and T_{cr} and t_{cr} are the temperature and time when $ROF = ROS$.

2.4 Strain Rate-Based Criteria

Throughout the years, Prokhorov's approach [22] has been one of the most widely used methods to assess solidification cracking. An experimentally-determined ductility curve (temperature-dependent critical strain function), as schematically shown in Fig. 2.5, must be available for hot cracking evaluation. See also section 2.1.

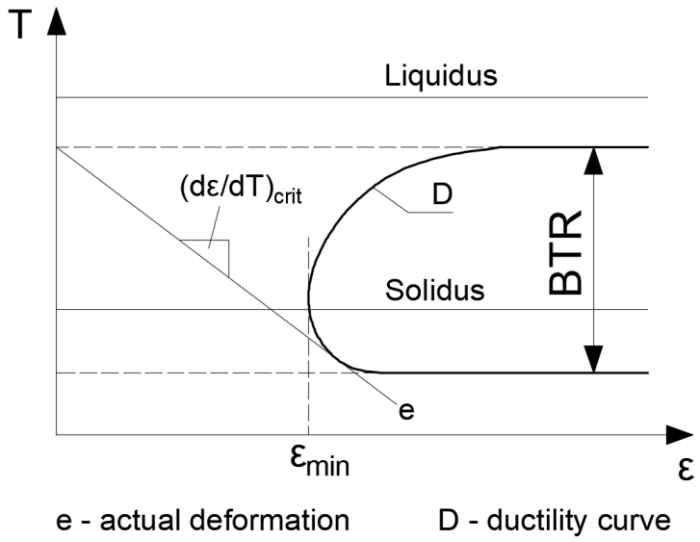

Fig. 2.5: Solidification cracking according to Prokhorov. Adapted from [22].

According to Prokhorov's technological strength theory, hot cracking occurs when the total accumulated strain, e, exceeds the ductility curve within the BTR, D. The total strain is given by the sum of the externally-induced strain due to, e.g., the mechanical load produced by substrate fixation, and the internally- or process-induced strain due to, e.g., restrained thermal shrinkage of the solidifying material. This criterion is often regarded as strain-rate-dependent since the ratio of accumulated strain to temperature drop, $d\varepsilon/dT$, is influenced by both strain rate, $d\varepsilon/dt$, and cooling rate, dT/dt, by means of Eq. (2.17).

$$\frac{d\varepsilon}{dT} = \frac{d\varepsilon/dt}{dT/dt} \tag{2.17}$$

Following Feurer's concept of liquid feeding, Rappaz et al. [23] developed a hot tearing criterion that accounts for tensile strain rate perpendicular to grain growth direction and liquid pressure drop in the mushy zone. When the grains undergo tensile strain during solidification, as shown in Fig. 2.6, the feed flow of the remaining liquid into the regions between the growing grains must be high enough to ensure that the liquid pressure at the root of the dendrites does not fall below a cavitation pressure. Otherwise, a void can nucleate and lead to crack initiation. Through Eq. (2.18), the Rappaz-Drezet-Gremaud criterion (RDG) allows estimating the maximum admissible strain rate, before a critical pressure drop is reached:

$$\dot{\varepsilon}_{p,max} = \frac{G_T}{B}\left[\frac{{\lambda_2}^2 G_T}{180\mu(1+\beta)}\Delta p_{crit} - \frac{\beta v_T}{1+\beta}A\right] \tag{2.18}$$

where $\dot{\varepsilon}_{p,max}$ is the maximum strain rate perpendicular to grain growth direction, G_T is the temperature gradient, λ_2 is the secondary dendrite arm spacing, μ is the viscosity of the liquid, β is a solidification shrinkage factor, and v_T is the velocity of the liquidus isotherm. Eq. (2.18) assumes steady state conditions and a uniform strain rate applied to the mushy zone. The critical pressure drop across the mushy zone, Δp_{crit}, is the difference between the metallostatic pressure, p_m, and the cavitation pressure, p_c, as expressed in Eq. (2.19).

$$\Delta p_{crit} = p_m - p_c \tag{2.19}$$

In Eq. (2.18), A and B are the following integrals:

$$A = \int_{T_S}^{T_L} \frac{{f_s}^2}{(1-f_s)^2}\,dT \tag{2.20}$$

$$B = \int_{T_S}^{T_L} \left[\frac{{f_s}^2}{(1 - f_s)^3} \int_{T_S}^{T} f_s \, dT \right] dT \tag{2.21}$$

where f_s is the temperature-dependent solid fraction, i.e., the solidification curve. The terms T_L and T_S are the liquidus temperature and the temperature at the end of solidification, respectively.

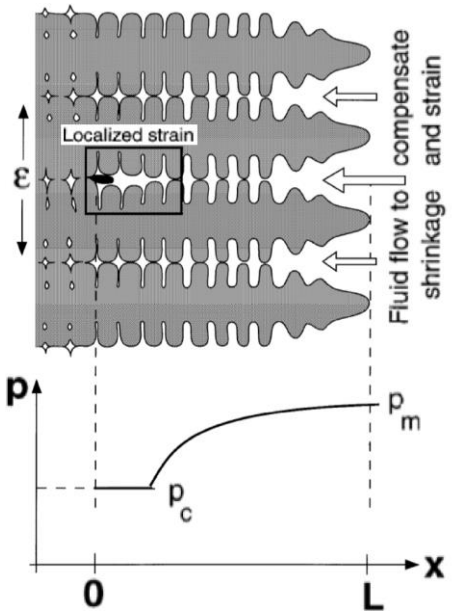

Fig. 2.6: Hot tear formation according to the RDG criterion. Adapted from [23].

The hot cracking susceptibility index is given by Eq. (2.22):

$$HCS = \frac{1}{\dot{\varepsilon}_{p,max}} \tag{2.22}$$

where $\dot{\varepsilon}_{p,max}$ is the maximum strain rate sustainable by the mushy zone. On the basis of the RDG criterion, Braccini et al. [24] developed a more refined model that included the mushy zone rheology.

According to the RDG model, a crack is formed due to cavitation when the liquid pressure falls below a critical value. Nevertheless, as reported in [16], cavitation is unlikely to occur in the mushy zone since the pressure drop produced by thermal strains (10^{-2} to 10^{1} atm) is several orders of magnitude smaller than the pressure drop liquid metals can withstand before collapsing (10^{3} to 10^{4} atm) and too small to significantly contribute to pore formation.

Considering the latter, Kou [25] suggested that cracking may initiate if the separation rate of two neighboring grains caused by tensile strain, subtracted by their rate of growth toward each other, exceeds the feeding rate of liquid along the grain boundary.

2.5 Pore-Based Criteria

According to [16, 26], several experimental observations advise that solidification cracking may originate from preexisting pore nuclei in the liquid. It has also been suggested that dissolved gas in the liquid plays an important role as a source of these nuclei.

Recently, Draxler [26] developed a hot cracking criterion based on preexisting micropores in the grain boundary liquid films (GBLF). A crack initiation index, CII, is defined as follows:

$$CII = \frac{p_f - p}{p_0} \tag{2.23}$$

where p_0 is the atmospheric pressure, p is the liquid pressure at some location in the GBLF without the presence of a pore, and p_f is the external pressure required to balance the surface tension of a pore with radius 50 µm. This particular radius was considered to be that of a pore capable of producing a severe defect; however, no mathematical or physical deduction is provided as to why that exact number was selected. It is assumed there is a risk for cracking when $p < p_f$, i.e., $CII > 0$.

This pore-based criterion was evaluated on Varestraint tests of nickel-based superalloy 718, showing that it can fairly predict crack locations, crack orientations, and crack widths for Varestraint tests.

2.6 Discussion on Hot Cracking Criteria

A few hot cracking criteria were presented in this section, some with perceptible advantages such as simplicity of implementation, but also shortcomings. For instance, strain- and stress-based criteria demand the determination of experimental fracture strain or stress values, respectively, which in practice may prove challenging for materials such as nickel superalloys due to the high temperatures involved during solidification. In the case of CM247LC, stress-strain curves can be found up to 1373 K (1100 °C) [27, 28], which is roughly 180 K below the equilibrium solidus.

In the technological strength approach, the emphasis is placed on externally applied strain and not on local strain because the former is easier to measure. The material is subjected to an external mechanical load (augmented strain) while the weld bead is fused. When a crack is produced, the applied strain is recorded. Nevertheless, it is unclear to what extent the augmented

strain can be used to evaluate the local strain field acting on the small solidifying portion of the material. Upon melting, the stress field is "switched off" within the melt pool, because liquid cannot transmit mechanical stress. As a result of this stress discontinuity between the melt pool and the substrate, the relationship between local strains developing during solidification and the augmented strain comes into question. Furthermore, the critical strain values obtained from technological strength tests such as Varestraint or Trans-Varestraint tests, and the resulting ductility curves, are highly dependent upon the process parameters. Consequently, their applicability is very limited when considering criteria such as Prokhorov's [22].

Based on the assumption that solidification cracking originates from preexisting voids in the GBLF, an interesting pore-based criterion has been proposed by Draxler [26]. A deep analysis must be conducted to assess the applicability of this criterion to PBF-LB/M. In addition, pore generation sources need to be defined or clarified. Draxler's approach was evaluated in Varestraint tests on nickel-based superalloy 718, using TIG welding with a track speed of 1 mm/s. The obtained weld beads were about 5 mm wide and it was assumed that a crack formed when a pore reached a diameter of 100 µm, which was estimated to occur in approximately 2 s. In PBF-LB/M, however, the scan speed is at least one or two orders of magnitude higher, the resulting beads are usually tens or up to hundreds of micrometers wide, cracks can originate and develop within milliseconds, and their length can be as small as, for example, 10 µm.

From the observation of the different theories and criteria, it could be argued that the feeding-shrinkage concept of Feurer has been considered in several hot cracking criteria, including those proposed by Clyne and Davies [20], Katgerman [20], Hatami et al. [16], Rappaz et al. [23], Braccini et al. [24], and Kou [25]. The use of this approach is particularly appealing for this study, since it can be easily implemented in FVM-based simulation tools such as OpenFOAM, and it also permits the consideration of mechanical effects in addition to fluid flow interactions. A more detailed look at Feurer's criterion is provided in the next section.

3 Evaluation of Solidification Cracking

The present work investigates solidification cracking based on Feurer's shrinkage-feeding theory, which suggests that cracking can occur when the rate of liquid feeding into a control volume, ROF, is less than the volume's shrinkage rate, ROS. With increasing solid fraction, the interdendritic space becomes smaller and fluid flow may be hindered to the point where not enough liquid is available to fill any remaining gaps between growing grains. This can produce microporosity or initiate a solidification crack. The competition between liquid feeding and solidification shrinkage is illustrated in Fig. 2.4, where the intersection point between these two rates should be at the lowest temperature possible in order to reduce the risk of cracking.

In Feurer's original approach, generally categorized as non-mechanical, the feeding rate is estimated using Eq. (2.7), which was derived from Darcy's law to describe the flow through the mushy zone, considering it a porous medium and assuming dendritic growth as the morphology of the solidification front (the equation is a function of the secondary dendrite arm spacing). Yet, depending on cooling rate and temperature gradient, cellular growth has been reported to be very common in processes such as LPBF and laser welding [5]. The latter limits the applicability of Eq. (2.7), which also requires previous knowledge of parameters that can be difficult to determine experimentally, e.g., the tortuosity of the mushy zone. For the rate of shrinkage, Feurer proposed Eq. (2.12), which assumes that contraction is determined solely by the change in material density during solidification, neglecting mechanically induced deformations within the mush.

In lieu of applying Eqs. (2.7) through (2.12) as found in section 2.3, an alternative strategy is proposed here for the numerical implementation of this criterion. In fact, the aforementioned equations are not required since the available multi-physical solver [9 - 12] provides all the necessary parameters for the calculation of the two rates that make up Feurer's criterion. On the one hand, the rate of feeding, ROF, is estimated from the divergence of the liquid velocity field, considering a more general model for fluid flow through porous media. Unlike Feurer's liquid feeding equation, this model requires the determination or calibration of a single parameter, namely, the permeability of the mushy zone. On the other hand, the rate of shrinkage, ROS, is obtained from a thermo-mechanical model, accounting not only for volume contraction due to density change during solidification, but also due to mechanical strains.

Most mechanical hot cracking approaches contemplate stresses and strains outside the mushy zone, where the material is completely solid. Here, the evolution of the strain field over time within the mushy zone is estimated and taken into account for the evaluation of hot cracking. Differently from Feurer's original theory, the approach proposed in this work combines mechanical and non-mechanical aspects involved in the solidification process.

3.1 Rate of Feeding

The flow of liquid volume entering or leaving a control volume, V, is estimated using the divergence of the velocity, $\boldsymbol{u}$. Mathematically, the divergence of the vector field $\boldsymbol{u}(\boldsymbol{x})$ at a point $\boldsymbol{x_0}$ within the control volume is given by

$$\operatorname{div} \boldsymbol{u}\,(\boldsymbol{x_0}) \equiv \lim_{V \to 0} \frac{1}{V} \int_{\partial V} \boldsymbol{u} \cdot \boldsymbol{n}\, d\Omega \tag{3.1}$$

The latter is just another form of the Gauss theorem, where ∂V is the closed boundary of V and $d\Omega$ is a surface differential. The vector $\boldsymbol{n}$, which provides the orientation of a given surface of the control volume, is a unit vector pointing out of the control volume. Thus, a positive divergence value means a net flow outward, while a negative value represents a net flow into the control volume.

It is important to note that the fluid mechanics formulation here is compressible, with the continuity equation reading as follows:

$$\operatorname{div}(\rho \boldsymbol{u}) + \frac{\partial \rho}{\partial t} = 0 \tag{3.2}$$

Since the density ρ varies with time and position, especially during solidification, the divergence of the velocity field for a closed control volume is not necessarily equal to zero.

In three-dimensional Cartesian coordinates, the divergence of $\boldsymbol{u}$ can be written as

$$\operatorname{div} \boldsymbol{u} = \nabla \cdot \boldsymbol{u} = \frac{\partial u_1}{\partial x_1} + \frac{\partial u_2}{\partial x_2} + \frac{\partial u_3}{\partial x_3} \tag{3.3}$$

The rate of liquid feeding, ROF, is then defined as

$$ROF = \left(\frac{\partial \ln V}{\partial t}\right)_{feeding} \equiv -f_l \operatorname{div} \boldsymbol{u}, \qquad \operatorname{div} \boldsymbol{u} < 0 \tag{3.4}$$

where f_l is the liquid fraction. The latter is introduced in Eq. (3.3) to account for the divergence caused solely by liquid motion. ROF has units of s^{-1}, which is consistent with Eq. (2.7).

The governing equations employed to derive the velocity field $\boldsymbol{u}$ include a source term, $\boldsymbol{S}$, which modifies the momentum equations in the mushy region to model fluid flow through a porous

medium [29]. This source term is shown in Eq. (3.5), where μ is the liquid dynamic viscosity, f_s is the solid fraction, κ is the permeability of the mushy zone, and δ is a constant introduced to avoid division by zero. The latter is set to 10^{-6}. As the solid fraction increases, the permeability decreases until it reaches a value of zero when the mush has solidified completely. The variation of permeability with solid fraction can be found in [30] for an aluminum alloy. There, the predicted value of permeability varies from $10^{-9.8}$ to $10^{-12.5}$ m^2 when f_s increases from 0.3 to 0.9. In this work, κ will be assumed constant and equal to 10^{-12} m^2.

$$\boldsymbol{S} = -\frac{\mu}{\kappa}\frac{{f_s}^2}{(1-f_s)^3+\delta}\boldsymbol{u} \tag{3.5}$$

3.2 Rate of Shrinkage

In PBF-LB/M, a given transverse cross section of a freshly fused bead can be fully solidified in just a few milliseconds (or less). Furthermore, depending on the process conditions, the physical distance between the solidus and the liquidus isothermal surfaces can vary up to tens or a few hundred micrometers. Because of the short duration and small spatial extent of the mushy zone, it is challenging to predict and validate its mechanical behavior. In technological approaches such as Noviko's [15] and Prokhorov's [22], strains during solidification are considered to evolve linearly with temperature; see for example Fig. 2.2(a) and Fig. 2.5. For simplicity, this study will assume linear thermo-elasticity as the constitutive law governing the stresses and strains within the mushy zone.

Each volume element is treated as an isotropic, linear-thermoelastic solid, with temperature- and phase-dependent properties. For such a case, the Duhamel-Neumann constitutive relation, which is an extension of Hooke's law to account for thermal loading [31], takes the form

$$\boldsymbol{\sigma} = \lambda \operatorname{tr}\boldsymbol{\varepsilon}\,\boldsymbol{I} + 2G\boldsymbol{\varepsilon} - (3\lambda + 2G)\alpha\Delta T\boldsymbol{I} \tag{3.6}$$

where $\boldsymbol{\sigma}$ is the Cauchy stress tensor, λ is the first Lamé constant, G is the second Lamé constant (shear modulus), $\boldsymbol{\varepsilon}$ is the infinitesimal strain tensor, $\boldsymbol{I}$ is the unit tensor, α is the linear Coefficient of Thermal Expansion (CTE), and ΔT is the difference between the current temperature, T, and a reference temperature, T_{ref}. In Eq. (3.6), the total strain $\boldsymbol{\varepsilon}$ consists of mechanical strain, $\boldsymbol{\varepsilon}^{mech}$, and strain caused by free thermal expansion (or contraction), $\boldsymbol{\varepsilon}^{th}$.

The first and second Lamé constants are related to the bulk modulus, K, and the Poisson's ratio, ν, through Eqs. (3.7) and (3.8), respectively. Also, the bulk modulus can be expressed as a function of the elastic modulus (Young's modulus), E, and the Poisson's ratio, ν, as shown in Eq. (3.9). These last two parameters are more often measured experimentally.

$$\lambda = \frac{3K\nu}{1+\nu} \tag{3.7}$$

$$G = \frac{3K(1-2\nu)}{2(1+\nu)} \tag{3.8}$$

$$K = \frac{E}{3(1-2\nu)} \tag{3.9}$$

For the displacement vector field, $\boldsymbol{D}$, in linear elasticity theory it holds

$$\boldsymbol{\varepsilon} = \nabla \boldsymbol{D}^S = \frac{1}{2}(\nabla \boldsymbol{D} + \nabla \boldsymbol{D}^T) \tag{3.10}$$

and thus,

$$\operatorname{tr} \boldsymbol{\varepsilon} = \operatorname{tr} \nabla \boldsymbol{D} \tag{3.11}$$

Using Eqs. (3.10) and (3.11), and recognizing that $K = \lambda + 2G/3$, Eq. (3.6) can be rewritten as

$$\boldsymbol{\sigma} = \lambda \operatorname{tr} \nabla \boldsymbol{D}\, \boldsymbol{I} + G\nabla \boldsymbol{D} + G\nabla \boldsymbol{D}^T - 3K\alpha\Delta T \boldsymbol{I} \tag{3.12}$$

Taking into account the small increments of stress components between opposite faces of a differential volume element, and neglecting the effect of body forces, the equilibrium conditions provide the local form of the linear momentum equation [32]:

$$\nabla \cdot \boldsymbol{\sigma} = \rho \dot{\boldsymbol{v}} = \rho \frac{\mathrm{d}}{\mathrm{d}t} \boldsymbol{v} = \frac{\mathrm{d}^2}{\mathrm{d}t^2} \boldsymbol{D} \tag{3.13}$$

where ρ is density, and $\boldsymbol{v}$ is the rate of change of the displacement vector field. Introducing Eq. (3.12) in Eq. (3.13), the next expression is obtained:

$$\rho \frac{\mathrm{d}^2}{\mathrm{d}t^2} \boldsymbol{D} = \nabla \cdot (\lambda \operatorname{tr} \nabla \boldsymbol{D}\, \boldsymbol{I} + G\nabla \boldsymbol{D} + G\nabla \boldsymbol{D}^T - 3K\alpha\Delta T \boldsymbol{I}) \tag{3.14}$$

Based on a sequentially coupled thermal-stress analysis (weakly coupled analysis), i.e., assuming that the thermal history affects the mechanical behavior but not vice versa, Eq. (3.14) is solved for $\boldsymbol{D}$ at each time step after the multi-physics solver provides the temperature field, T. Subsequently, $\boldsymbol{\varepsilon}$ and $\boldsymbol{\sigma}$ are computed using Eq. (3.10) and Eq. (3.12), respectively.

For small deformations, the unit volume change of an infinitesimal volume element in three-dimensional Cartesian coordinates is given by

$$e_V = \frac{\Delta(\mathrm{d}V)}{\mathrm{d}V} = \varepsilon_{11} + \varepsilon_{22} + \varepsilon_{33} = \mathrm{tr}\,\boldsymbol{\varepsilon} = \mathrm{div}\,\boldsymbol{D} = \frac{\partial D_1}{\partial x_1} + \frac{\partial D_2}{\partial x_2} + \frac{\partial D_3}{\partial x_3} \tag{3.15}$$

where ε_{ii} are the diagonal components of the infinitesimal strain tensor [33]. This unit volume change, e_V, is known as dilation. Considering the variation of the strain tensor over time, $\dot{\boldsymbol{\varepsilon}}$, one can estimate the rate of dilation as follows:

$$\frac{\mathrm{d}e_V}{\mathrm{d}t} = \frac{\mathrm{d}}{\mathrm{d}t}(\mathrm{tr}\,\boldsymbol{\varepsilon}) = \mathrm{tr}\,\dot{\boldsymbol{\varepsilon}} = \mathrm{div}\,\boldsymbol{v} = \frac{\partial v_1}{\partial x_1} + \frac{\partial v_2}{\partial x_2} + \frac{\partial v_3}{\partial x_3} \tag{3.16}$$

Finally, the rate of shrinkage (volumetric contraction), ROS, is given by

$$ROS = \left(\frac{\partial \ln V}{\partial t}\right)_{shrinkage} \equiv -\,\mathrm{div}\,\boldsymbol{v} = -\,\mathrm{tr}\,\dot{\boldsymbol{\varepsilon}}, \qquad \mathrm{tr}\,\dot{\boldsymbol{\varepsilon}} < 0 \tag{3.17}$$

ROS has units of s^{-1}, which is consistent with Eq. (2.12) or Eq. (2.13).

3.3 Hot Cracking Susceptibility

According to Feurer, solidification cracking is possible when the following condition is met:

$$ROF < ROS \tag{3.18}$$

A hot cracking susceptibility index is proposed here to provide further quantitative depth to the application of Feurer's theory. This index is based on the volume fraction of the elements meeting the ROF-ROS criterion. Once the melt pool and mushy zone have reached a quasi-constant shape, the susceptibility to hot cracking is quantified as follows:

$$HCS = \frac{\sum_{i=1}^{n} V_i}{\sum_{j=1}^{N} V_j} \tag{3.19}$$

where V_j is the volume of each element j in the risky region (risky temperature range) formed by N elements (sample size), V_i is the volume of each element i within the risky region that actually satisfies Eq. (3.18), and n is the total number of elements i. If all volume elements within the risky region are the same size, Eq. (3.19) becomes simply $HCS = n/N$.

The sample size can be defined in different ways. Recalling the shrinkage-brittleness theory of Pumphrey and Jennings [14], the upper and lower limits of the "effective interval" are the coherency temperature and the solidus, respectively. In this work, N is given by the number of solidifying elements within this temperature range.

3.4 Further Considerations

As shown in Eqs. (3.3) and (3.17), feeding and shrinkage rates are influenced by the divergence of two vector fields: the fluid velocity, $\boldsymbol{u}$, and the rate of change of displacement ("velocity") of solid particles, $\boldsymbol{v}$, respectively. It is worth noticing that the former comes from the thermofluid solution (fluid mechanics), while the latter is obtained from the thermomechanical model (solid mechanics).

For the application of the linear thermoelastic model, it is assumed that the same elastic modulus, E, applies to both loading states tension and compression. Furthermore, E is considered independent of strain rate, although it has been shown that elastic behavior may be sensitive to this parameter [34]. In this case, given that it is highly complex to obtain reliable material properties to account for the dependency of elastic modulus on strain rate, it might not be worth adding this complexity to the model. It is also pertinent to mention that, despite using a linear thermomechanical model, non-linearities can generally arise from different sources, e.g., temperature- and phase-dependent material properties, non-linear heat sources, among others.

Mechanical stress and strain are expected to be present only in the substrate and in that portion of the material undergoing solidification, whose solid fraction exceeds 0.6. The latter is assumed to be the solid fraction at which the semisolid reaches the coherency temperature, T_{coh}. Details on coherent temperature estimation are presented in section 4.4.

In the thermomechanical model, a reference temperature, T_{ref}, must be defined to quantify the effect of thermal expansion and contraction. For volume elements that remain solid throughout the process, the reference temperature is the initial temperature, which can be room temperature or higher if the substrate is preheated. For that part of the material that melts and then resolidifies, T_{coh} is taken as the reference temperature after melting.

4 Numerical Simulation Model

The formulated solidification cracking criterion is assessed with the aid of single-track simulations of laser sintered CM247LC nickel superalloy, using a multi-physical numerical model developed in OpenFOAM [35]. The simulation model employs the Finite Volume Method (FVM) to solve the systems of coupled partial differential equations and the Volume of Fluid (VOF) approach to estimate the dynamics of free boundaries [9 - 12]. Although this solver is typically used for fluid dynamics problems, its capabilities are extended to include the thermomechanical model described in section 3.2. This chapter presents the simulation model used, as well as the properties of the studied material.

4.1 Simulation Model

A schematic of the OpenFOAM geometry is shown in Fig. 4.1. In order to minimize computational expenses, only a small rectangular block is considered for the single-track simulations.

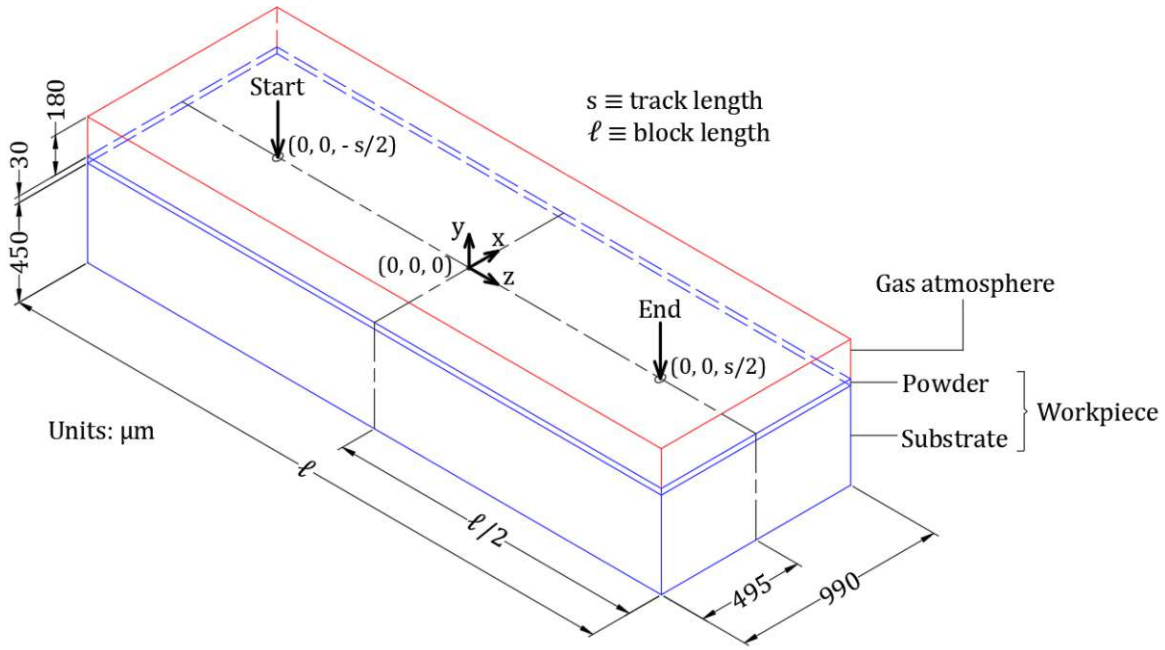

Fig. 4.1: Geometry in OpenFOAM.

The workpiece consists of substrate and powder, which are of the same material: CM247LC. Instead of modeling powder particles and their interactions, a continuum with powder-like properties is proposed for the powder bed. In PBF-LB/M, nitrogen or argon are normally used

as oxidation protective atmospheres. Since no chemical reactions are being simulated, the properties of air are assigned to the surrounding gas.

The coordinate system origin is at the top of the powder layer, which is 30 µm thick. The "Start" and "End" arrows indicate the start and end coordinates of the laser's linear path. The geometry is chosen to cover the full extent of the melt pool and allow it to reach a nearly constant shape within the laser path.

To investigate the effect of preheating on solidification cracking, simulations are performed using different initial temperatures, namely 25 °C (room temperature), 500 °C, and 1000 °C. Since the length of the melt pool is affected by the preheating temperature, suitable track lengths, s, are selected for each case: 2 mm, 3 mm, and 5 mm, respectively. The corresponding substrate lengths, ℓ, are 3.00 mm, 3.99 mm, and 6.00 mm, respectively. A summary of the boundary and initial conditions of the model's main variables can be found in Table 4.1.

Table 4.1: Boundary and initial conditions for the main variables

Variable	Uniform internal field (Initial condition)	Boundary condition [36]
Solid displacement, $\boldsymbol{D}$ (m)	(0 0 0)	AT [a]: zeroGradient WP [b]: fixedValue = (0 0 0)
Fluid velocity, $\boldsymbol{u}$ (m)	(0 0 0)	AT: fluxCorrectedVelocity WP: noSlip
Temperature, T (K)	298.15 w/o preheating 773.15 or 1273.15 w/ preheating	AT: inletOutlet (initial value of internal field as inlet value) WP: zeroGradient

[a] AT: faces of the atmosphere
[b] WP: faces of the workpiece

At the beginning of the simulations, substrate, powder, and surrounding atmosphere are in thermodynamic equilibrium, i.e., at the same initial temperature. The maximum time step for the numerical solution is set to 5e-6 s (0.005 ms). The simulations employ dynamic mesh refinement to provide better resolution within the melt pool and near region. As shown in Fig. 4.2, the initial mesh consists of cubic volume elements evenly distributed throughout the entire computational domain, each with a side of 30 µm. With three levels of refinement, the smallest cubic cells obtained during the simulations have a side length of 3.75 µm.

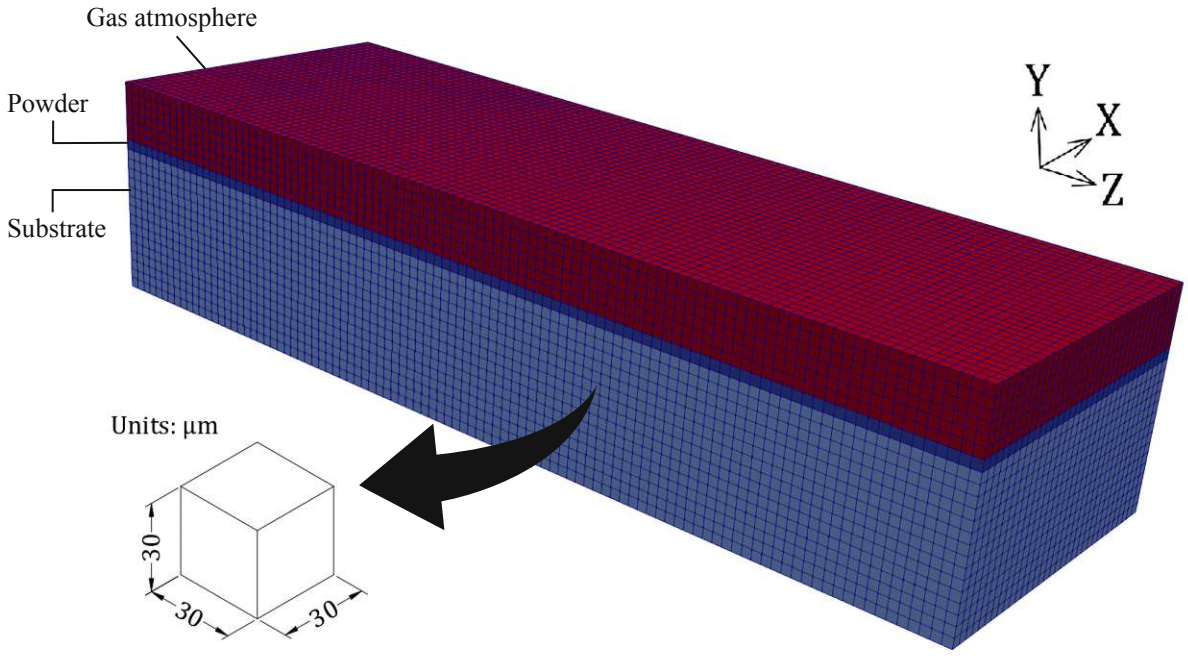

Fig. 4.2: Initial mesh.

4.2 Process Parameters

The parameters used in the simulations are summarized in Table 4.2. These parameters were drawn from [37 - 39], which is a compilation of studies conducted at the Institute of Machine Tools and Manufacturing (IWF) of ETH Zürich on a SLM (Selective Laser Melting) laboratory machine equipped with 200 W water-cooled infrared (1070 nm) fiber lasers. In these studies, the investigated materials were stainless steel 316L and nickel superalloy CM247LC.

Table 4.2: Process parameters

Parameter	Value
Scan speed	1000 mm/s
Input power	200 W
Target total absorbed power	128 W (64% of input power [39])
Spot type	Gauss
Laser wavelength	1070 nm
Spot diameter at beam waist	90 µm
Focus vertical coordinate	0 mm
Thickness of powder bed	30 µm

The total absorbed power shown in Table 4.2 is a reference value extracted from the simulation analyses presented in [39]. For similar process conditions as those described above, it was found that most of the incoming laser power is absorbed within the melt pool and a keyhole-like depression located at the front of the melt pool, where the absorptivity is high due to multiple beam reflections. According to [39], the evaporation of material at the front of the melt pool results in a recoil pressure on the melt pool's surface, which induces a strong downward and rearward flow, pushing the melt away from the area of highest temperature. The latter generates the aforementioned keyhole-like dent.

4.3 Material Properties

This subchapter summarizes the most simulation-relevant properties of nickel superalloy CM247LC, whose nominal composition is shown in Table 4.3. In OpenFOAM, the volume of fluid (VOF) method uses a species transport equation to determine the relative volume fraction of the predefined phases (solid, powder, liquid, metal vapor, surrounding gas) in each computational cell [36]. In the present study, all physical properties of each cell are calculated as a linear weighted average based on the volume fractions mentioned above.

Table 4.3: Nominal composition of CM247LC powder in wt% [37]

C	Cr	Co	W	Mo	Ta	Al	Ti	Hf	B	Zr	Ni
0.06	8.4	9.4	9.6	0.5	3.3	5.6	0.8	1.4	0.01	0.009	Bal.

4.3.1 Thermophysical Properties

Phase transition temperatures and enthalpies

Alloys melt and solidify over a temperature range whose lower and upper limits are the solidus and liquidus temperatures, respectively. The difference between these two temperatures during cooling is called the solidification or freezing range, which depends on alloy composition and cooling rate. As reported in [40], local equilibrium between the liquid and solid phases at the solidification interface might be maintained for cooling rates up to 10^3 K s^{-1}. At higher cooling rates, non-equilibrium solidification occurs, and the solidus temperature shifts to lower values. Table 4.4 shows some estimated solidification range values and liquid-solid phase transition temperatures reported for alloy CM247LC under both, thermodynamic equilibrium and non-equilibrium assumptions.

Table 4.4: Reported liquid-solid phase transition temperatures and estimated values for the solidification range of nickel superalloy CM247LC

	Equilibrium conditions				Non-Eq. solidification		
Solidus (K)	N/A	1552	1530	1570	N/A	N/A	1200
Liquidus (K)	1645	1646	1658	1645	N/A	N/A	1669
Solidification range (K)	N/A	94	128	75	~225	~325	469
Method[a]	DSC[b] cooling	DSC heating	TC[c] TCNI5	TC TTNI8	TC-S[d] TCNI8	TC-S TTNI8	TC-S TCNI9
Reference	[41]	[42]	[42]	[42]	[28]	[28]	[43]

[a] Method used to estimate the phase transition temperatures and/or solidification range.
[b] Differential Scanning Calorimetry (DSC) during cooling or heating.
[c] ThermoCalc® equilibrium simulation using data base XXNIX.
[d] ThermoCalc® non-equilibrium simulation under Scheil assumptions using data base XXNIX.

Due to uncertainties in the results produced during cooling in the Differential Scanning Calorimetry (DSC) experiment, the solidus temperature of Ni-based alloy CM247LC is often estimated during heating from the onset of melting [41, 42]. The DSC is performed at cooling or heating rates on the order of 10^1 K min^{-1}. This experimental technique cannot replicate the extremely high cooling rates typical of PBF-LB, which can reach up to 10^8 K s^{-1} [5, 44]. To estimate the solidification paths at such high cooling rates, computational simulations using non-equilibrium transformations (e.g., the Scheil-Gulliver model) are usually employed.

As seen in Table 4.4, the solidification range for CM247LC can vary from roughly 100 K in conditions of thermodynamic equilibrium to approximately 500 K when non-equilibrium solidification is assumed, depending on the solidification model and alloy database used for the simulations. The effect that rapid cooling has on the solidification path is also represented in Fig. 4.3, where Ni-based superalloy Hastelloy-X (HX) is given as an example [45]. Due to the high cooling rates produced in PBF-LB, non-equilibrium solidification could play an important role in the analysis of hot cracking, given that this phenomenon is believed to occur during the last stage of solidification.

In this work, however, equilibrium solidification is assumed as a first approximation to investigate the problem of hot cracking. Table 4.5 shows the selected values for the phase transition temperatures and enthalpies of Ni-based alloy CM247LC.

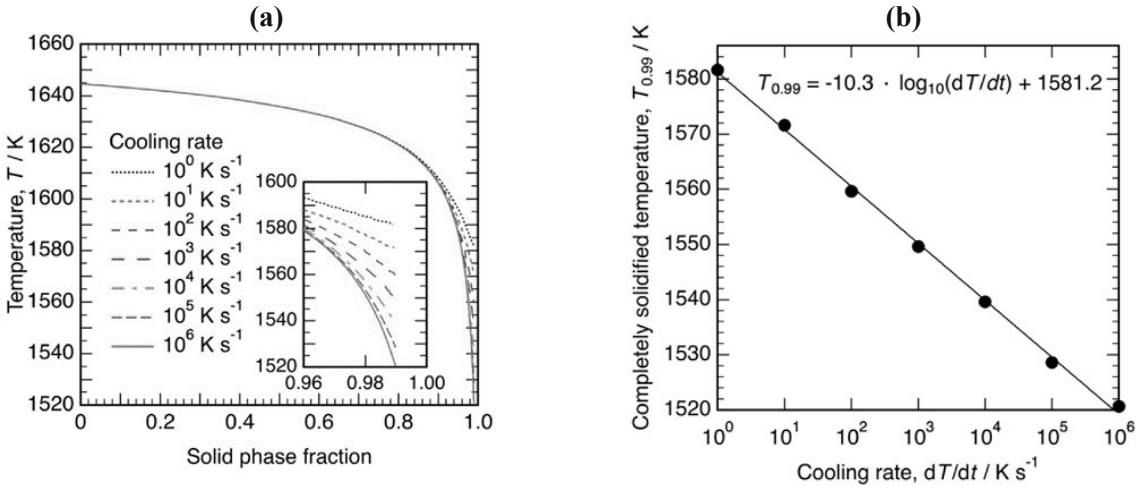

Fig. 4.3: (a) Solidification paths of HX superalloy obtained from modified Scheil-Gulliver simulations using various cooling rates. (b) Temperature at which 99% of the alloy is solidified ($T_{0.99}$) as a function of the cooling rate. Adapted from [45].

Table 4.5: Selected phase transition temperatures and enthalpies of CM247LC [37]

Property	Value
Solidus temperature (K)	1555
Liquidus temperature (K)	1641
Solidification range (K)	86
Evaporation temperature (K)	3213
Enthalpy of fusion (kJ kg^{-1})	264
Enthalpy of evaporation (kJ kg^{-1})	6697

Density

Fig. 4.4 provides an overview of the temperature-dependent density of alloy CM247LC. Both the density of the material in the solid state, i.e., substrate, workpiece or resolidified material, and the density of the liquid phase are estimated according to the method described in [46], using the chemical composition from Table 4.3. The powder bed density is assumed to be 50% of the substrate density, as suggested in [47] for general SLM. For comparison, Fig. 4.6 also shows the experimental density values reported in [48] for a Ni-based alloy similar to CM247LC. To model the density of the gas phase, the alloy vapor is treated as an ideal gas with a molar mass of 59.8 g mol^{-1}; the latter is calculated from the composition in Table 4.3 and the

molar mass of each element. Density values outside the temperature range shown for each phase are assumed to be constant and equal to the end values. This applies to all properties described in this chapter.

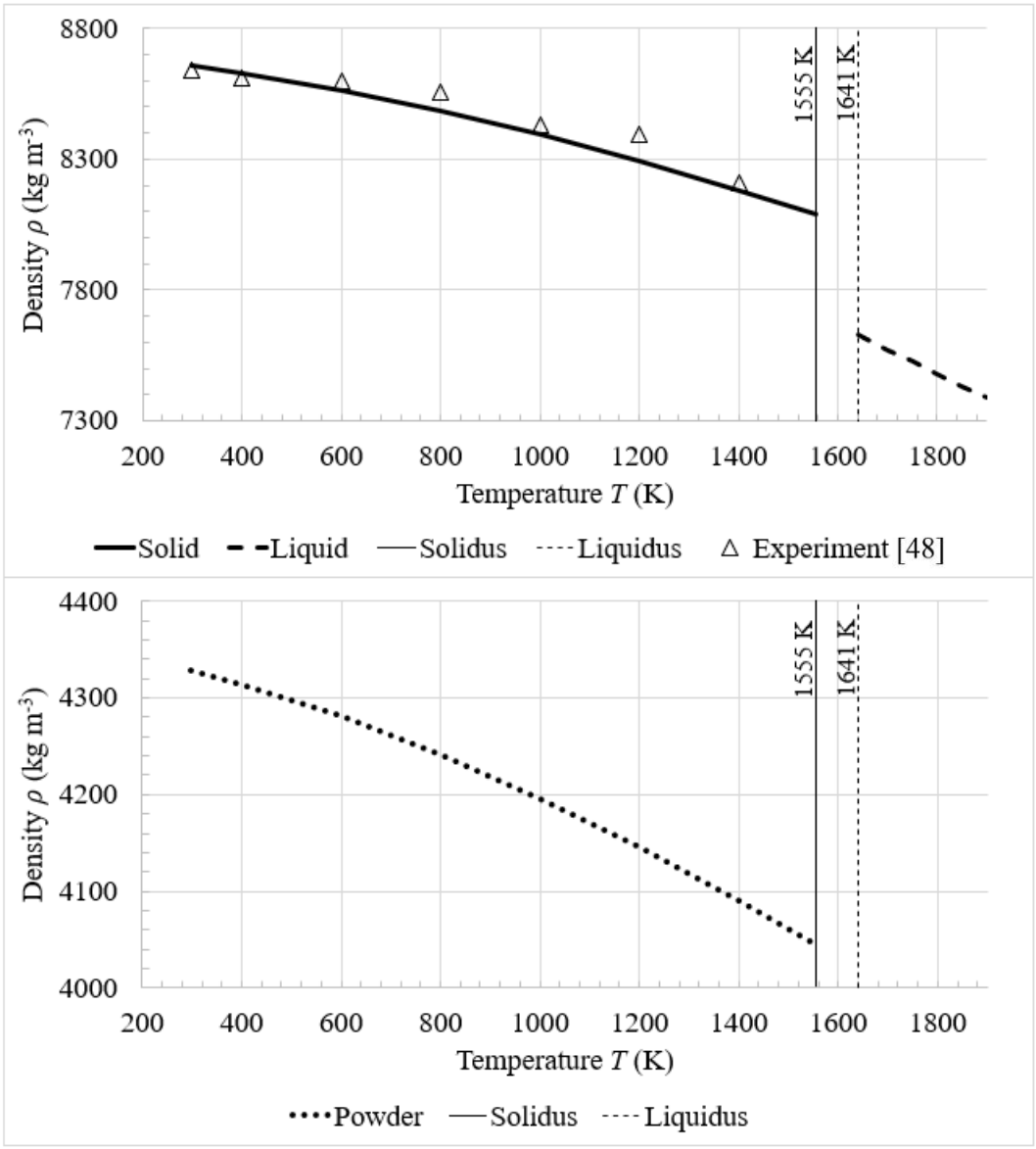

Fig. 4.4: Density.

Specific heat capacity

Fig. 4.5 shows the specific heat capacity as a function of temperature. Due to their similar aluminum content, the values recommended in [46] for nickel superalloy CMSX4 are assumed to be the same for alloy CM247LC; heat capacity is a function of the aluminum content in Ni-based superalloys [46]. Experimental values for the solid state can also be found in [48] for temperatures ranging from 298 K to 1400 K. The metallic powder is considered to have the

same heat capacity as the substrate [49]. For the alloy gas phase, the heat capacity values are assumed to be the same as those reported for iron in the *NIST Chemistry WebBook* [50].

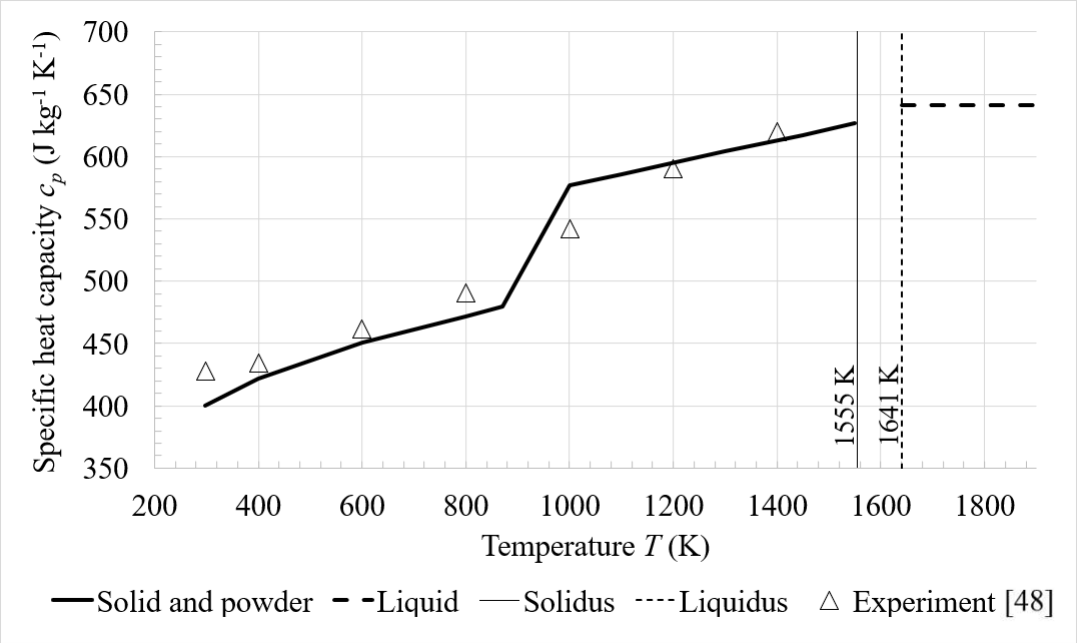

Fig. 4.5: Specific heat capacity.

Thermal conductivity

Fig. 4.6 includes the thermal conductivity values reported in [46] for the solid phase at temperatures ranging from 298 K to 1550 K. For the liquid phase, a constant conductivity of 33.6 W/(m K) is assumed. The conductivity k_p of the metallic powder is estimated using the model developed by Sih [51], as presented in Eq. (4.1):

$$k_p = k_f \left[\left(1 - \sqrt{1-\phi}\right)\left(1 + \phi \frac{k_r}{k_f}\right) + \sqrt{1-\phi}\left(\frac{2}{1-\frac{k_f}{k_s}} \left(\frac{2}{1-\frac{k_f}{k_s}} ln \frac{k_s}{k_f} - 1 \right) + \frac{k_r}{k_f} \right) \right] \tag{4.1}$$

where k_f is the thermal conductivity of the gas surrounding the powder particles, ϕ is the porosity of the powder bed, k_s is the conductivity of the solid, and k_r is the heat transfer due to radiation between the individual powder particles. The latter is calculated through Eq. (4.2), where σ is the Boltzmann constant and D_p is the average diameter of the powder particles.

$$k_r = \frac{4}{3} \sigma T^3 D_p \tag{4.2}$$

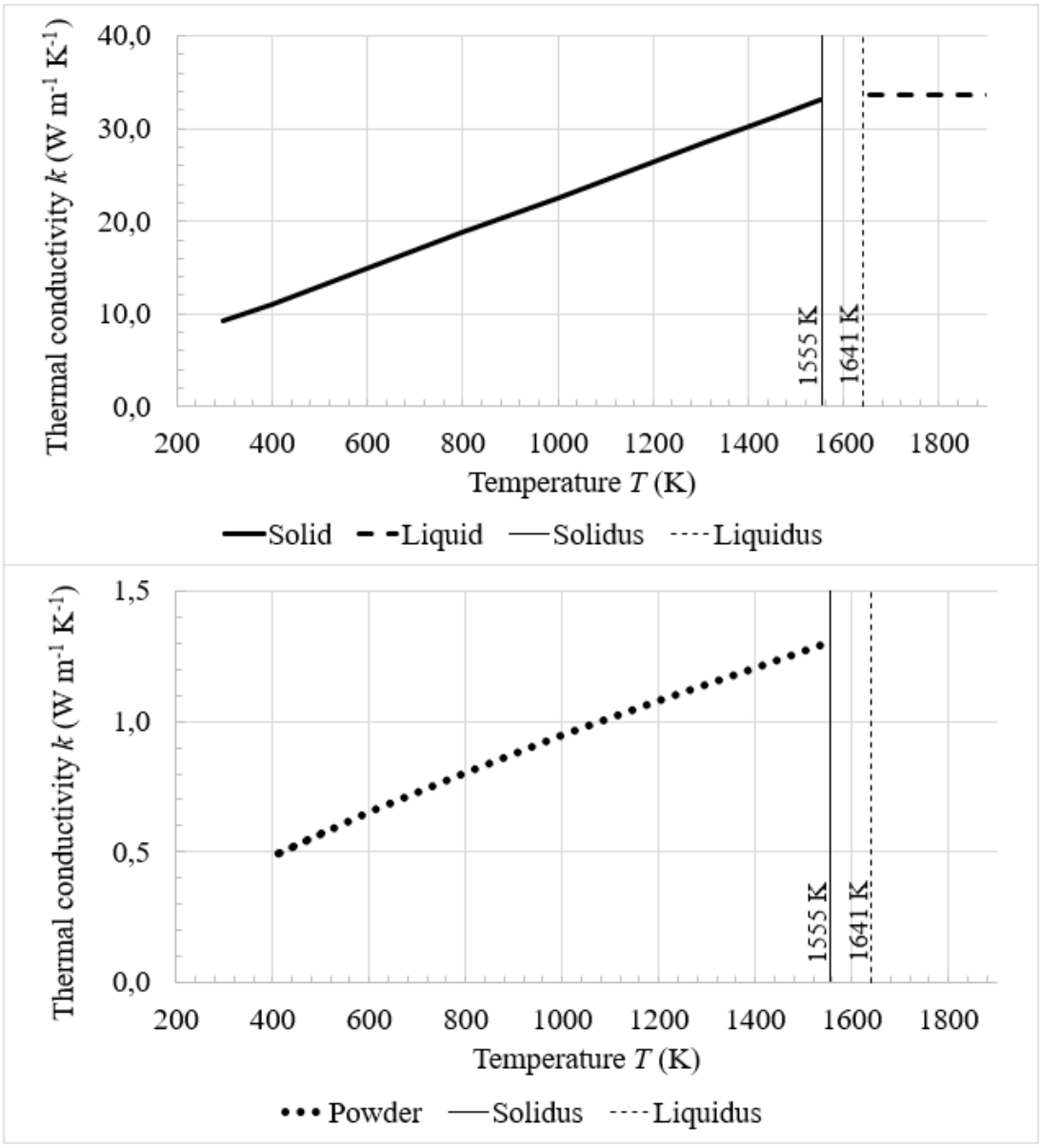

Fig. 4.6: Thermal conductivity.

It is assumed that the alloy gas phase has the same thermal conductivity as argon, which is estimated using Eq. (4.3) proposed in [52]:

$$k_v = \frac{\sqrt{T}}{1000}\left(\frac{a_1}{T} + a_2 + a_3 T\right) \tag{4.3}$$

where k_v is the thermal conductivity in W m^{-1} K^{-1}, T is the vapor temperature in K, and a_i are constants equal to -1.125 · 10^2, 1.354, and 1.453 · 10^{-4}, respectively.

Viscosity and surface energy

Mills et al. [46] recommend Eq. (4.4) for estimating the viscosity of Ni-based alloys, where μ is the dynamic viscosity in mPa s, T is the temperature in K, Y_i is the mass percentage of element i, and Y_{heavy} is the total mass percentage of heavy elements (W, Mo, Ta, and Hf are here considered). The chemical composition presented in Table 4.3 is used for the calculation.

$$log_{10}\,\mu = \frac{2570}{T} - 0.8224 + 1.75 \cdot 10^{-3} Y_{Cr} + 1.1 \cdot 10^{-3} Y_{Fe} + 10.2 \cdot 10^{-3} Y_{heavy} \qquad (4.4)$$

To obtain de kinematic viscosity η, μ is divided by the density value at the corresponding temperature. After plotting $ln(\eta)$ as a function of $1/T$ and performing a linear regression, the Arrhenius coefficients η_0 and E_a are estimated using Eq. (4.5):

$$\eta = \eta_0 e^{\frac{E_a}{RT}} \qquad (4.5)$$

where $\eta_0 = 4.06 \cdot 10^{-8}$ m^2 s^{-1} is the kinematic viscosity at $T = T_\infty$, $E_a = 4.44 \cdot 10^4$ J mol^{-1} is the activation energy, and $R = 8.3145$ J mol^{-1} K^{-1} is the gas constant.

With respect to surface energy (surface tension), Fig. 4.7 shows the values reported in [37] for the liquid-gas interface. The surface energy values for the solid and powder phases are selected in such a way that solid-liquid interactions do not exhibit distinctive wetting behavior, while powder-liquid interactions are hydrophilic (perfect wetting behavior).

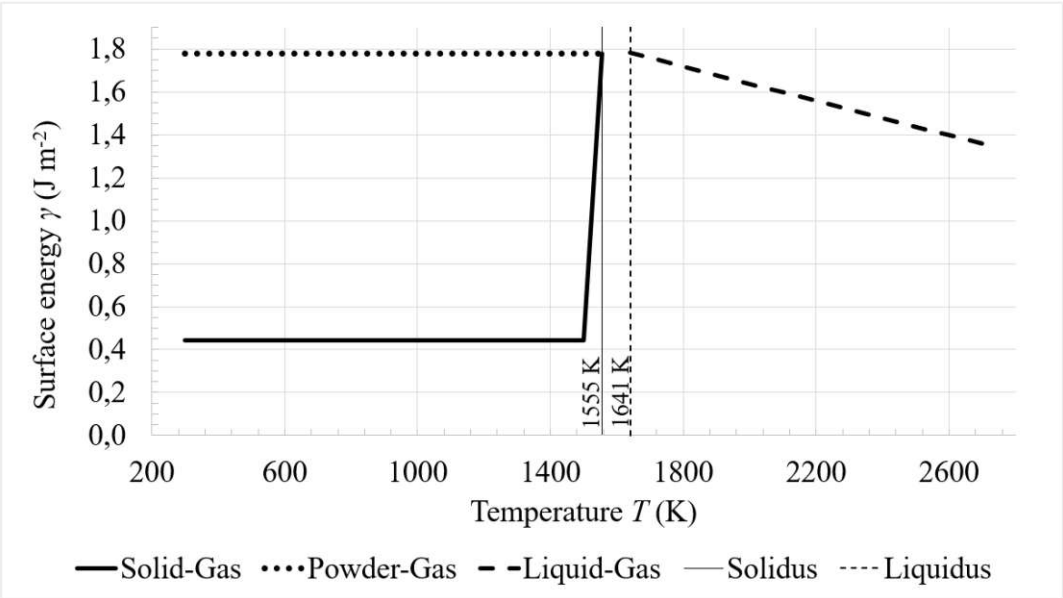

Fig. 4.7: Surface energy.

Solidification curve and coherency temperature

Between the liquidus and solidus temperatures, an alloy is in a semisolid state. According to [15], a semisolid can be distinguished between slurry and mush. A slurry is a liquid with suspended solid particles, while a mush is viewed as a solid network with liquid in between. The transition from slurry to mush occurs at a temperature below which the material becomes capable of withstanding mechanical strain. This temperature is often referred to as the coherency temperature, T_{coh}. The solid fraction corresponding to the coherency temperature varies between 0.25 and 0.6, depending on the morphology of the solid particles [15].

Draxler et al. [53] reported a coherency temperature of 1551 K (1278 °C) for nickel-based superalloy Inconel 718. According to the solidification path published in their work, this temperature corresponds to a solid phase fraction of 0.6. In this study, it is assumed that the coherency temperature of alloy CM247LC also matches a 0.6 solid fraction and, based on the solidification curve obtained from the OpenFOAM solver [9 - 12] (see Fig. 4.8), it is estimated to be 1624 K (1351 °C). This temperature is important for the simulations carried out in OpenFOAM, as it defines the starting point for stress buildup during solidification. The solidification curve was obtained by simulating the one-dimensional Stefan problem, where only the solid and liquid phases were present.

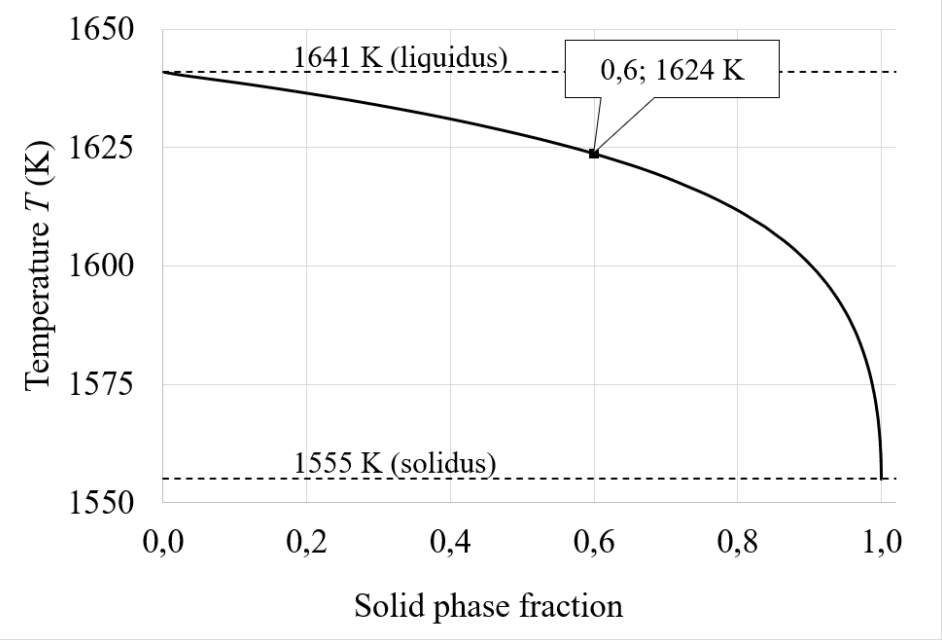

Fig. 4.8: Equilibrium solidification path.

4.3.2 Mechanical Properties

Linear coefficient of thermal expansion

Fig. 4.9 shows the linear CTE (Coefficient of Thermal Expansion), α, of CM247LC. In the solid phase, the CTE is related to the temperature-dependent density through Eq. (4.6):

$$\rho = \rho_{298}[1 + \alpha\,(T - 298)]^{-3} \tag{4.6}$$

where ρ_{298} is the density at 298 K (25 °C) [46]. The CTE is set to zero for the liquid phase, based on the assumption that thermal expansion of this phase produces only liquid flows, but no mechanical deformation [53].

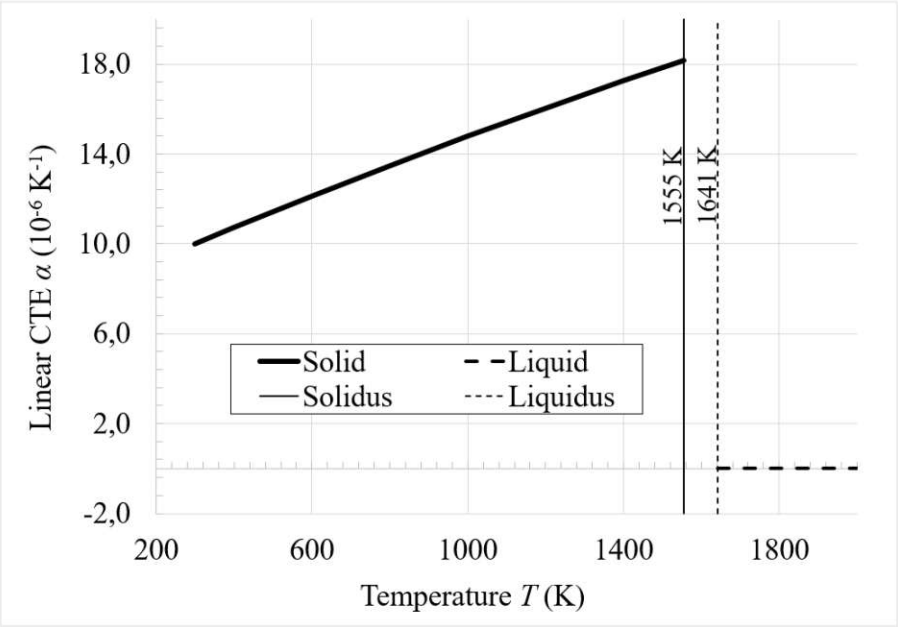

Fig. 4.9: Linear coefficient of thermal expansion.

Elastic modulus and Poisson's ratio

The determination of elastic properties depends on the type of test performed, the test conditions, and sample preparation. For instance, one should differentiate between a conventionally cast, directionally cast, welded, or SLM fabricated sample. The microstructure (and therefore the elastic response) of a PBF-LB "as-fabricated" can be modified by post-processing procedures such as hot isostatic pressing (HIP) or heat treatment. The mechanical properties of the single track may be different from those of the built part, because the workpiece is heat treated as neighboring beads and subsequent layers are deposited; defects are

also introduced throughout the manufacturing process. The microstructure and the level of anisotropy (grain orientation) change permanently during PBF-LB.

According to the simulation results reported in [37] for CM247LC and the parameters presented in Tables 4.2 and 4.5, the transverse cross section of individual tracks produced by PBF-LB consists of elongated grains with a mean width and length of approximately 4 µm and 10 µm, respectively. Stress-strain plots are available in [54] for conventionally cast specimens of alloy Mar-M247LC with mean linear intercept grain size of 60 µm at temperatures of 977 K, 1033 K, and 1088 K. Young's modulus estimates from these data are presented in Fig. 4.10, which also includes values obtained from ultrasonic and nanoindentation experiments at room temperature using CM247LC ingot samples with a fine-grained microstructure [55].

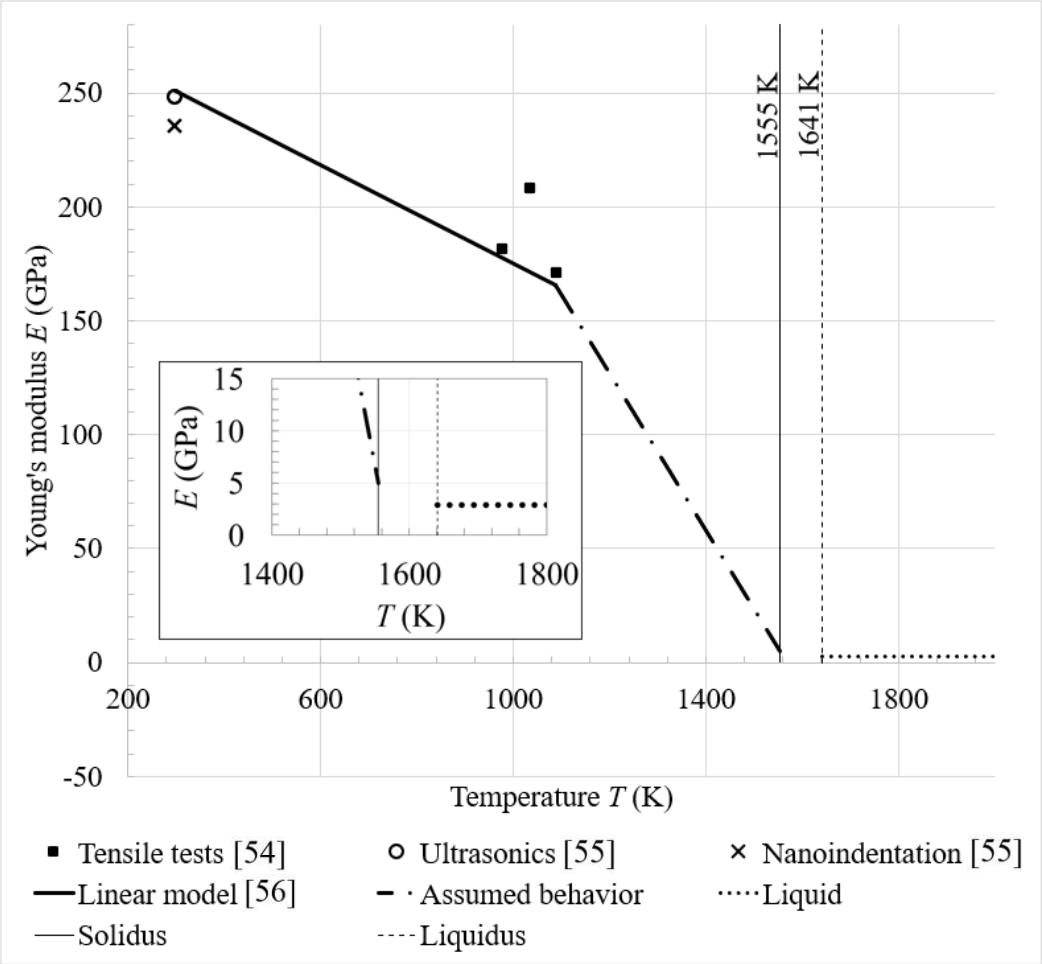

Fig. 4.10: Modulus of elasticity.

In addition, Fig. 4.10 incorporates a linear temperature-dependent model proposed by Sehitoglu and Boismer for alloy Mar-M247, which is expected to have an elastic response similar to that of CM247LC [56]. This model is in agreement with the experimental data from [54] and [55] for temperatures below 1088 K (815 °C). For higher temperatures, no information on the elastic

modulus could be found in the literature. As reported in e.g. [27], CM247LC samples tested at a temperature of 1473 K (1200 °C) failed with very low applied tensile load, so the stress-strain curve could not be determined.

Consequently, the elastic modulus at temperatures near the solidus must be assumed. The linear thermoelasticity hypothesis relies heavily on this assumption. If the elastic modulus is too high at the solidus temperature, the stresses will already exceed the yield point of the material within the mushy zone. This value must be low enough, so that linear thermoelasticity is still possible during alloy solidification. Table 4.6 shows the considered values of elastic modulus and yield stress as a function of temperature. The latter is important to verify if the stresses obtained exceed the elastic region of the material at a given temperature. The Poisson's ratio is assumed to be constant throughout the temperature domain and equal to 0.26 [55].

Table 4.6: Selected elastic properties for CM247LC

	273 K (25 °C)	1088 K (815 °C)	1555 K (1282 °C)	Ref.
Elastic modulus (GPa)	250	165	5[a]	[55]
Yield stress (MPa)	710	693	50[b]	[27]
Poisson's ratio	0.26	0.26[a]	0.26[a]	[55]

[a] Assumed value.
[b] Assumed value, based on the results reported in [27].

With respect to solid mechanics, it is supposed that liquid has a Young's modulus of zero. However, liquid is considered compressible within the fluid mechanical model, and therefore a bulk modulus of ~2 GPa is assumed for liquid phases. For this reason, when converting the bulk modulus into a Young's modulus by means of Eq. (3.9), the liquid phase has a non-zero Young's modulus as observed in Fig. 4.10.

5 Results

This chapter compiles the main findings from single-track simulations of the PBF-LB/M process. First, the resulting temperature field and dimensions of the melt pool and mushy zone are presented for cases with and without preheating, followed by a description of the transverse cross-sectional solidification time and bead morphology. After examining the evolution of mechanical stresses and strains during solidification, the reader is introduced to the parameters associated with the selected hot cracking criterion. Fig. 5.1 provides a general view of the simulated process and the mesh obtained after dynamic refinement.

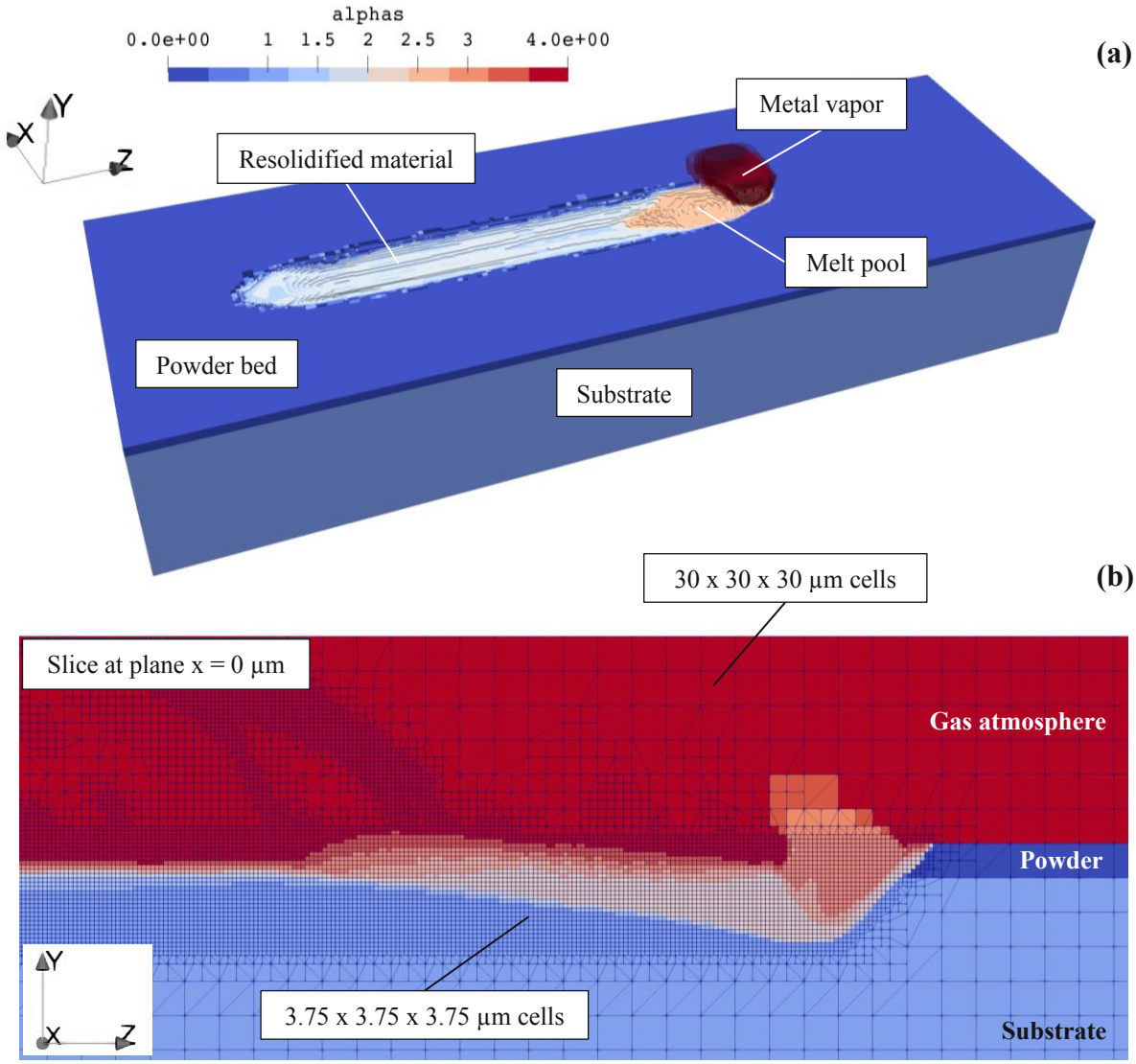

Fig. 5.1: General view of (a) the single-track process and (b) the mesh obtained for the case w/o preheating.

5.1 Melt Pool and Mushy Zone Dimensions

The size and shape of the melt pool and mushy zone are influenced by preheating. This can be seen in Fig. 5.2, which includes cross-sectional views of the temperature field at the longitudinal midplane (x = 0 µm), the substrate's top surface (y = -30 µm), and at a transverse plane at the melt pool's front (section A-A). In general, if the initial temperature of the workpiece is raised, more material is likely to melt with the same amount of energy input, since less heat is required to reach the liquid state. As observed in Fig. 5.2, the spatial extent of the melt pool and mushy zone increase significantly with preheating.

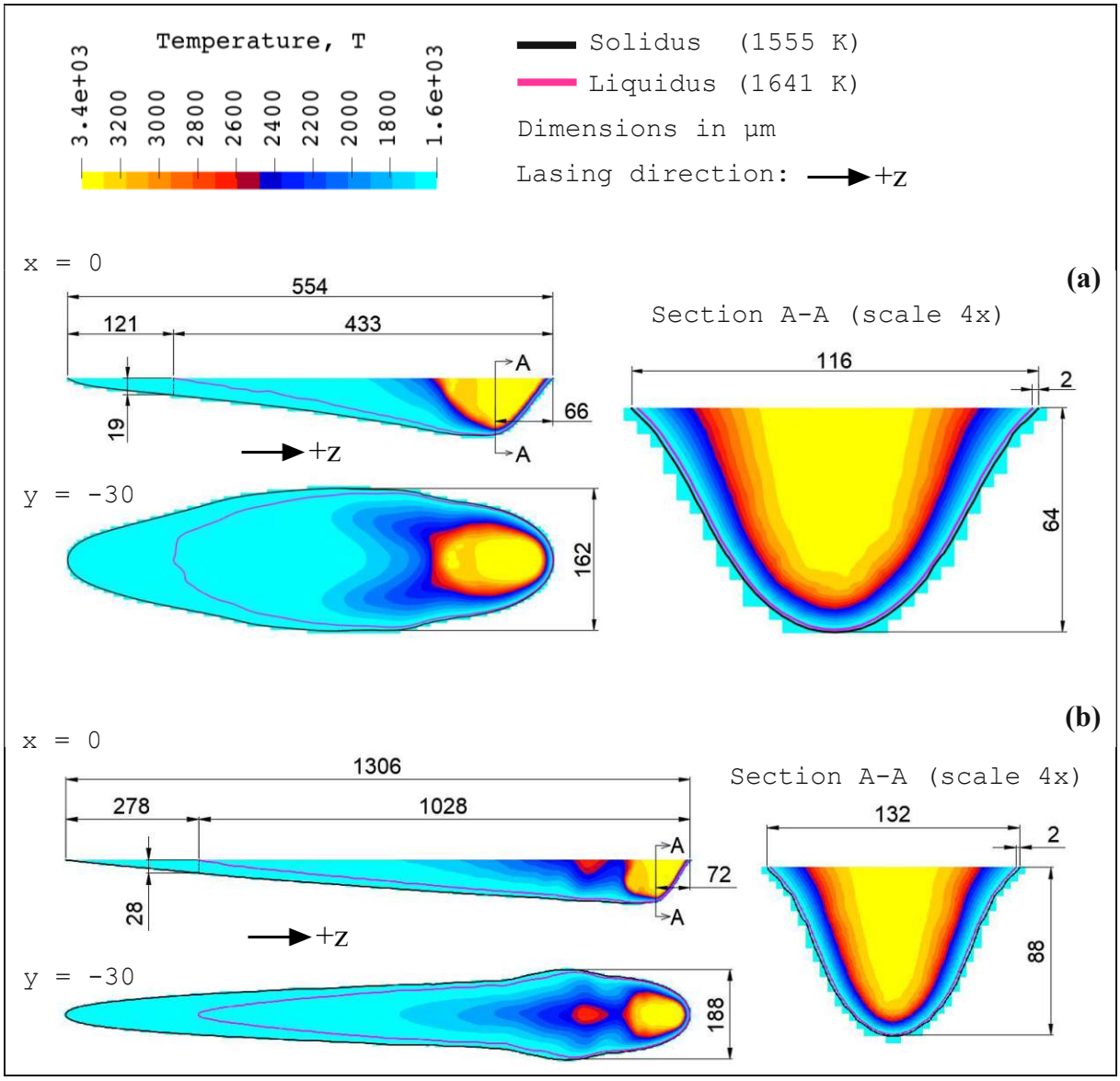

Fig. 5.2: Temperature field and dimensions of melt pool and mushy zone for the cases (a) w/o preheating, and (b) w/ preheating at 500 °C.

The enlargement effect is also attributed to a higher velocity of the backward melt flow originating from the laser beam [57]. Different mechanisms may contribute to this flow, including Marangoni forces, a larger recoil pressure due to increased evaporation, and buoyancy-related effects. At the tail of the melt pool, the flow is mainly driven by natural convection, which depends on the density gradients (or temperature gradients) within the liquid.

From the measurement of the widest and deepest dimensions of the solidus contour, the aspect ratio (depth/width) is estimated to be 0.40 for the case without preheating, and 0.47 with preheating at 500 °C. Although the obtained aspect ratios would suggest a conduction welding mode, the total absorbed power obtained from the simulations is approximately 60% and 70% of the input power, respectively, which is above typical values for pure conduction regime in laser welding, e.g., 30%. The latter is due to a keyhole-like depression caused by sustained evaporation at the melt pool's front, increasing laser reflections within this region and thus the energy absorbed. This effect was also reported in [39], where PBF-LB/M simulations were performed with similar process parameters, obtaining a total absorbed power of 64% (see section 4.2). Moreover, it has been shown that keyholes are present across a broad range of PBF-LB/M processing conditions [58].

Due to the lower temperature difference between the mushy zone and the substrate (lower temperature gradients), preheating hinders conduction heat transfer from the mushy zone to the substrate, thus reducing the cooling rate as shown in Fig. 5.3. Here, the maximum cooling rates obtained within the mushy zone at the substrate's top surface are approximately $1.5 \cdot 10^6$ K/s and $4 \cdot 10^5$ K/s for the simulations w/o preheating and w/preheating at 500 °C, respectively. In both cases, the highest cooling rate values are observed near the solidus at the rear tip of the mush. According to [40], non-equilibrium solidification would occur at these cooling rates.

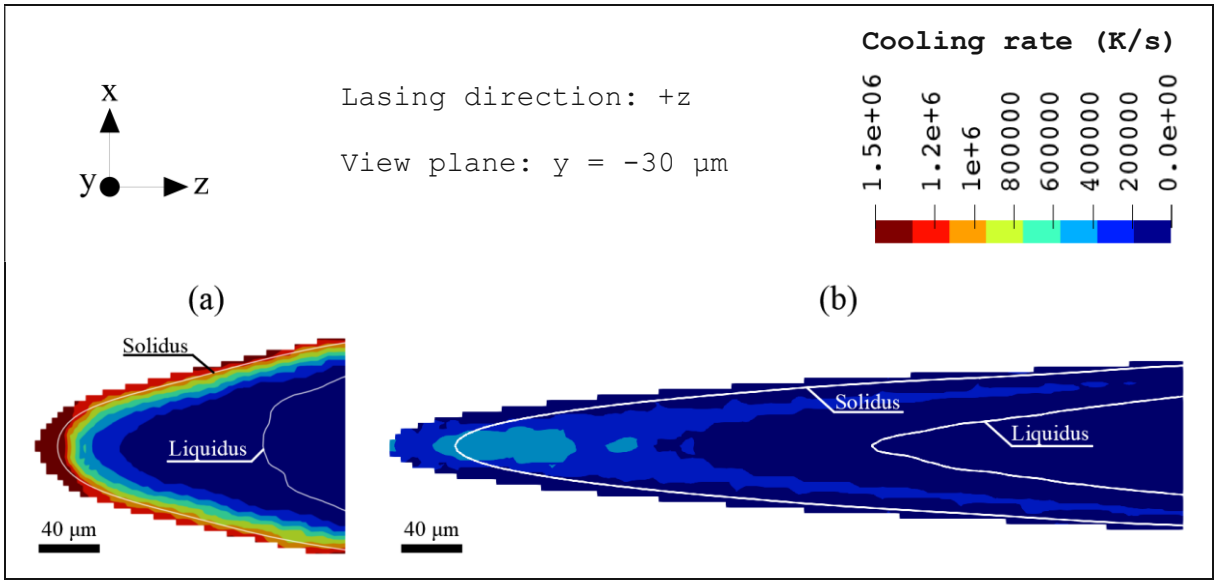

Fig. 5.3: Cooling rate for the cases (a) w/o preheating, and (b) w/ preheating at 500 °C.

5.2 Solidification Time and Bead Morphology

From left to right, Fig 5.4 illustrates the solidification sequence of a fixed cross section perpendicular to the displacement of the laser beam. Three initial conditions are considered: (a) no preheating, (b) preheating at 500 °C, and (c) preheating at 1000 °C. The quantity "alpha" used for coloring is a marker function denoting powder, substrate, liquid, metal vapor, and ambient gas. The regions above the powder are white because the ambient gas was removed from the visualization, not because these regions have an alpha value of 2, which corresponds to liquid. The images were obtained after the melt pool and mushy zone reached a nearly constant shape. The initial time, t_0, corresponds approximately to the instant in which the depression reaches maximum depth.

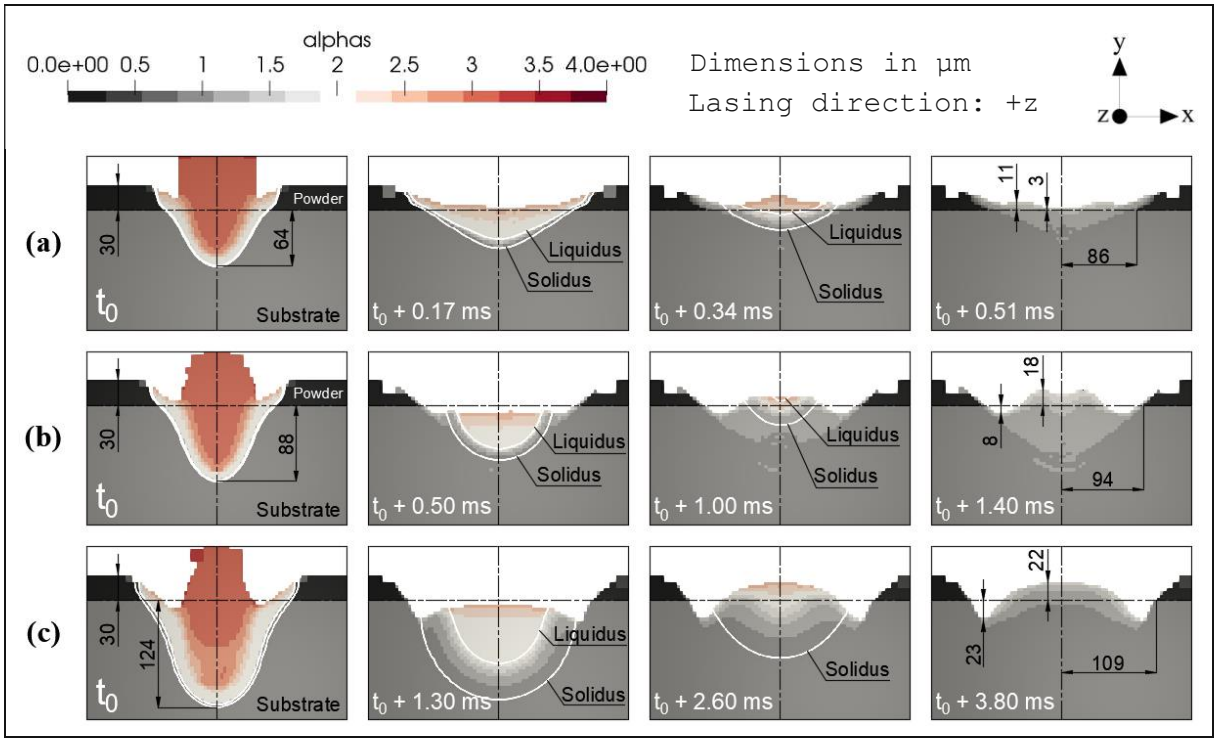

Fig. 5.4: Cross-sectional solidification time and bead morphology for the cases (a) w/o preheating, (b) w/ preheating at 500 °C, and (c) w/ preheating at 1000 °C.

Certainly, a distinguishing feature of the solidification process in PBF-LB/M is its celerity. For the given set of parameters, it takes only half a millisecond for a transverse cross section to fully solidify when no preheating is applied, and approximately four milliseconds when the workpiece is preheated to 1000°C. Fig 5.4 also shows that the distance between solidus and liquidus widens as solidification progresses, and that higher preheating temperatures lead to an increase in the extent of the mushy zone and the depth/width aspect ratio. From the bead shape at the end of solidification, it can be seen that an additional bead height (relative to the top surface of the substrate) is reached when the workpiece is preheated, but at the same time an

"undercut" forms at each side of the bead. The undercuts get deeper with increasing preheating temperature. Similar structures can be seen in X-ray images from single-track experiments published in [57].

The latter implies that the cross-sectional morphology of the beads does not remain constant during the process of printing an entire component, because the workpiece is progressively heated when sintering subsequent beads or adding new layers of material.

5.3 Stress and Strain in the Mushy Zone

After providing a geometrical perspective on the mushy zone and its evolution during solidification, the focus is now shifted to the stresses and strains that develop within this region. Once again, a fixed cross section perpendicular to the displacement of the laser beam is used for this purpose.

Following the upward movement of the mushy zone, Fig. 5.5 shows color maps of raw cell data describing the diagonal components of the stress and strain tensors for the case without preheating, considering three different times during solidification of the bead cross section. These times are chosen within the last third of the total solidification time, which is 0.51 ms according to Fig 5.4, so that the separation between the solidus and coherency temperature isolines is wide enough to allow for acceptable visualization. Recalling section 3.4, dendrite coherency is assumed to be the state at which the mushy zone becomes capable of sustaining mechanical strain. Above this temperature, solid stresses and strains are assumed to be zero. A different color legend is used for each stress and strain component to better perceive the distribution of cell values within the mush. Each color legend is scaled according to the minimum and maximum values present during the time period considered.

As illustrated in Fig. 5.5(a), the three diagonal stress components have a symmetrical arrangement with respect to the longitudinal midplane ($x = 0\ \mu m$), predominantly displaying a state of tension towards the left and right ends of the mushy zone, and compression towards the center. This symmetry is maintained as the mushy zone travels upwards. Looking at the color legends, the component along the transverse direction, x, presents the highest stress values in both tension and compression states.

Likewise, strains exhibit a symmetrical disposition as shown in Fig. 5.5(b). Along the x-axis, where the highest strain magnitudes are found, the mushy zone contracts in the center and stretches in the lateral regions. Along the y-axis is the opposite, i.e., the material contracts at the ends and stretches in the middle, which can be attributed to the Poisson effect. Along the z-axis, the material stretches in all regions of the mushy zone, albeit with relatively low strain values. The latter is also expected, since the modeled workpiece has its largest dimension along z. Tensile strains in the z-direction are largest towards the end of solidification, when the coherency isotherm reaches the top surface.

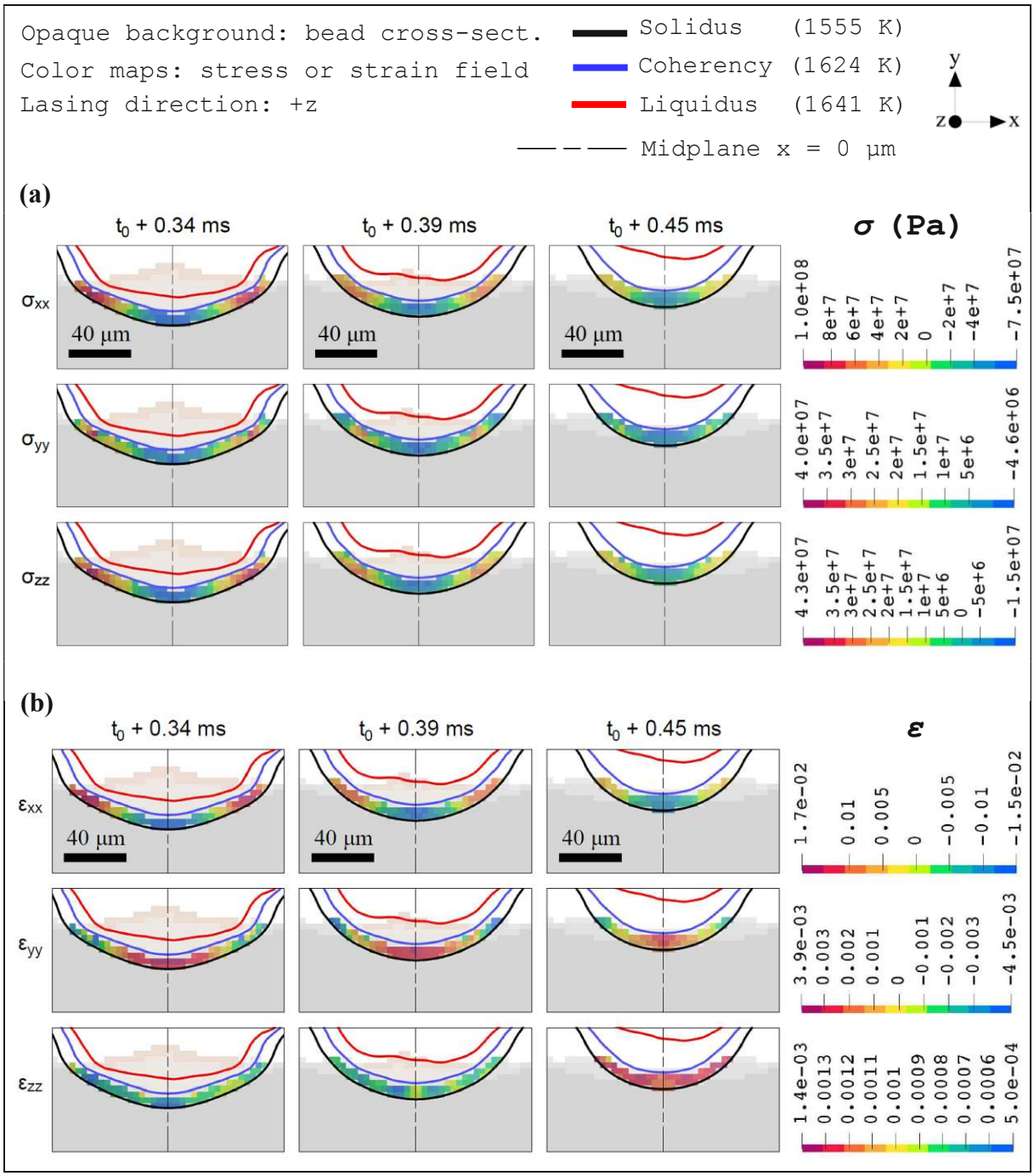

Fig. 5.5: Development of (a) stress and (b) strain in the mushy zone for the case w/o preheating.

To provide a more quantitative perspective on the above images, an isotherm between the solidus and the coherency temperature is selected (1585 K on this occasion) and tracked as it moves with the mushy zone. Figs. 5.6 and 5.7 respectively show the stress and strain values along this isotherm for three different times, which are the same as those considered in Fig. 5.5. Since the arc length of the isothermal line decreases over time, a normalized length is used for ease of comparison. The mush is represented by the black region in the figures mentioned above.

In agreement with the color maps of Fig. 5.5, the symmetrical characteristic of stresses and strains is also observed in Figs. 5.6 and 5.7. The tensile and compressive stresses in the x-direction are more than double those in the y- and z-directions; these last two stress components exhibit similar values along the isotherm. The transition from tension to compression or vice versa (zero stress value) occurs at different locations depending on the observed stress component. As shown in Fig. 5.6, all three components decrease in amplitude as the isothermal line moves in the positive y-direction, suggesting that an observer moving up together with the mushy zone (Lagrangian description) will experience stress relaxation, and that the highest stress values within the mushy zone should be found at deeper positions, closer to the keyhole-like depression. The latter can also be seen in Fig. 5.8, taking σ_{xx} as example.

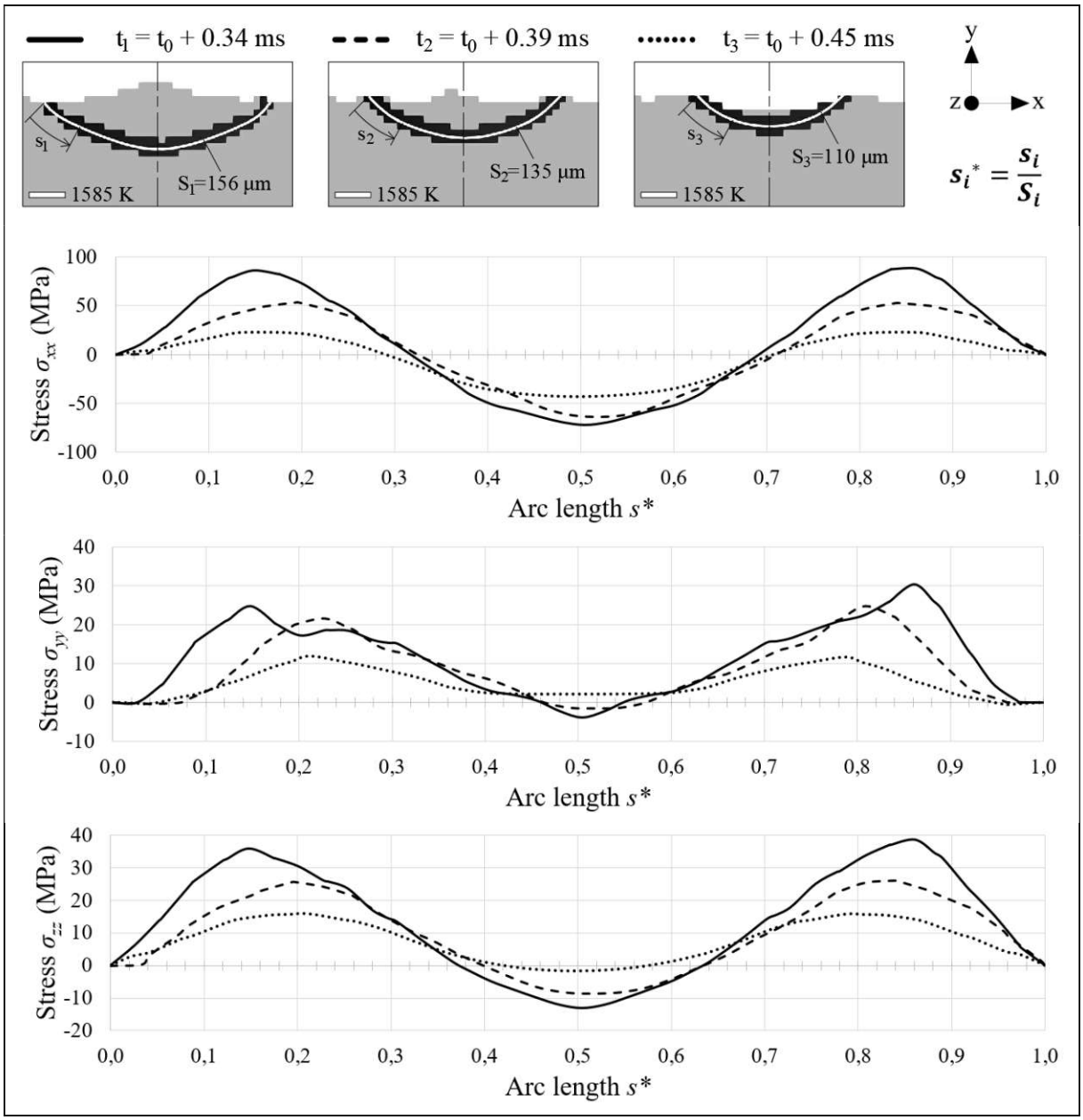

Fig. 5.6: Isothermal stress values within the mush and their evolution over time.

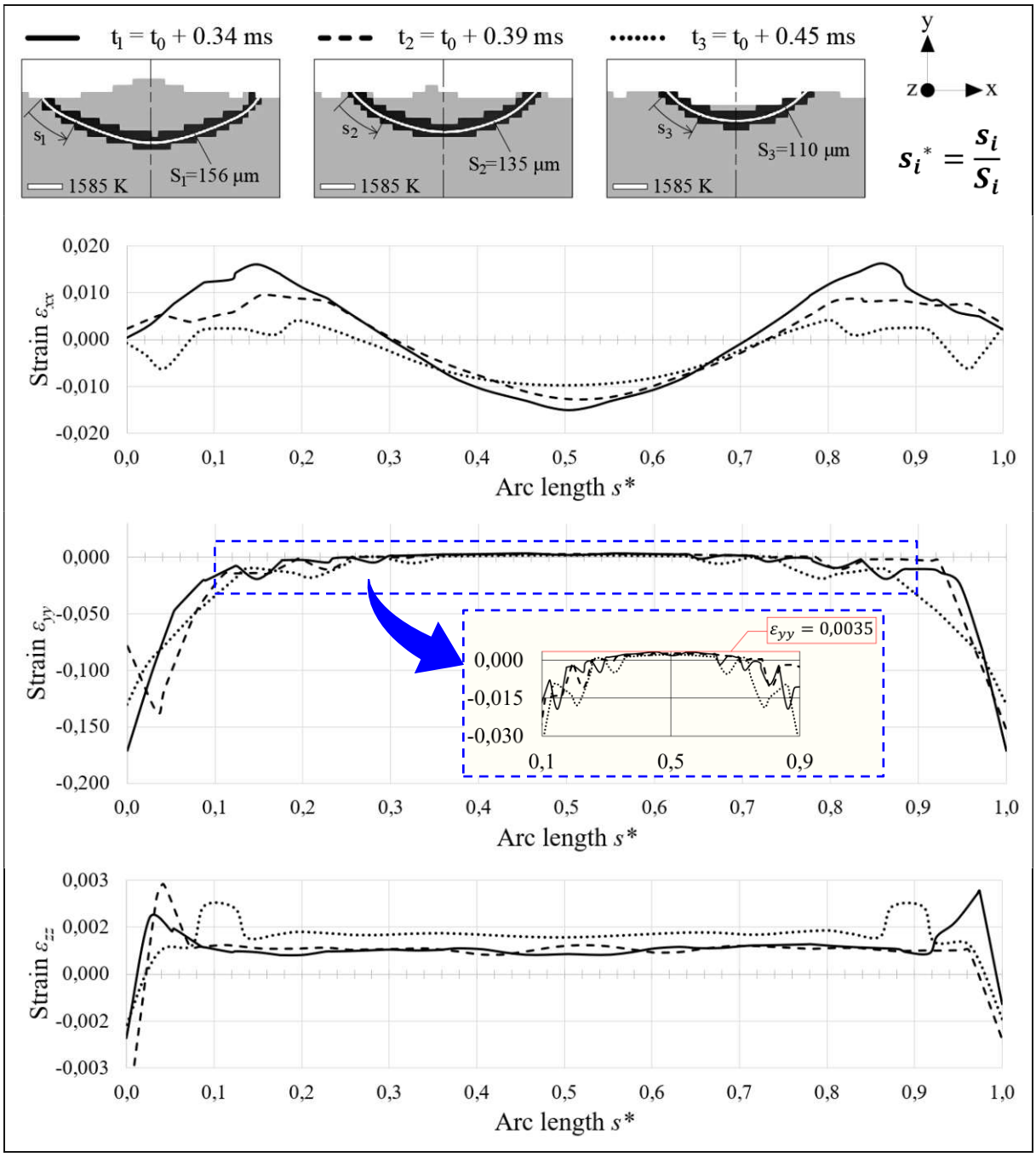

Fig. 5.7: Isothermal strain values within the mush and their evolution over time.

Based on Fig. 5.7, within the first and last 30% of the arc length, the material experiences the largest tensile strains in the x-direction. Towards the center of the isotherm, strains in the y- and z-directions are mainly tensile, but significantly smaller than the tensile strains on the end locations. In the central region, contraction strains in the x-direction are the largest.

As with stresses, strains in the x-direction along the isotherm decrease in magnitude as the mushy zone moves up. A variation can also be observed, although not as strong, for the strains in the y- and z-directions.

Unlike the stress curves in Fig. 5.6, strong fluctuations in strain values are found towards the left and right ends of the isothermal line, where the mush is thinnest. As will be discussed in the next chapter, the strain peaks and oscillations in Fig. 5.7 are an interpolation effect aggravated by the proximity between the isothermal line and cells with high liquid or powder content. This is based on the observation that, with the current numerical implementation, the calculated mechanical strains in the liquid phase (and also in powder) are not zero as they should be, thereby introducing noise into the strains within the solid network of the mushy zone. The latter is relevant for the results involving the *Rate of Shrinkage* (ROS) in the evaluation of hot cracking, since this parameter depends on the trace of the strain rate tensor.

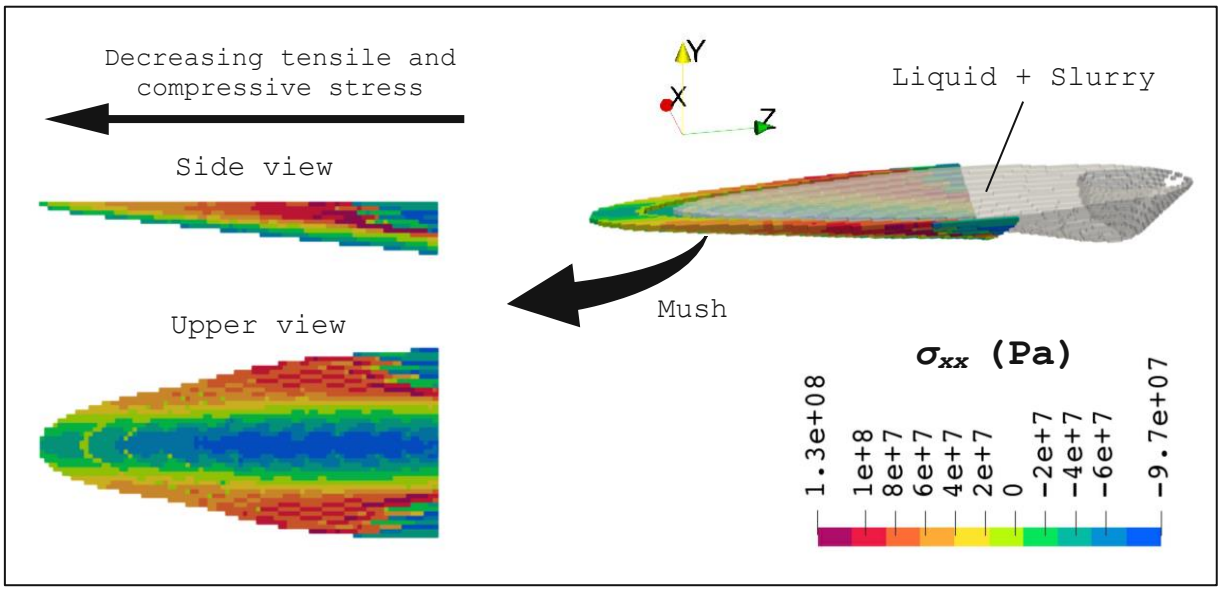

Fig. 5.8: Stress distribution throughout the mush, σ_{xx}.

It is also interesting to observe the evolution of stresses and strains along a fixed line during solidification of the bead cross section. From this Eulerian point of view, Fig. 5.9 shows for the components along the x-axis that stress increases with increasing time (or with decreasing temperature), while strain decreases as the material cools down. Another important remark is that the strain curve becomes smooth when the fixed line is out of the influence of the mush, i.e., when no liquid is present. Within the mush peaks similar to those in Fig. 5.7 are observed. In contrast, stress curves are fairly smooth at all times analyzed. The values presented for stress and strain outside the mushy zone are purely referential and serve only to identify a trend over time. These are not necessarily valid since the assumption of linear thermoelasticity does not apply in this region. The discussion chapter addresses the latter in further detail.

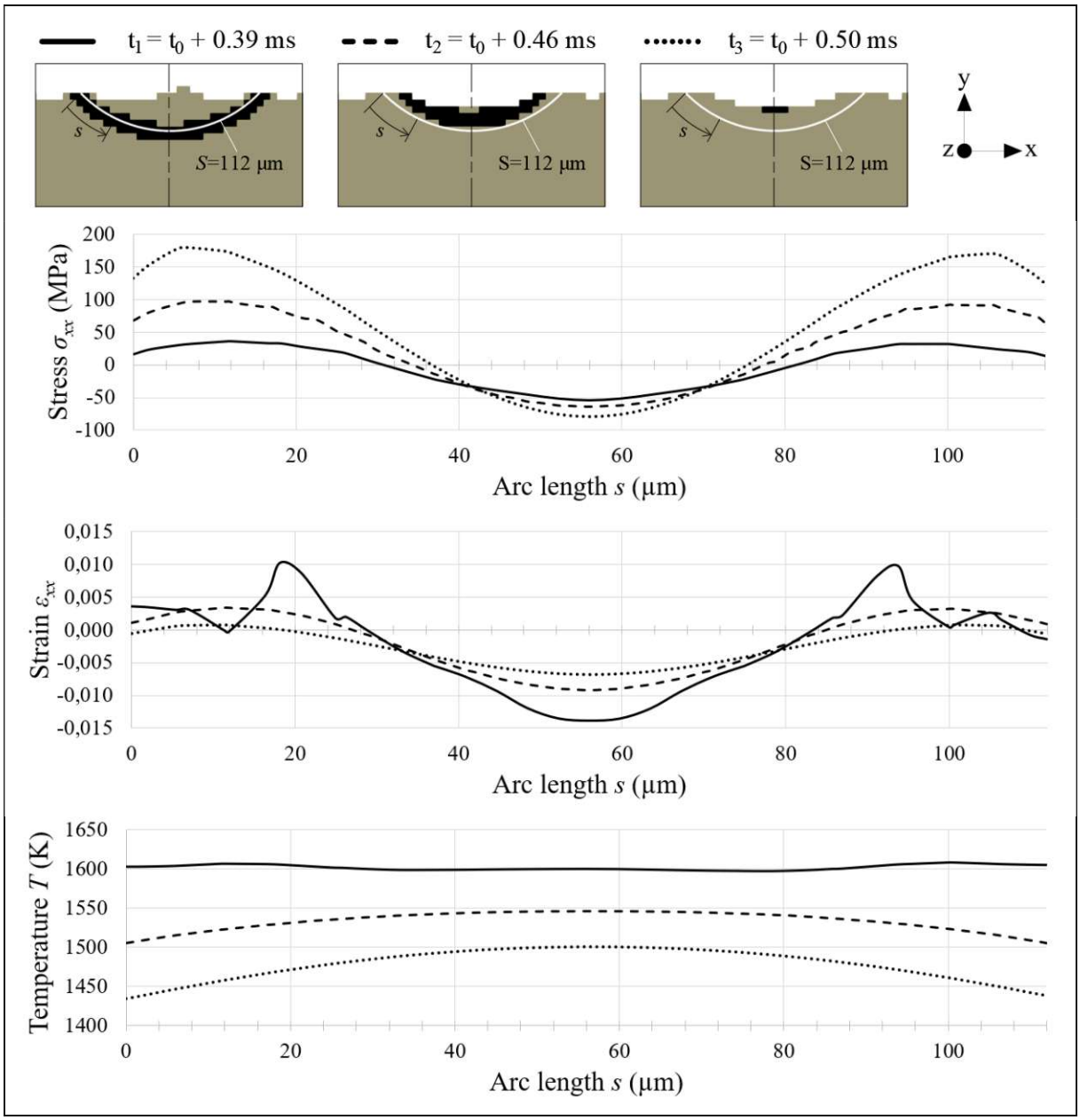

Fig. 5.9: Evolution over time of stress, strain, and temperature along a fixed line.

To identify the effect that preheating has on stress and strain fields, Figs. 5.10 and 5.11 include color maps of σ_{xx} and ε_{xx}, respectively, showing the tail of the mushy zone in the $y = -30\ \mu m$ plane (substrate's top surface) for the cases without preheating and with preheating at 500 °C. The main impact of preheating resides in the reduction of tensile stresses and strains in the lateral regions of the mush (an almost tenfold reduction is observed in this example). Both cases exhibit similar magnitudes of compression stresses and strains in the central region of the mush, with the highest values occurring in the plane of symmetry, close to the coherency temperature isotherm.

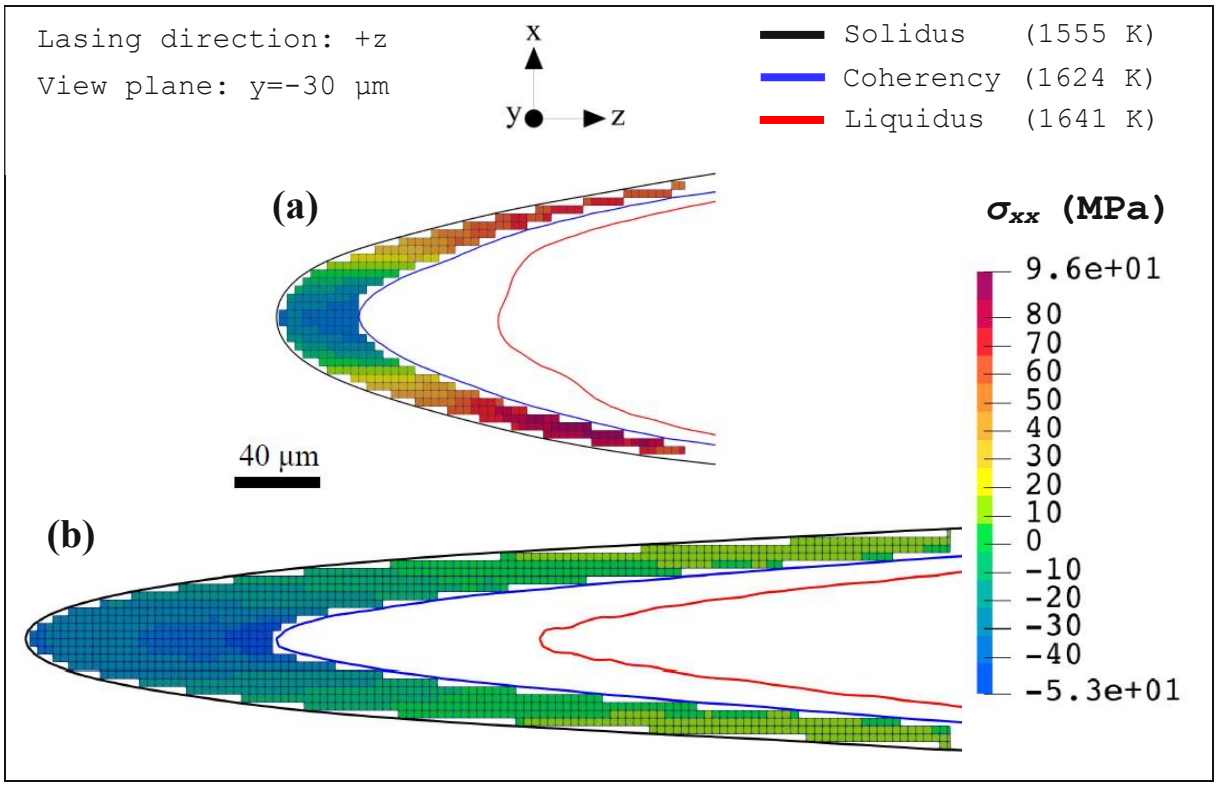

Fig. 5.10: Upper view of stress fields in the mushy zone for the case (a) w/o preheating, and (b) w/ preheating at 500 °C.

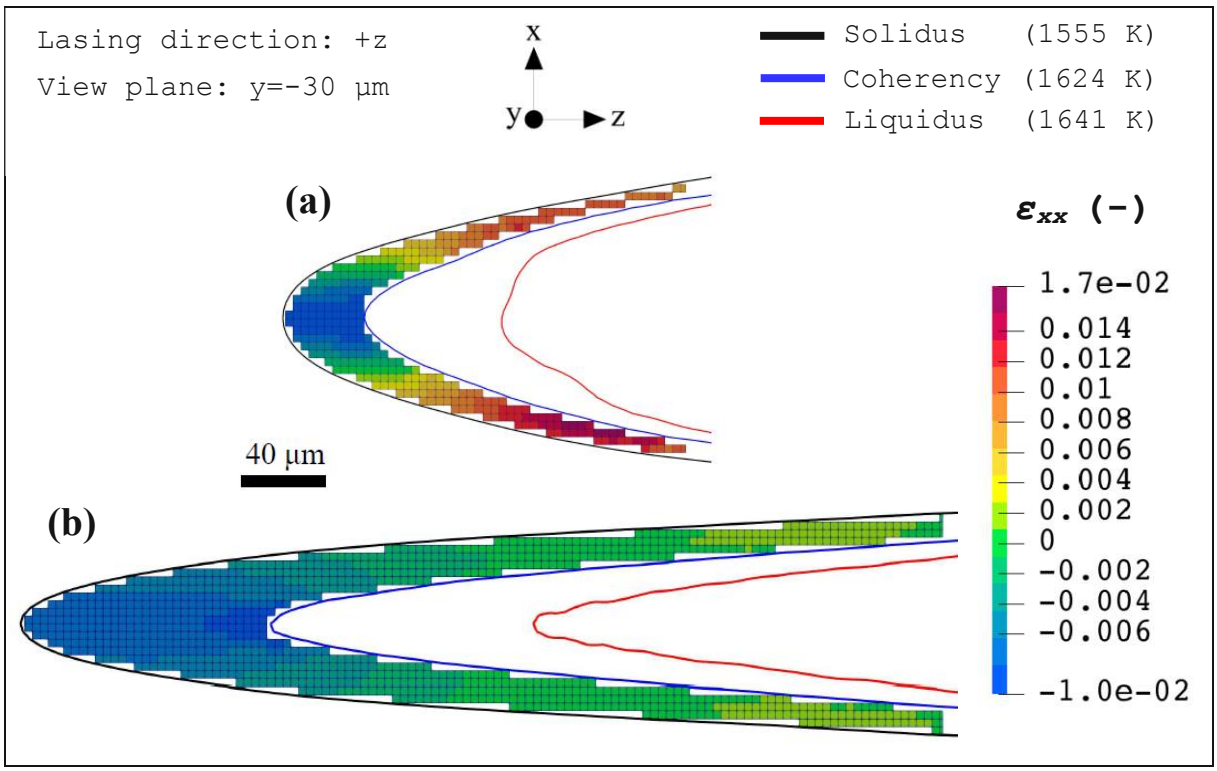

Fig. 5.11: Upper view of strain fields in the mushy zone for the case (a) w/o preheating, and (b) w/ preheating at 500 °C.

5.4 Solidification Cracking

5.4.1 Rate of Feeding (ROF)

Fig. 5.12 displays the Rate of Feeding (ROF) as it evolves over time along a fixed line inside the mush. The curves obtained are not necessarily smooth, alternating between positive and negative values depending on time and location. A positive ROF value indicates a net flow of liquid volume into a control volume, while a negative value represents a net flow out of the control volume. A certain degree of symmetry can be distinguished with respect to the longitudinal midplane $x = 0\ \mu m$; see for example the curves corresponding to times t_1 and t_3, which are only 0.026 ms apart from each other.

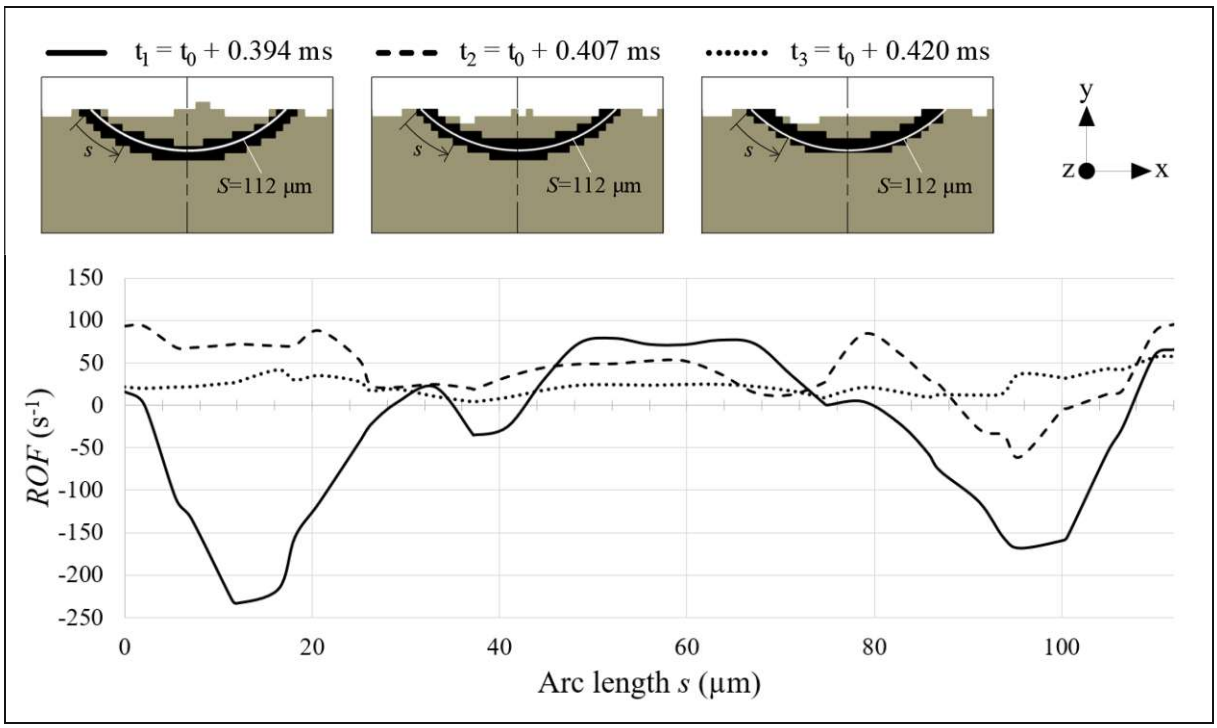

Fig. 5.12: Evolution over time of ROF along a fixed line for the case w/o preheating.

The ROF depends on liquid motion. Looking at Fig. 5.13, the velocity field of the liquid phase appears symmetrical from a general perspective, but there is some local disorder near the mush. In some regions, the direction of the velocity vectors, $f_l \boldsymbol{u}$, does not change smoothly when walking along the coherency isothermal line; in fact, there are quick orientation changes. Due to this, perfect symmetry and smoothness cannot be expected for the rate of liquid feeding. In other regions, there are vectors pointing away from the mush (backflow into the melt pool), suggesting liquid loss rather than feeding. Thus, depending on time and location, there may be negative ROF values. The latter is also illustrated in Fig. 5.14, which presents the ROF distribution over two isothermal surfaces within the mushy zone, namely 1624 K and 1585 K.

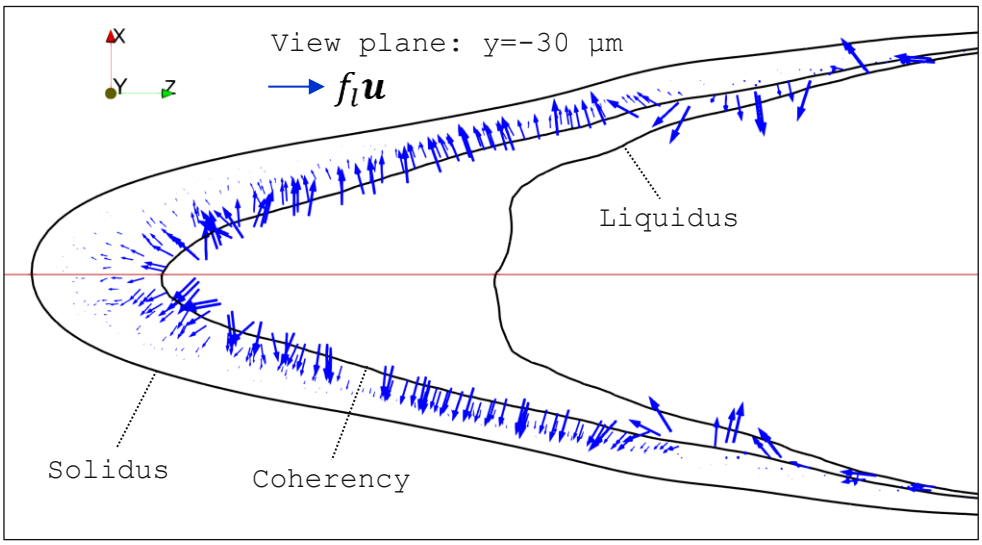

Fig. 5.13: Liquid velocity towards the mush (no preheating).

For a given isothermal surface, where the liquid fraction is the same at all points, the ROF is not constant because, as defined in this study, it depends not only on the liquid fraction, f_l, but also on the divergence of the velocity field $\boldsymbol{u}$.

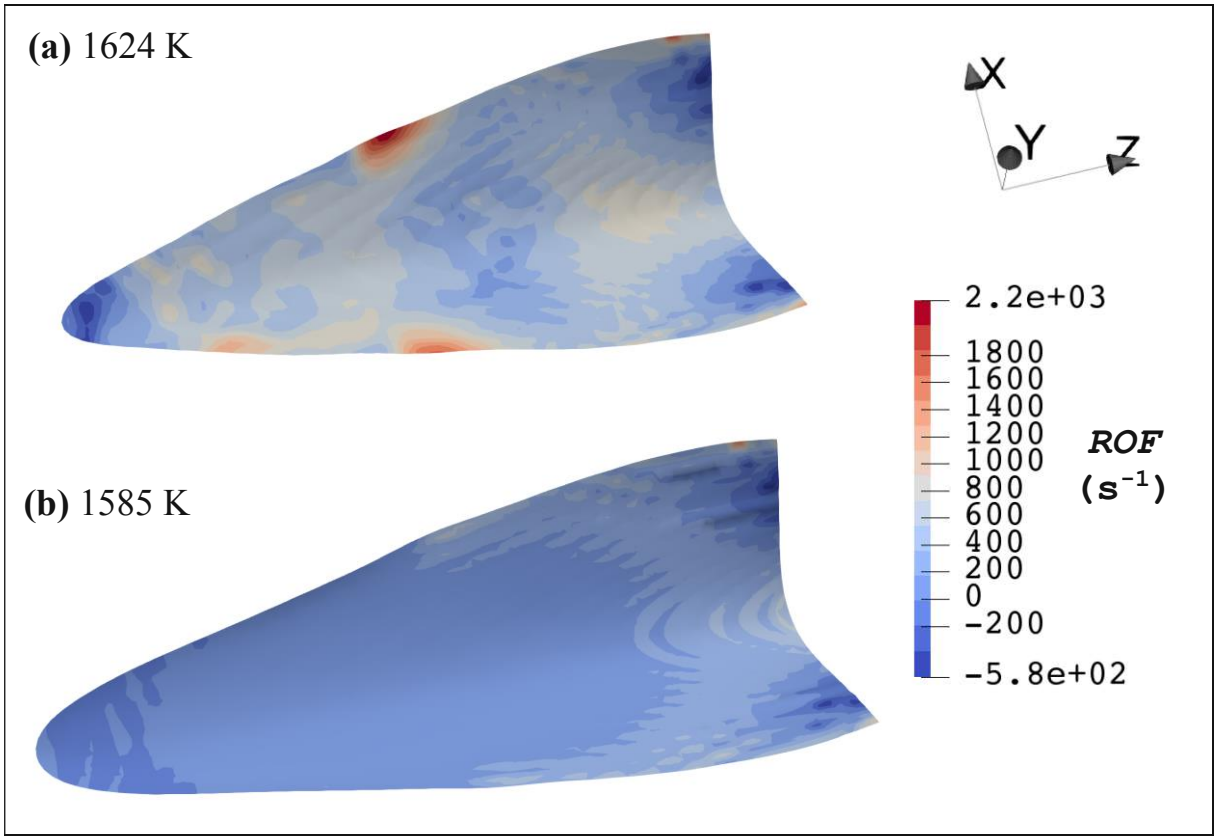

Fig. 5.14: Color map of ROF for two isothermal surfaces within the mushy zone: (a) 1624 K, and (b) 1585 K.

It is interesting to compare the order of magnitude of the ROF values shown in Fig. 2.4 (see chapter 2) with those in Fig. 5.14. In the first situation, which applies to the casting process of an Al-Si alloy, the ROF varies from an order of magnitude of approximately 10^{-1} to 10^{-3} s^{-1} upon solidification, while in PBF-LB of CM247LC nickel alloy, the ROF reaches up to 10^{3} s^{-1}, that is, feeding rates that are thousands of times higher than those estimated for the casting process. Another important observation from the results applicable to casting is that the ROF and the ROS are usually reported as a function of temperature (or liquid/solid fraction) only. In other words, a single feeding or shrinkage rate is associated with a specific temperature during solidification. This could be valid for cases where the fluid velocity is not as influential as in PBF-LB. In the latter, due to the effect of fluid velocity, a distribution of rates is related to each temperature.

As can also be seen in Fig. 5.14, ROF values are generally lower at lower temperatures. To provide a better numerical perspective, Table 5.1 shows the quartiles of the ROF distribution for different isothermal surfaces. Then, the effect of preheating is illustrated through plots of the median and the minimum values, as shown in Figs. 5.15 and 5.16, respectively.

Table 5.1: Quartiles of the ROF distribution for different isothermal surfaces [a]

Case	Isotherm (K)	Min.	Q1	Q2	Q3	Max.
No preheating	1624	-412,67	470,85	567,78	706,50	2490,30
	1610	-411,55	301,84	421,04	516,38	2634,50
	1590	-409,95	78,07	151,91	284,82	2750,70
	1570	-386,46	11,64	31,92	117,07	2737,50
	1555	-380,38	1,61	6,30	45,48	2727,60
Preheating at 500 °C	1624	-1193,90	171,60	254,29	324,01	2060,60
	1610	-598,19	71,57	113,52	158,60	1420,00
	1590	-454,53	9,25	16,33	29,03	580,08
	1570	-271,24	0,67	1,33	2,91	277,13
	1555	-141,22	0,04	0,10	0,30	120,92
Preheating at 1000 °C	1624	-42,53	22,01	28,93	36,83	55,62
	1610	-37,58	5,64	7,22	8,74	49,55
	1590	-18,18	0,53	0,69	0,92	18,23
	1570	-6,11	0,01	0,03	0,07	11,90
	1555	-1,16	0,00	0,00	0,00	1,62

[a] ROF values in s^{-1}.

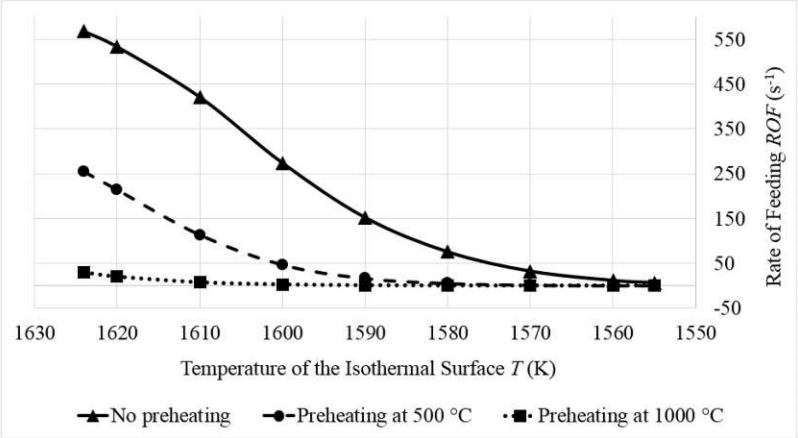

Fig. 5.15: Median (Q2) of ROF for different isothermal surfaces.

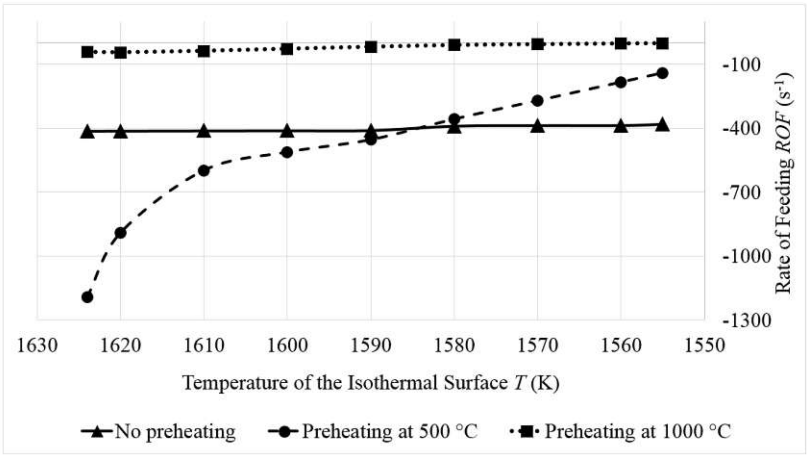

Fig. 5.16: Minimum value of ROF for different isothermal surfaces.

Two main effects of preheating on the ROF are identified. On the one hand, the higher the preheating temperature, the lower the rate of positive feed. This trend is observed not only for the median (Q2) but also for Q1, Q3, and the maximum values (see Table 5.1). The explanation for the latter lies in the fact that, at higher preheating temperatures, the temperature gradients between the melt pool and the substrate become lower, which constrains the convective flow towards the mush. Certainly, this effect seems to play against the mitigation of hot cracking. On the other hand, higher preheating temperatures contribute to reducing the net volumetric flow out of the mush. In Fig. 5.16, this is evident for a preheating temperature of 1000 °C during the entire solidification process, as well as for a preheating temperature of 500 °C during the last stage of solidification. This second effect would be in favor of hot cracking mitigation, since it suggests that more liquid is kept within the mush at higher preheating temperatures. The question then arises as to what is more decisive for solidification cracking: a) to have a high rate of liquid feeding, or b) to sustain liquid feeding into the mush, even if it is at a relatively low rate, while preventing backflows towards the melt pool as much as possible.

5.4.2 Rate of Shrinkage (ROS)

The evolution of the Rate of Shrinkage (ROS) is examined along a fixed line for two scenarios, inside and outside the mush, as represented in Figs. 5.17 and 5.18, respectively. The latter shows that, for a stationary observer, the shrinking rate decreases within the substrate over time.

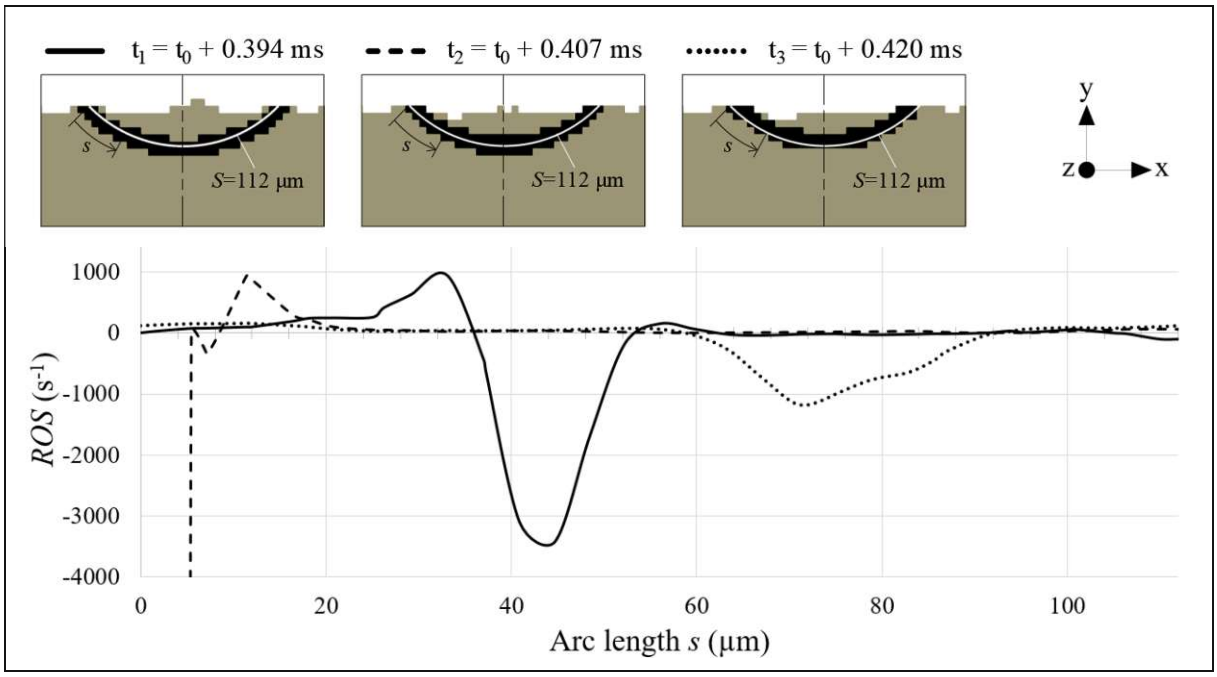

Fig. 5.17: ROS evolution along a fixed line while inside the mush (case w/o preheating).

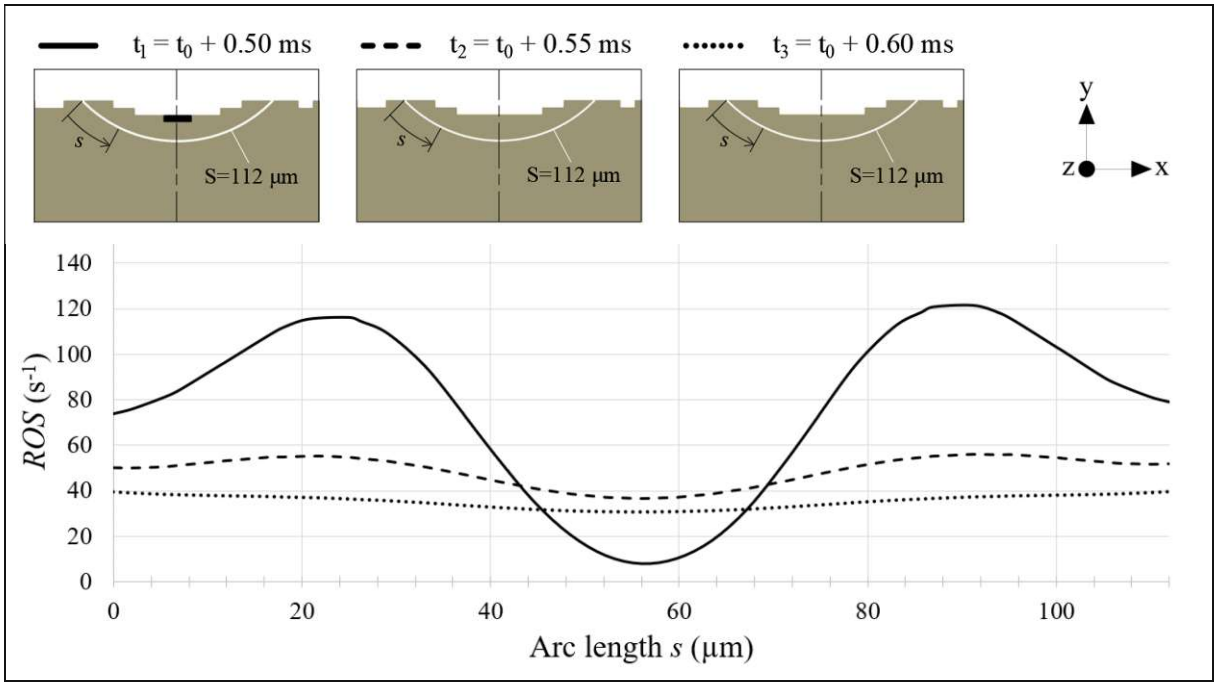

Fig. 5.18: ROS evolution along a fixed line while outside the mush (case w/o preheating).

Inside the mush, large peaks and strong oscillations between positive and negative ROS values are observed, whereas the substrate (mainly solid phase) displays smooth and symmetrical curves. This result is also illustrated in Figs. 5.19 and 5.20, showing ROS color maps at a transverse cross section and at two isothermal surfaces within the mush, respectively.

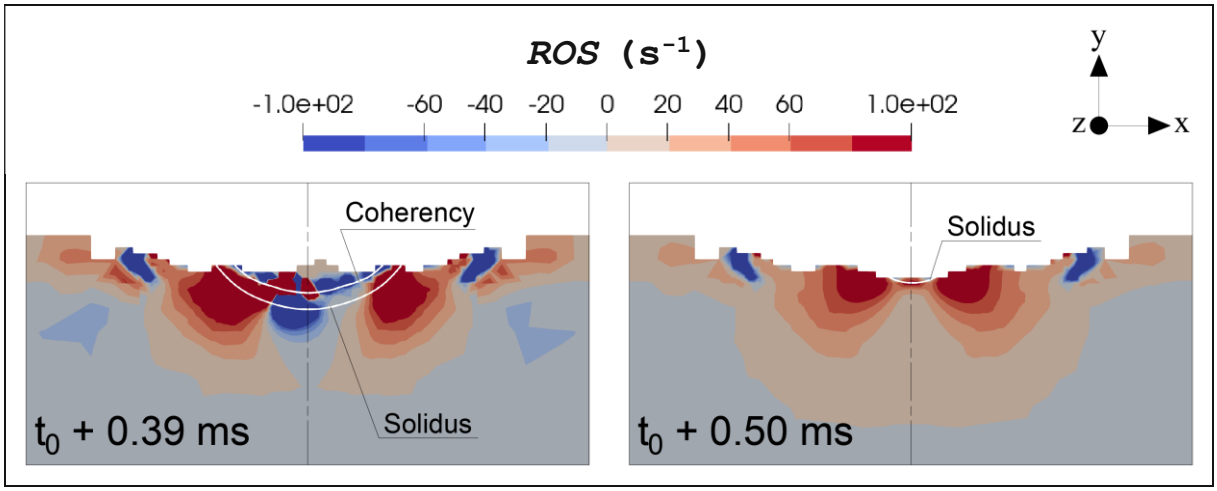

Fig. 5.19: Cross-section view of the ROS outside and inside the mush.

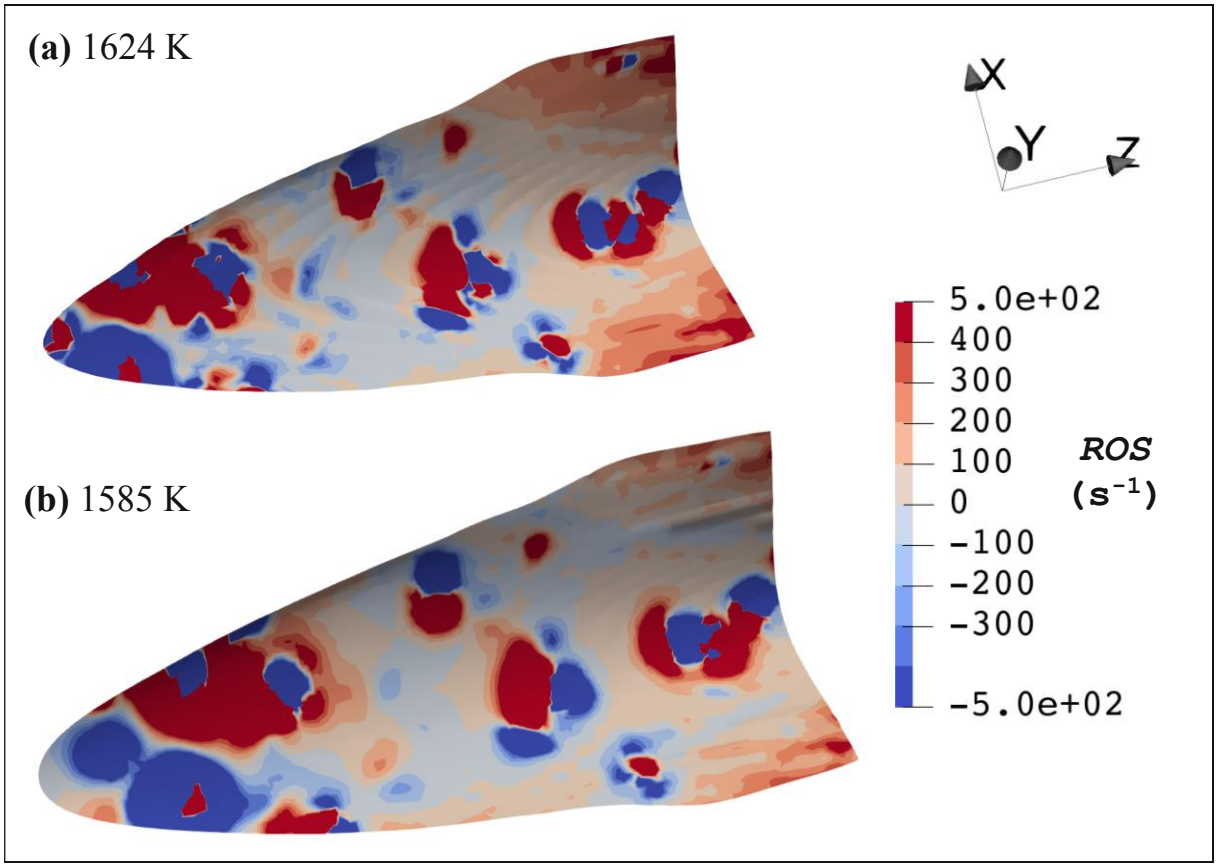

Fig. 5.20: Color map of ROS for two isothermal surfaces within the mushy zone: (a) 1624 K, and (b) 1585 K.

According to Fig. 5.19, the largest ROS values are found towards the left and right sides of the mush. Already in the slurry, i.e., above the coherency temperature, very high positive and negative ROS values are observed. The contradictory aspect of the latter is that mechanical strains within the slurry and the liquid phase must be zero, and therefore the ROS as well, since this parameter is estimated from the trace of the strain rate tensor. This is something to review in the current implementation of the thermomechanical model. Given that the displacements within the liquid phase are considerably larger than those within the solid phase, not filtering them out completely from the calculation of mechanical strains could lead to strong ROS peaks in the mush.

With a little effort, some degree of symmetry can be identified in the isothermal surfaces of Fig. 5.20, which is consistent with the behavior observed in the substrate. However, this symmetry is distorted by the ROS peaks (blue and red stains). To obtain more information from the available data, again the quartiles of the ROS distribution for different isothermal surfaces were collected and summarized in Table 5.2. Given the large difference between the minimum values and the lower quartiles (Q1), and between the maximum values and the upper quartiles (Q3), the positive and negative ROS peaks most likely include outliers.

Table 5.2: Quartiles of the ROS distribution for different isothermal surfaces [a]

Case	Isotherm (K)	Min.	Q1	Q2	Q3	Max.
No preheating	1624	-2,4E+06	-46,37	56,03	219,81	3,8E+05
	1610	-2,0E+06	-42,95	51,73	189,09	2,0E+05
	1590	-1,5E+06	-50,88	38,80	142,27	4,4E+04
	1570	-1,1E+05	-53,51	30,56	124,54	2,5E+04
	1555	-1,2E+04	-51,75	27,26	111,92	1,6E+04
Preheating at 500 °C	1624	-3,7E+05	-53,50	-10,91	33,58	6,5E+04
	1610	-3,1E+05	-38,33	6,86	55,48	3,2E+04
	1590	-3,8E+04	-33,11	11,95	55,96	1,8E+04
	1570	-5,6E+03	-25,23	12,31	46,09	8,6E+03
	1555	-3,5E+03	-16,85	11,82	37,23	2,6E+03
Preheating at 1000 °C	1624	-3,1E+05	-7,24	0,39	10,79	1,2E+05
	1610	-9,1E+04	-3,87	2,36	9,79	2,0E+04
	1590	-3,2E+04	-1,36	1,72	5,91	2,4E+04
	1570	-9,3E+04	0,00	1,54	3,45	7,4E+04
	1555	-3,9E+04	-0,01	1,06	2,01	2,1E+04

[a] ROS values in s^{-1}.

The median (Q2) is a good indicator of central tendency when dealing with skewed distributions or when there are outliers in the data. From the plots of the second quartiles, Fig. 5.21 shows that higher preheating temperatures considerably reduce the rate of shrinkage within the mush, which favors hot cracking mitigation. This trend applies for the upper quartiles as well, as seen in Table 5.2. When plotting the lower quartiles as in Fig. 5.22, it is worth noting that higher preheating temperatures also lead to lower expansion rates in the material. By viewing the mush as a continuum, the latter makes sense, since regions undergoing significant contraction must cause equivalent or compensatory expansion in adjacent areas. This explains why the red spots in Fig. 5.20 are accompanied by blue spots.

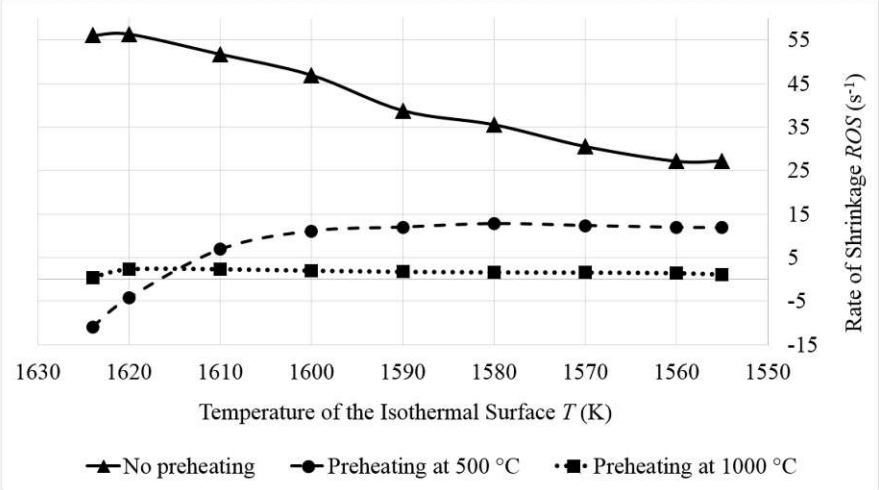

Fig. 5.21: Median (Q2) of ROS for different isothermal surfaces.

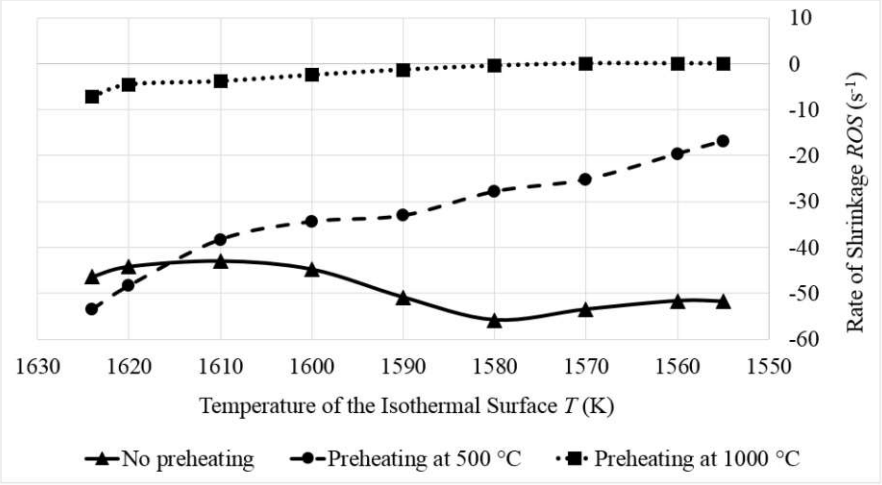

Fig. 5.22: First quartile (Q1) of ROS for different isothermal surfaces.

5.4.3 Solidification Cracking Evaluation

Despite the perturbations affecting the ROS in the mush, an interesting trend is recognized when considering the worst-case scenario, that is, shrinking cells (positive ROS) for which the net volumetric flow of liquid is outwards (negative ROF). Fig. 5.23 shows the regions where the proposed hot cracking criterion is met considering the aforementioned conditions. In all cases, with and without preheating, most of the susceptible volume elements are found in the lateral and rear regions of the mush.

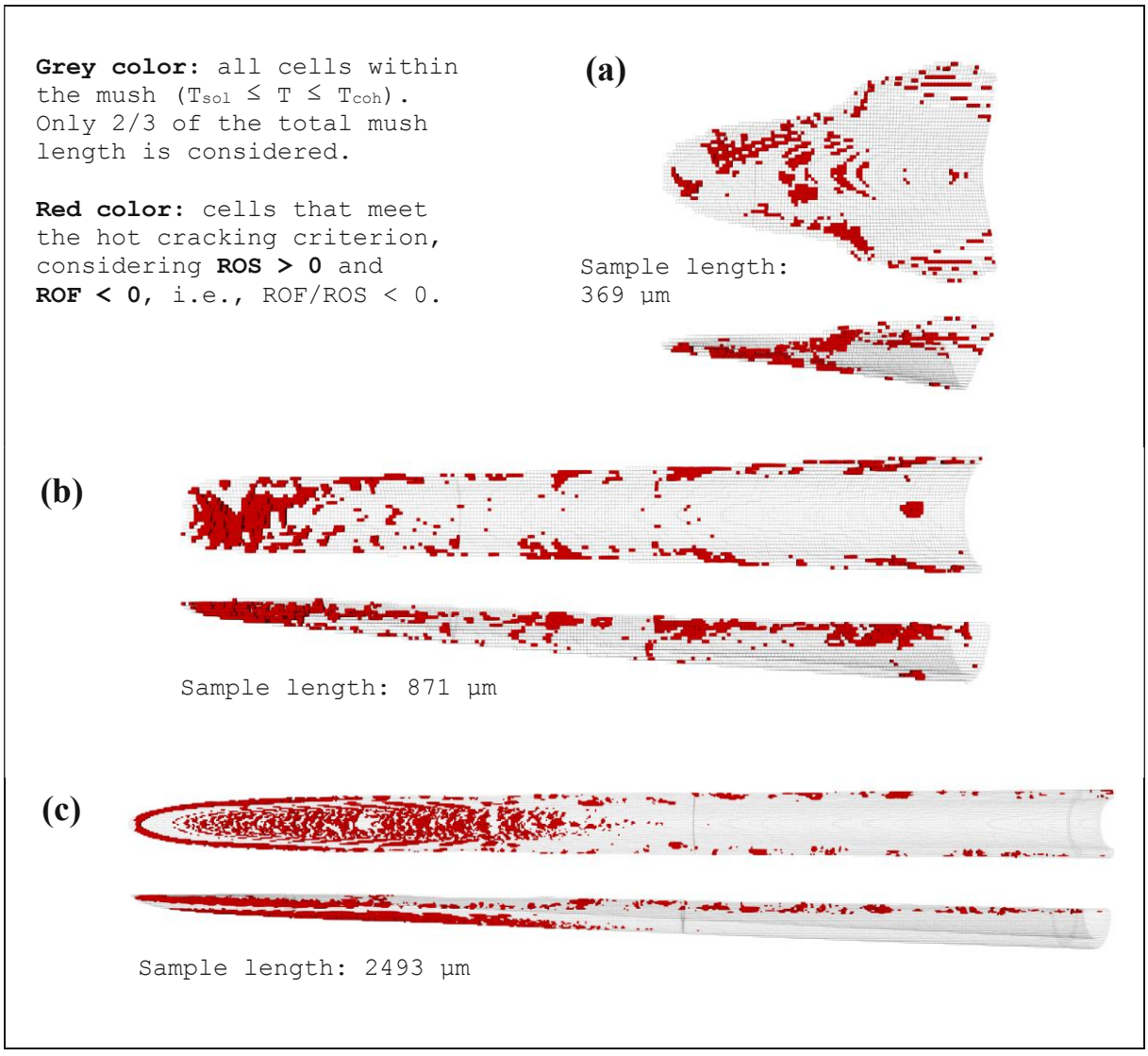

Fig. 5.23: Top and side views of the regions susceptible to cracking for cases (a) w/o preheating, (b) w/ preheating at 500 °C, and (c) w/ preheating at 1000 °C.

The HCS is estimated using Eq. (3.19) based on data collected at different time steps after the melt pool and mushy zone reached a nearly constant shape. When evaluated in this way, Fig. 5.24 not only shows that higher preheating temperatures lead to a lower risk of cracking but also to a decrease in the dispersion of the HCS index, i.e., the ratio of susceptible cells to sample size becomes less variable between time steps.

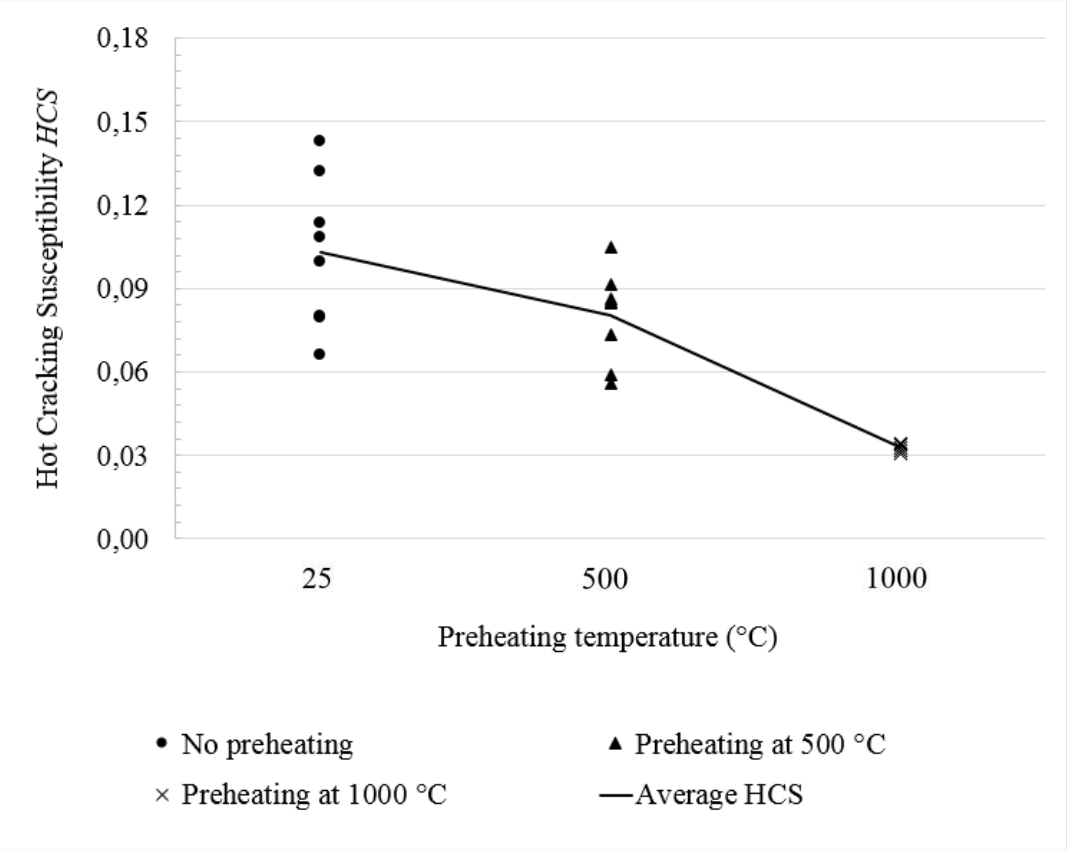

Fig. 5.24: Effect of preheating temperature on hot cracking susceptibility.

6 Discussion

Additional aspects of the simulations are discussed in this chapter, including a qualitative verification of the temperature field for the case without preheating, the validity of linear thermoelasticity as constitutive law, the perturbations affecting strain and ROS fields within the mush and, finally, a brief comparison between Feurer's original approach and the one used in this study for the evaluation of solidification cracking.

6.1 Verification of the Temperature Field

Fig. 6.1 compares the cross-section temperature fields from [37] and this work for PBF-LB single-track simulations of CM247LC. The images show the temperature fields from the substrate's top surface downwards. Both studies considered the process parameters and material data listed in Tables 4.2 and 4.5, as well as very similar temperature-dependent thermophysical properties. In [37], the temperature field was recorded at the "start of solidification", which for comparison purposes is assumed here to be the time when the depression at the front of the melt pool reaches maximum depth. The objective in [37] was to simulate the microstructure growth of a single track using a two-dimensional cellular automata (CA) model that included non-equilibrium rapid solidification. The input temperature field for the CA-based approach was computed by a three-dimensional numerical SLM melt pool simulation model that combined the Finite Difference Method (FDM) and Volume of Fluid Method (VOF), considering physical effects such as conduction, convection, radiation, buoyancy, capillary forces, Marangoni effect, evaporation, and recoil effects.

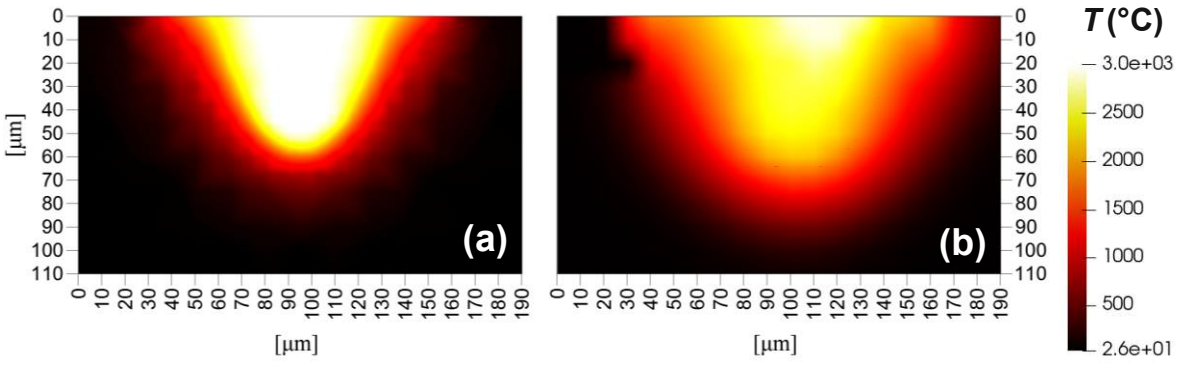

Fig. 6.1: Comparison between temperature fields from (a) this study and (b) [37].

Between the two temperature fields shown, there is good similarity in penetration depth and melt pool width, although Fig. 6.1(a) exhibits additional evaporation (larger white region) and a more symmetrical temperature distribution. Aside from the discretization methods employed

in each study, the differences in melt pool dimensions and temperature distribution could be attributed to the differing radiation absorption models, which greatly influence the way in which input energy is spread within the material and, therefore, the dimensions and dynamics of the melt pool. In the present study, beam absorption and reflection is modeled by the Fresnel equations, considering the complex refractive indices of each phase, while the absorption of laser radiation in [37] was based on the model proposed by Gusarov et al. [59]. The latter was specifically constructed to investigate single-track scanning of a laser beam over a thin layer of metallic powder placed on a dense substrate of the same material, estimating an effective volumetric heat source from laser radiation scattering and absorption in the powder layer.

6.2 Validity of Linear Thermoelasticity

Fig. 5.10(a) illustrates that, although a relatively low modulus of elasticity was considered at solidus temperature (5 GPa according to Table 4.6), the assumed yield strength of 50 MPa is already exceeded in the lateral regions of the mush for the case without preheating. Fig. 5.10(b) depicts a different situation for the case with preheating at 500 °C, where the tensile stresses obtained do not exceed the fluency limit, suggesting that the assumption of linear thermoelasticity could be consistent under these circumstances. As seen in Fig. 5.11, strains in the semisolid are considerably smaller when applying enough preheating, favoring linear thermoelasticity (law for small deformations) as a valid constitutive law in the mushy zone.

Given the very high temperatures involved in the solidification process of the selected nickel alloy, the very small spatial extent of the mushy zone, and the celerity of the solidification process, it seems challenging to design a reliable experimental procedure that allows the validation of the constitutive law governing the stress-strain relationship in this region.

The lack of reliable material properties also represents a common limitation in computational simulation problems. The local physical conditions generated during PBF-LB/M are probably beyond the capabilities of experimental setups and measuring systems that would be necessary to derive material properties in a process-like environment. Moreover, the thermophysical properties depend not only on the composition of the alloy, but also on the temperature, whether the material undergoes cooling or heating, as well as the cooling or heating rates. Likewise, the mechanical properties are influenced by temperature, evolution of the microstructure (grain size, growth orientation, morphology), strain rate, among others. In this work, “reasonable” assumptions had to be made to perform simulations that contribute to gaining insights into the development of stress and strain in the mushy zone.

In solid regions outside to the mushy zone that have been affected by heat, or after solidification has been completed, it is not appropriate to speak of linearity in the stress-strain relationship, as demonstrated in Fig. 6.2, showing a color map of the stress component σ_{xx} in the cross-section of a fully solidified bead when no preheating is applied. After quickly comparing this

figure with the yield stress values in Table 4.6, it can be seen that fluency is readily exceeded at different temperatures below solidus. For example, according to Table 4.6, the fluency limit at 1088 K is 693 MPa, but Fig. 6.2 shows compressive stress values of the order of 10^3 MPa when following the corresponding isothermal line. Similarly, for a temperature of 1240 K, the fluency limit should be between 50 MPa and 693 MPa. However, Fig. 6.2 shows tensile stress values of the order of 10^3 MPa, especially towards the lateral sides of the bead. As illustrated in Fig. 4.10, the elastic modulus increases steadily with decreasing temperature, requiring the integration of a plasticity model to adequately simulate the thermomechanical behavior of the material outside the mushy zone.

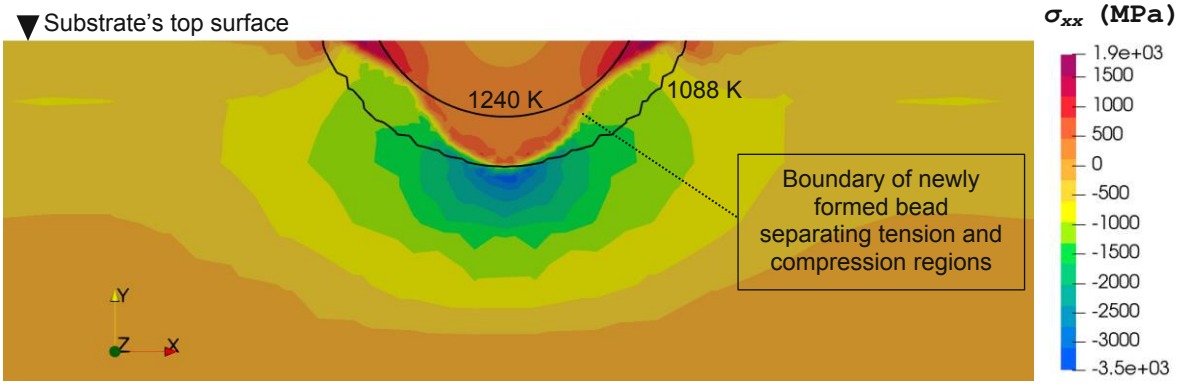

Fig. 6.2: Stress field outside the mushy zone.

6.3 Perturbations in Strain and ROS Fields

Currently, the thermomechanical solver also produces non-zero strain values for non-solid phases, contradicting the idea that mechanical strain begins to accumulate when the solid fraction within a volume element reaches 60%, the point at which coherency is assumed. Fig. 6.3(a) illustrates the latter considering ε_{yy} as an example. Two images are presented for the same cross-section and time, with the only difference being that the image underneath shades in dark color the non-solid or unconsolidated solid regions that exhibit the presence of mechanical strains. These strains are large compared to those in the mush or substrate, which appear as approximately zero on the color scale employed. As observed, there are non-zero strains in the powder and liquid phases, as well as in the slurry, which is considered a liquid with suspended solid particles. Both liquid and powder were assigned the same bulk modulus of 2 GPa in the simulations. As no information is available on the bulk modulus of liquid CM247LC, the value of liquid water was chosen as reported by [60]. The latter is comparable to the bulk modulus used for the solid phase at the solidus temperature, 3.5 GPa.

Considering the entire computational domain as a continuum, large displacements (or deformations or strains) in regions adjacent to the mush can lead to perturbations in the

calculated strains within this region (see, for example, Figs. 5.7 and 5.9), generating strong variations in the rate of shrinkage, ROS, as shown in Fig. 5.17. Perturbations in the ROS can be magnified since this parameter takes into account the evolution of strain over time. The strains themselves should be smooth in the mush, so there is a greater chance that the ROS will be smooth. Fig. 6.3(b) reveals the presence of very high ROS values in the powder, slurry and adjacent regions, which is not expected to happen. In this case, the color scale was kept within $\pm 500\ s^{-1}$ for better visualization.

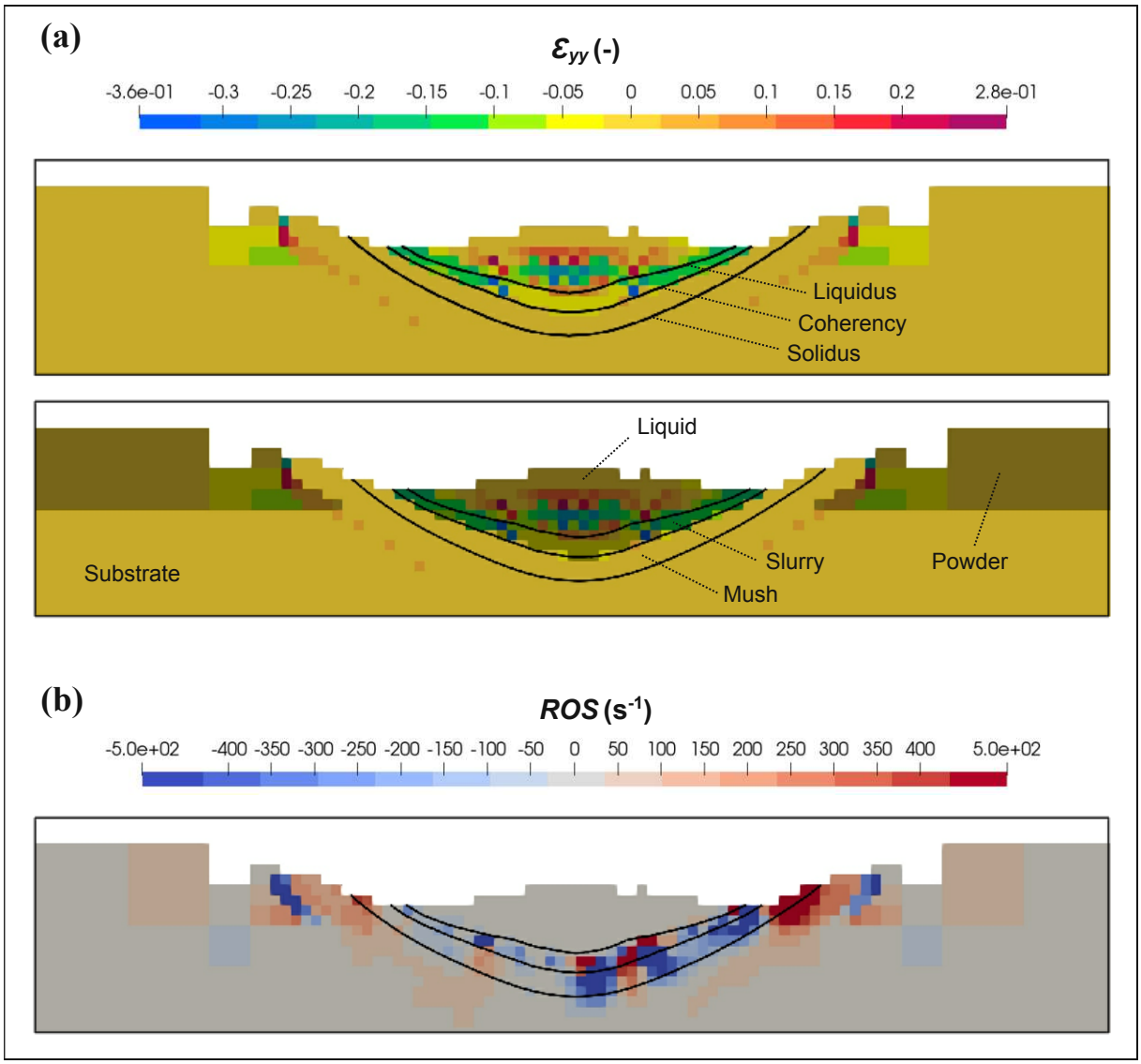

Fig. 6.3: Cross-section view of perturbations in (a) strain and (b) ROS fields.

How to minimize or eliminate the perturbations? The answer may not be straightforward. Having a finite bulk modulus for the liquid phase, one possible solution would be to define a temperature-dependent Poisson's ratio that approximates a value of 1/2 for temperatures equal or higher than liquidus. The latter would imply perfect incompressibility for the liquid phase,

and the shear and elasticity moduli, G and E respectively, would both become zero (see Eqs. 3.8 and 3.9). In addition, the first Lamé constant, λ, would be equal to the bulk modulus, K, and the displacement equation for non-solid volume elements would read as follows:

$$\rho \frac{\mathrm{d}^2}{\mathrm{d}t^2} \boldsymbol{D} = \nabla \cdot (\lambda \operatorname{tr} \nabla \boldsymbol{D}\, \boldsymbol{I}) = \nabla \cdot (K \operatorname{tr} \nabla \boldsymbol{D}\, \boldsymbol{I}) \tag{6.1}$$

This approach needs to be tested for stability. It is expected that metal vapor or the surrounding gas, which are compressible, will not adversely affect the solid-displacement solution using the above approach, since they have a quite low bulk modulus when compared to the liquid, powder, or solid phases.

Such idealization could also be applied to the powder phase, which is treated here as a liquid with powder-like properties. However, in that case, the Poisson's ratio should remain at 1/2 (or approximately 1/2) at all temperatures.

6.4 Differences between Feurer's Approach and this Work

In the traditional way of applying Feurer's theory, it is common practice to associate a single rate of feeding or shrinkage with a specific temperature or phase fraction. There, the susceptibility to hot cracking is given by the temperature at which ROF equals ROS. The lower this critical temperature, the less prone the material is to crack. In the present approach, due to the dependence of the ROF on liquid velocity, all isothermal surfaces within the mush may contain regions where the Feurer condition is met. Thus, it cannot simply be said here that reaching a given temperature or liquid fraction determines whether or not solidification cracking is possible. In fact, looking at the ROF and ROS curves in Fig. 6.4, which are based on the median values for different isothermal surfaces, the conventional way of estimating cracking susceptibility following Feurer would predict a higher risk (intercept point located at higher temperatures) with increasing preheating temperature. The latter is contrary to experimental observations, since more preheating usually favors the mitigation of this defect. For that reason, the susceptibility to cracking susceptibility (HCS) is measured differently in this work, examining local conditions, volume element by volume element within the mush. Table 6.1 summarizes the main differences between Feurer's original approach and the present work.

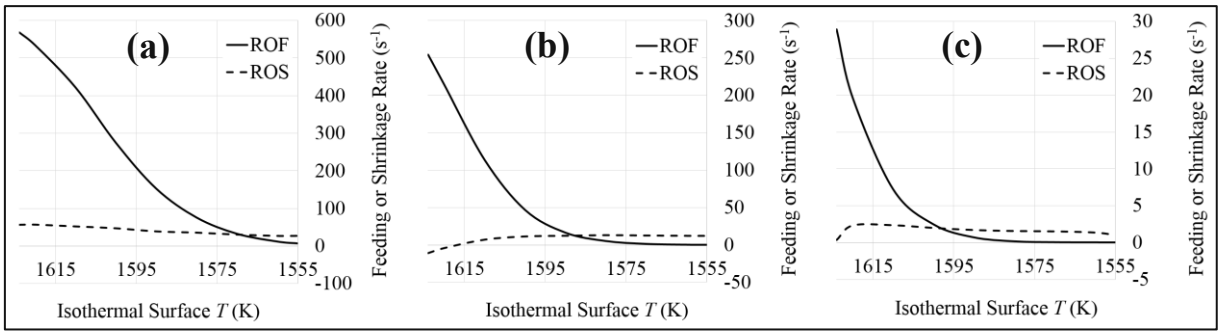

Fig. 6.4: Comparison between ROF and ROS based on the median values for cases (a) w/o preheating, (b) w/ preheating at 500 °C, and (c) w/ preheating at 1000 °C.

Table 6.1: Differences between Feurer's original approach and the current approach

Aspect	Feurer's approach	This work
Classification	Non-mechanical	Involves fluid and solid mechanics
Application	Casting	PBF-LB/M, laser welding
Solidification front morphology	Assumes dendritic growth	General model; does not differentiate between growth types.
ROF estimation	$\frac{{f_l}^2 {\lambda_2}^2 p_s}{24\pi c^3 \mu L^2}$	$-f_l \operatorname{div} \boldsymbol{u}$
ROS estimation	$-\frac{1}{\bar{\rho}} \frac{\partial \bar{\rho}}{\partial t}$	$-\operatorname{tr} \dot{\boldsymbol{\varepsilon}}$
Critical temperature	T_{cr} (temperature at which $ROF = ROS$)	Does not apply. The criterion can be met at various temperatures.
Cracking susceptibility index HCS	T_{cr}, $f_l(T_{cr})$, or $f_s(T_{cr})$	$\frac{\sum_{i=1}^{n} V_i}{\sum_{j=1}^{N} V_j}$

7 Conclusions and Future Work

This study has provided some important insights into different aspects of PBF-LB/M single-track simulations, including stress and strain development within the mushy zone, evaluation of solidification cracking, and the capabilities of the solver employed in OpenFOAM. The results obtained can serve as a contribution for the development of complementary research topics related to laser-assisted manufacturing technologies. Described below are the main outcomes of this work, together with the proposed future activities.

7.1 Process Features

Single-track simulations of laser sintered CM247LC nickel superalloy were performed. With the process parameters employed, and in the absence of preheating, the mushy zone exhibits dimensions of approximately 554 · 162 · 64 µm (length · width · depth) and a maximum cooling rate in the order of 10^6 K/s. Sustained evaporation is present at the melt pool's front, producing a keyhole-like depression with enhanced total absorbed power when compared to pure conduction regimes. After the depression reaches maximum depth, a given cross-section perpendicular to the laser path requires about 0.5 ms to fully solidify.

Unlike cooling rates, the spatial extent of the melt pool and mushy zone, the depth/width aspect ratio, and the cross-sectional solidification time increase when preheating is applied. Different preheating temperatures produce different bead morphologies, which should be taken into account in multi-track or multi-layer cases, since the substrate temperature changes permanently during processing.

Alloy solidification was modeled assuming thermodynamic equilibrium conditions. However, extremely high cooling rates, such as those obtained in the present PBF-LB/M simulations, have been shown to promote non-equilibrium solidification, which can extend the freezing range and thus modify the geometry of the mushy zone.

Future work

- Implementation of a physical model that accounts for non-equilibrium solidification of metallic alloys, e.g., a Scheil-Gulliver solidification model. This will help determine how non-equilibrium solidification affects the geometry of the mushy zone, the development of stresses and strains, and the evaluation of solidification cracking.
- Parametric analyzes involving different process variables, such as input power, beam geometry, powder bed thickness, etc., should be carried out to investigate their impact on bead morphology, as the latter can become a source of defects when not adequately

controlled. It would also be interesting to evaluate the influence of surface energy between the different phases on bead morphology.

7.2 Stress and Strain

Here, it has been shown that mechanical stress and strain fields can be modeled within the mushy zone, using the Finite Volume Method (FVM) as a numerical technique capable of combining fluid mechanics phenomena with solid mechanics, as well as other physical effects. As a first approximation to the solution, equilibrium solidification was assumed to estimate the temperature field, while linear thermo-elasticity was selected as the constitutive law for the stress-strain relationship, employing a sequentially coupled thermal-stress analysis, of course in combination with temperature- and phase-dependent material properties.

From the simulations carried out, the stress and strain fields appear symmetrical with respect to the median plane $x = 0\,\mu m$. The transverse stress and strain components, σ_{xx} and ε_{xx}, respectively, show the highest values in both tension and compression states. When analyzing solidification on a cross-section perpendicular to the beam travel, the behavior is mainly tensile towards the left and right ends of the mush, while it is compressive towards the central part. The evolution of stresses and strains is perceived differently depending on the point of view. From a Lagrangian perspective, when following the mushy zone as it moves up the cross-section, the magnitude of stresses and strains decreases within the mush. By contrast, when viewed from a fixed line on the cross-section (Eulerian description), stresses increase as temperature decreases, whereas strains tend to lower values. A higher preheating temperature results in lower tensile stresses and strains in the lateral regions of the mush. The influence of preheating on compression stresses and deformations was not found to be as significant.

Considering the complexity of PBF-LB/M and the multiple phases involved, few studies actually model stress and strain during solidification, adding value to the present work. Several approaches focus on thermomechanics outside the mushy zone, where the material is completely solid.

Linear thermo-elasticity may be valid inside the mushy zone (it is hard to prove otherwise), but it is definitely not applicable in adjacent solid regions, where it is necessary to incorporate plasticity effects for proper thermomechanical modeling.

Future work

- Review of the current thermomechanical implementation in order to cancel the perturbations produced on mechanical strains in the mush. This will reduce the spikes or outliers obtained in the Rate of Shrinkage (ROS), which depends on the trace of the strain rate tensor, and perhaps contribute to increasing the robustness of the solver when computing solid stresses and strains.

- To incorporate plasticity for an adequate estimation of stresses and strains outside the mushy zone. This enhanced thermomechanical model could also be tested within the mushy zone to contrast the results obtained using the linear thermo-elastic assumption. Plasticity is necessary to estimate permanent deformations and residual stresses within the workpiece.
- Estimation of the coherency temperature using grain growth models.
- To investigate the influence of different sets of mechanical boundary conditions on stress and strain fields. In the simulations, the geometry used is assumed to be a small portion of a larger substrate. In this sense, how well does the fixed displacement boundary condition fit this assumption? To investigate this question, simulations can be conducted using a larger substrate with volume elements of appropriate size, and a free-face-type boundary condition (zero force or zero second time derivative for displacement) on the side faces. This configuration is believed to be closer to a real experimental situation and will allow verifying through simulations how well stresses and strains match those obtained with the fixed displacement boundary condition (or other types of boundary conditions, e.g., *zeroGradient*) in a smaller region of interest.
- To model stresses and strains using a different simulation software or numerical method, e.g., FEM, in order to assess the consistency of the numerical results obtained in OpenFOAM.
- It would also be interesting to implement the calculation of principal stresses and principal strains. These provide the magnitude and direction of maximum and minimum stresses and strains, allowing for the identification of possible cracking modes. Besides, there are hot cracking criteria such as the one proposed by Magnin et al. [15], which are based on principal strains.

7.3 Solidification Cracking

This study demonstrates the capability of the available multi-physical numerical model [9 - 12] to incorporate hot cracking analysis into simulations of laser-assisted manufacturing processes. On this occasion, a hot cracking criterion based on Feurer's shrinkage-feeding theory [20] was implemented and tested, combining thermofluid science with solid mechanics for a more integral evaluation. In addition, the effect of preheating temperature on hot cracking mitigation was examined using a susceptibility index based on the volume fraction of the elements that meet the proposed criterion.

Fundamental to Feurer's concept are two parameters: rate of volumetric liquid feeding (ROF) and rate of volumetric shrinkage (ROS). Solidification cracking is possible when the ROF is lower than the ROS. As implemented in this work, the simulation results show that the criterion

can be met at any isothermal surface within the mush, depending on the local conditions present in each volume element. When considering the least favorable situation, i.e., shrinking cells (positive ROS) for which the net volumetric flow of liquid is outwards (negative ROF), the majority of the susceptible elements are found in the lateral and rear regions of the mush. When evaluated in this way, the proposed HCS index indicates a lower susceptibility to hot cracking as the preheating temperature increases, which is in accordance with practical experience.

From a fluid mechanics point of view, a higher preheating temperature does not improve liquid feeding (it actually lowers the ROF), but prevents excessive backflow from the mush into the melt pool (less negative ROF values). From a solid mechanics perspective, preheating significantly reduces the ROS, i.e., strain rates.

Future work

- To verify how the results related to solidification cracking are affected after reducing or eliminating the perturbations produced when calculating the ROS. In this way, other regions susceptible to hot cracking can be more reliably identified, including those where the ROF is positive.
- To investigate the influence of other parameters besides preheating on solidification cracking. For example, laser beam geometry, scanning speed, input power, powder bed thickness, etc. Another important variable to examine is the permeability of the mushy zone (κ in Eq. 3.5), since it can strongly influence the ROF.
- Validation of the proposed hot cracking evaluation methodology based on single-track experiments.
- Finally, to what extent is shrinkage due to mechanical deformations relevant? Would it be enough to simply model the ROS based on the average change in density, as originally proposed by Feurer? If this was the case, less computational effort would be required to assess solidification cracking, as the calculation of mechanical strains would not be necessary. To answer this question, the contribution of thermal strains, $\boldsymbol{\varepsilon}^{th}$, to the global strain tensor, $\boldsymbol{\varepsilon}$, should be assessed. This could be done by running similar simulations using Feurer's original ROS equation as shown in Table 6.1 and then comparing the results with those obtained from the thermomechanical model.

List of References

[1] I. Yadroitsev, I. Yadroitsava, A. Du Plessis, *Basics of laser powder bed fusion*, in: I. Yadroitsev, I. Yadroitsava, A. Du Plessis, E. MacDonald (Eds.), *Additive Manufacturing Materials and Technologies, Fundamentals of Laser Powder Bed Fusion of Metals*, Elsevier, 2021, pp. 15-38, https://doi.org/10.1016/B978-0-12-824090-8.00024-X.

[2] J.M. Ravalji, S.J. Raval, *Review of quality issues and mitigation strategies for metal powder bed fusion*, Rapid Prototyping Journal (2022), https://doi.org/10.1108/RPJ-01-2022-0008.

[3] S. Sanchez, P. Smith, Z. Xu, G. Gaspard, C.J. Hyde et al., *Powder Bed Fusion of nickel-based superalloys: A review*, International Journal of Machine Tools and Manufacture 165 (2021) 103729, https://doi.org/10.1016/j.ijmachtools.2021.103729.

[4] European Committee for Standardization. *Destructive tests on welds in metallic materials – Hot cracking tests for weldments – Arc welding processes – Part 1: General*. EN ISO 17641-1:2004.

[5] CUSTODIAN Consortium. *Deliverable D1.1 Handbook on metallurgical defects and their genesis*, Custodian Project (2019) 825103, H2020-ICT-2018-2020.

[6] J.H. Boswell, D. Clark, W. Li, M.M. Attallah, *Cracking during thermal post-processing of laser powder bed fabricated CM247LC Ni-superalloy*, Materials and Design 174 (2019) 107793, https://doi.org/10.1016/j.matdes.2019.107793.

[7] KM. Kim, U. Lee, H. Lee, SM. Seo, EJ. Chun, *Quantifying Susceptibility to Solidification Cracking in Oscillated CM247LC Superalloy Welds via Varestraint Testing*, Met. Mater. Int. (2022), https://doi.org/10.1007/s12540-022-01250-4.

[8] O. Adegoke, *Processability of Laser Powder Bed Fusion Alloy 247LC: Influence of process parameters on microstructure and defects*, Licentiate dissertation, University West (2020), available from: http://urn.kb.se/resolve?urn=urn:nbn:se:hv:diva-16114.

[9] H. Koch, R. Gómez Vázquez, A. Otto, *A Multiphysical Simulation Model for Laser Based Manufacturing*, Proceedings of the 6th European Congress on Computational Methods in Applied Sciences and Engineering – ECCOMAS (2012) 6709-6722.

[10] A. Otto, H. Koch, R. Gómez Vázquez, *Multiphysical Simulation of Laser Material Processing*, Physics Procedia 39 (2012) 843-852, https://doi.org/10.1016/j.phpro.2012.10.109.

[11] A. Otto, H. Koch, KH. Leitz, M. Schmidt, *Numerical Simulations – A Versatile Approach for Better Understanding Dynamics in Laser Material Processing*, Physics Procedia 12 A (2011) 11-20, https://doi.org/10.1016/j.phpro.2011.03.003.

[12] C. Zenz, M. Buttazzoni et al., *Simulation-based process optimization of laser-based powder bed fusion by means of beam shaping*, Additive Manufacturing (2023) 103793, https://doi.org/10.1016/j.addma.2023.103793.

[13] C.E. Cross, *On the Origin of Weld Solidification Cracking*, in: T. Böllinghaus, H. Herold (Eds.), *Hot Cracking Phenomena in Welds*, Springer, Berlin, Heidelberg, 2005, pp. 4-18, https://doi.org/10.1007/3-540-27460-X_1.

[14] J.C. Lippold, *Hot Cracking*, in: J.C. Lippold (Ed.), *Welding Metallurgy and Weldability*, John Wiley & Sons, Inc., Hoboken, New Jersey, 2015, pp. 84-129, https://doi.org/10.1002/9781118960332.ch3.

[15] D.G. Eskin, L. Suyitno, L. Katgerman, *Mechanical properties in the semi-solid state and hot tearing of aluminium alloys*, Progress in Materials Science 49 (2004) 629-711, https://doi.org/10.1016/S0079-6425(03)00037-9.

[16] N. Coniglio, C.E. Cross, *Initiation and growth mechanisms for weld solidification cracking*, International Materials Reviews 58 (2013) 375-397, https://doi.org/10.1179/1743280413Y.0000000020.

[17] D. Wang, S. Sakoda et al., *Investigation of Evaluation Method for Hot Cracking Susceptibility of 310S Stainless Steel during Laser Welding using Trans-Varestraint Test*, Quarterly Journal of the Japan Welding Society 33 (2015) 39-43, https://doi.org/10.2207/qjjws.33.39s.

[18] R. F. Pierer, *Formulation of a Hot Tearing Criterion for the Continuous Casting Process*, PhD dissertation, University of Leoben (2007), available from: https://pure.unileoben.ac.at/portal/files/2490560/AC06522242n01vt.pdf.

[19] D.J. Lahaie, M. Bouchard, *Physical modeling of the deformation mechanisms of semisolid bodies and a mechanical criterion for hot tearing*, Metall Mater Trans B 32 (2001) 697-705, https://doi.org/10.1007/s11663-001-0124-5.

[20] Suyitno, W.H. Kool, L. Katgerman, *Hot Tearing Criteria Evaluation for Direct-Chill Casting of an Al-4.5 Pct Cu Alloy*, Metall Mater Trans A 36 (2005) 1537-1546, https://doi.org/10.1007/s11661-005-0245-6.

[21] D. Manitsas, J. Anderson, *Hot Cracking Mechanisms in Welding Metallurgy: A Review of Theoretical Approaches*, MATEC Web Conf. 188 (2018) 03018, https://doi.org/10.1051/matecconf/201818803018.

[22] N. N. Prokhorov, N. Nikol. Prokhorov, *Fundamentals of the Theory for Technological Strength of Metals while Crystallizing During Welding*, Transaction of the Japan Welding Society 2 (1971) 109-117.

[23] M. Rappaz, J.M. Drezet, M. Gremaud, *A New Hot-Tearing Criterion*, Metall. Mater. Trans. A 30 (1999) 449-455, https://doi.org/10.1007/s11661-999-0334-z.

[24] M. Braccini, C. Martin, M. Suéry, Y. Bréchet, *Relation between mushy zone rheology and hot tearing phenomena in Al-Cu alloys*, in: P.R. Sahm et al. (Eds.), *Modeling of Casting, Welding and Advanced Solidification Processes IX*, Shaker Verlag, 2000, pp. 18-24.

[25] S. Kou, *A criterion for cracking during solidification*, Acta Materialia 88 (2015) 366-374, https://doi.org/10.1016/j.actamat.2015.01.034.

[26] J. Draxler, *Modeling and Simulation of Weld Hot Cracking*, PhD dissertation, Luleå University of Technology (2019), available from: http://urn.kb.se/resolve?urn=urn:nbn:se:ltu:diva-76425.

[27] A. Prabhu, *Influence of Phase Transformations on the Residual Stress Evolution and Cracking Tendency in CM247LC Nickel-base Superalloy*, PhD dissertation, University of Tennessee (2019), available from: https://trace.tennessee.edu/utk_graddiss/5746.

[28] J.N. Ghoussoub, Y.T. Tang, W.J.B. Dick-Cleland et al., *On the Influence of Alloy Composition on the Additive Manufacturability of Ni-Based Superalloys*, Metall. Mater. Trans. A 53 (2022) 962–983, https://doi.org/10.1007/s11661-021-06568-z.

[29] V.R. Voller, C. Prakash, *A fixed grid numerical modelling methodology for convection-diffusion mushy region phase-change problems*, Int. J. Heat Mass Transfer 30 (1987) 1709-1719, https://doi.org/10.1016/0017-9310(87)90317-6.

[30] Lf. Li, Rj. Zhang, Sj. Hu et al., *Prediction of mushy zone permeability of Al-4.5wt%Cu alloy during solidification by phase field model and CFD simulation*, China Foundry 16 (2019) 313-318, https://doi.org/10.1007/s41230-019-9039-0.

[31] M.H. Sadd, *Chapter 12 - Thermoelasticity*, in: M.H. Sadd (Ed.), *Elasticity (Fourth Edition)*, Academic Press, 2021, pp. 379-405, https://doi.org/10.1016/B978-0-12-815987-3.00012-8.

[32] Y. Vetyukov, *4 Elastizitätstheorie*, in: Y. Vetyujov (Ed.), *Mechanik 3*, TU Wien, 2020, pp. 13-27.

[33] W.M. Lai, D. Rubin, E. Krempl, *CHAPTER 3 – Kinematics of a Continuum*, in: W.M. Lai, D. Rubin, E. Krempl (Eds.), *Introduction to Continuum Mechanics (Fourth Edition)*, Butterworth-Heinemann, 2010, pp. 69-153, https://doi.org/10.1016/B978-0-7506-8560-3.00003-7.

[34] P. Zhang, C. Yi, G. Chen, H. Qin, C. Wang, *Constitutive Model Based on Dynamic Recrystallization Behavior during Thermal Deformation of a Nickel-Based Superalloy*, Metals 6 (2016) 161, https://doi.org/10.3390/met6070161.

[35] H. G. Weller, G. Tabor, H. Jasak, C. Fureby, *A tensorial approach to computational continuum mechanics using object-oriented techniques*, Computers in Physics and IEEE Computational Science & Engineering 12 (6) (1998) 620-631, https://doi.org/10.1063/1.168744.

[36] C.J. Greenshields, *OpenFOAM v6 User Guide*, OpenFOAM Foundation Ltd. (2018), https://doc.cfd.direct/openfoam/user-guide-v6/.

[37] M. Gerstgrasser, R. Jakob, K.S. Pandya, J. Stirnimann, K. Wegener, *CA single track microstructure simulation of nickel base alloy CM247LC and stainless steel S316L, including experimental validation of S316L*, Materials and Design 199 (2021) 109395, https://doi.org/10.1016/j.matdes.2020.109395.

[38] M. Gerstgrasser, *Selective laser melting of CM247LC*, PhD dissertation, ETH Zürich (2021), available from: https://doi.org/10.3929/ethz-b-000529003.

[39] T. Heeling, *Synchronized Two-Beam Strategies for Selective Laser Melting*, PhD dissertation, ETH Zürich, available from: https://doi.org/10.3929/ethz-b-000270330.

[40] D. Stefanescu, *Thermodynamic Concepts—Equilibrium and Nonequilibrium During Solidification*, in: *Science and Engineering of Casting Solidification*, Springer, 2015, pp. 17-18, https://doi.org/10.1007/978-3-319-15693-4_2.

[41] Y.T. Tang, C. Panwisawas, J.N. Ghoussoub et al., *Alloys-by-design: Applications to new superalloys for additive manufacturing*, Acta Materialia 202 (2021) 417-436, https://doi.org/10.1016/j.actamat.2020.09.023.

[42] V.D. Divya, R. Muñoz-Moreno, O.M.D.M. Messé et al., *Microstructure of selective laser melted CM247LC nickel-based superalloy and its evolution through heat treatment*, Materials Characterization 114 (2016) 62-74, http://dx.doi.org/10.1016/j.matchar.2016.02.004.

[43] K.-M. Kim, H.-E- Jeong, Y.-S. Jeong et al., *Effect of ERNiFeCr-2 Filler Metal on Solidification Cracking Susceptibility of CM247LC Superalloy Welds*, Korean J. Met. Mater. 59 (2021) 698-708, http://dx.doi.org/10.3365/KJMM.2021.59.10.698.

[44] Z. Chen, Y. Lu, F. Luo et al., *Effect of Laser Scanning Speed on the Microstructure and Mechanical Properties of Laser-Powder-Bed-Fused K418 Nickel-Based Alloy*, Materials 15 (2022) 3045, https://doi.org/10.3390/ma15093045.

[45] M. Okugawa, D. Izumikawa, Y. Koizumi, *Simulations of Non-Equilibrium and Equilibrium Segregation in Nickel-Based Superalloy Using Modified Scheil-Gulliver and Phase-Field Methods*, Materials Transactions 61-11 (2020) 2072-2078, https://doi.org/10.2320/matertrans.MT-MA2020005.

[46] K. C. Mills, Y. M. Youssef, Z. Li, Y. Su, *Calculation of Thermophysical Properties of Ni-based Superalloys*, ISIJ International 46 (2006) 623-632, https://doi.org/10.2355/isijinternational.46.623.

[47] S. Kumar, *10.05 - Selective Laser Sintering/Melting*, in: S. Hashmi, G. Ferreira Batalha, C.J. Van Tyne, B. Yilbas (Eds.), *Comprehensive Materials Processing*, Elsevier, 2014, pp. 94-134, https://doi.org/10.1016/B978-0-08-096532-1.01003-7.

[48] L. Avala, M. Bheema, P. K. Singh et al., *Measurement of Thermo Physical Properties of Nickel Based Superalloys*, IJMER, ISSN (Print): 2321-5747, Volume-1, Issue-1, 2013, http://www.irdindia.in/journal_ijmer/pdf/vol1_iss1/19.pdf.

[49] F. Ahsan, J. Razmi, L. Ladani, *Experimental measurement of thermal diffusivity, conductivity and specific heat capacity of metallic powders at room and high temperatures*, Powder Technology 374 (2020) 648-657, https://doi.org/10.1016/j.powtec.2020.07.043.

[50] M.W. Chase, *NIST-JANAF Themochemical Tables, Fourth Edition*, J. Phys. Chem. Ref. Data, Monograph 9, 1998, 1-1951, available from: https://webbook.nist.gov/cgi/cbook.cgi?ID=C7439896&Units=SI&Type=JANAFG&Table=on#JANAFG.

[51] M. Gouge, P. Michaleris, E. Denlinger, J. Irwin, *The Finite Element Method for the Thermo-Mechanical Modeling of Additive Manufacturing Processes*, in M. Gouge, P.

Micharelis (Eds.), Thermo-Mechanical Modeling of Additive Manufacturing, Elsevier, 2018, pp. 19-38, https://doi.org/10.1016/B978-0-12-811820-7.00003-3.

[52] T. Hoshino, K. Mito, A. Nagashima et al., *Determination of the thermal conductivity of argon and nitrogen over a wide temperature range through data evaluation and shock-tube experiments*, Int J Thermophysics 7 (1986) 647–662, https://doi.org/10.1007/BF00502397.

[53] J. Draxler et al., *Modeling and simulation of weld solidification cracking part III*, Welding in the World 63 (2019) 1883-1901, https://doi.org/10.1007/s40194-019-00784-3.

[54] T.P. Gabb, R.A. MacKay, S.L. Draper et al., *The Mechanical Properties of Candidate Superalloys for a Hybrid Turbine Disk*, NASA/TM-2013-217901. Available electronically at https://ntrs.nasa.gov/citations/20140000732.

[55] S.-J. Wu, P.-C. Chin, H. Liu, *Measurement of Elastic Properties of Brittle Materials by Ultrasonic and Indentation Methods*, Appl. Sci. 9 (2019) 2067, https://doi.org/10.3390/app9102067.

[56] T. Bouchenot, *On the Interaction of Creep and High-Cycle Fatigue in CM 247 LC*, Electronic Theses and Dissertations (2020) 475, https://stars.library.ucf.edu/etd2020/475.

[57] Q. Chen, Y. Zhao, S. Strayer et al., *Elucidating the effect of preheating temperature on melt pool morphology variation in Inconel 718 laser powder bed fusion via simulation and experiment*, Additive Manufacturing 37 (2021) 101642, https://doi.org/10.1016/j.addma.2020.101642.

[58] R. Cunningham et al., *Keyhole threshold and morphology in laser melting revealed by ultrahigh-speed x-ray imaging*, Science 363 (2019) 849-852, https://doi.org/10.1126/science.aav4687.

[59] A.V. Gusarov, I. Yadroitsev, Ph. Bertrand, I. Smurov, *Model of Radiation and Heat Transfer in Laser-Powder Interaction Zone at Selective Laser Melting*, J. Heat Transfer 131 (2009) 072101, https://doi.org/10.1115/1.3109245.

[60] A. Stein, *Simulation rotordynamischer Problemstellungen mit der Smoothed Particle Hydrodynamics Methode*, PhD dissertation, University of Kassel (2016), available from: https://dx.doi.org/doi:10.19211/KUP9783737602211.